



HAL
open science

Nonlinear dynamics of volcanic systems from geodetic data

Damian Walwer

► **To cite this version:**

Damian Walwer. Nonlinear dynamics of volcanic systems from geodetic data. Geophysics [physics.geoph]. Université Paris sciences et lettres, 2018. English. NNT : 2018PSLEE004 . tel-01875362

HAL Id: tel-01875362

<https://theses.hal.science/tel-01875362>

Submitted on 17 Sep 2018

HAL is a multi-disciplinary open access archive for the deposit and dissemination of scientific research documents, whether they are published or not. The documents may come from teaching and research institutions in France or abroad, or from public or private research centers.

L'archive ouverte pluridisciplinaire **HAL**, est destinée au dépôt et à la diffusion de documents scientifiques de niveau recherche, publiés ou non, émanant des établissements d'enseignement et de recherche français ou étrangers, des laboratoires publics ou privés.

THÈSE DE DOCTORAT

de l'Université de recherche Paris Sciences et Lettres
PSL Research University

Préparée à l'École Normale Supérieure

Nonlinear dynamics of volcanic systems from geodetic data

Dynamique non linéaire des systèmes volcaniques à partir des données géodésiques

Ecole doctorale n°560

Ecole Doctorale STEP'UP

Spécialité Sciences de la Terre et de l'Environnement

COMPOSITION DU JURY :

Mme. PINEL Virginie
Université Savoie Mont-Blanc,
Rapporteur

M. De Viron Olivier
Université de la Rochelle, Rapporteur

Mme. DOIN Marie-Pierre
Université Grenoble Alpes, Examinatrice

M. JAUPART Claude
Institut de Physique du Globe de Paris,
Président du jury

M. CALAIS Eric
Ecole Normale Supérieure, Directeur de
thèse

M. GHIL Michael
Ecole Normale Supérieure, Co-directeur
de thèse

**Soutenue par Damian
WALWER
le 23 février 2018**

**Dirigée par Eric Calais et
Michael Ghil**



RÉSUMÉ

Nous étudions dans un premier temps l'intérêt de l'utilisation de la "multichannel singular spectrum analysis" (M-SSA) sur des séries temporelles de positionnements GPS. Cette méthode permet de simultanément analyser un ensemble de séries temporelles et d'en extraire des modes de variabilités communs sans utiliser d'information a priori sur les structures spatiales et temporelles des champs géophysiques. Ces modes correspondent à des tendances non linéaires, des oscillations ou du bruit.

Après avoir validé cette méthode sur des séries synthétiques imitant certaines caractéristiques génériques des séries temporelles GPS nous l'appliquons à des données enregistrées sur le volcan Akutan en Alaska. Nous y extrayons deux types de signaux. L'un périodique de période annuel et semi-annuel correspondant à des déformations dites saisonnières. L'autre représentant deux cycles d'inflations et de déflations successifs du volcan Akutan. Les inflations sont rapides et courtes et suivies de déflations plus lentes et plus longues.

Dans une seconde partie nous tirons parti de la M-SSA pour analyser des séries temporelles enregistrées sur plusieurs volcans. Les volcans Okmok et Shishaldin en Alaska et le Piton de la Fournaise à la Réunion possèdent une partie de leurs histoires de déformations qui est similaire à celle d'Akutan. Le caractère oscillatoire de ces cycles de déformations mis en évidence par la reconstruction de portraits de phases nous mène à faire une analogie entre le régime oscillatoire d'un simple oscillateur non linéaire et les cycles de déformations observés à ces volcans.

Les données pétrologiques, géochimiques et géophysiques disponibles pour Okmok et le Piton de la Fournaise combinées aux contraintes sur la dynamiques apportées par

l'oscillateur non linéaire permet de proposer un modèle physique. Deux réservoirs superficiels sont connectés par un conduit cylindrique dans lequel le magma possède une viscosité qui dépend de la température. Un tel système se comporte de manière similaire à l'oscillateur non linéaire étudié précédemment. Lorsque que le gradient de température vertical présent dans le fluide est suffisamment important et que le flux de magma entrant dans le système de réservoirs est compris entre deux valeurs déterminées analytiquement un régime oscillatoire non linéaire se met en place. Ce régime se caractérise par des phases de variations rapides et courtes de surpressions dans les réservoirs suivies de phases plus calmes.

CONTENTS

| | |
|--|------------|
| Résumé | iii |
| 1 Introduction | 1 |
| 2 Data-adaptive analysis of geodetic time series | 7 |
| 2.1 Abstract | 7 |
| 2.2 Introduction and motivation | 8 |
| 2.3 Multichannel Singular Spectrum Analysis (M-SSA) | 10 |
| 2.3.1 Formulation | 10 |
| 2.3.2 Synthetic Example | 12 |
| 2.3.3 Signal Reconstruction | 14 |
| 2.3.4 M-SSA versus SSA and PCA | 15 |
| 2.4 Application to Transient Deformation of the Akutan Volcano, Alaska | 16 |
| 2.4.1 The GPS Data | 17 |
| 2.4.2 Choice of window width M | 18 |
| 2.4.3 Singular Spectrum, ST-EOFs and ST-PCs | 19 |
| 2.4.4 Testing the statistical significance of the extracted modes | 19 |
| 2.4.5 Seasonal Signals | 21 |
| 2.4.6 Transient Signals | 24 |
| 2.5 Discussion | 27 |

| | | |
|----------|--|-----------|
| 2.5.1 | Implications for Transient Detection in Large GPS Networks | 27 |
| 2.5.2 | Noise Extraction from GPS Time Series | 28 |
| 2.5.3 | M-SSA, GPS Time Series and Nonlinear Dynamical Systems | 29 |
| 2.6 | Conclusion | 30 |
| 2.7 | Appendix: Southern California Earthquake Center (SCEC) validation Exercise | 31 |
| 2.8 | Figures | 32 |
| 3 | Nonlinear dynamics of volcanic inflation/deflation cycles | 55 |
| 3.1 | Abstract | 55 |
| 3.2 | Introduction | 56 |
| 3.3 | Methods | 57 |
| 3.3.1 | Data and preprocessing | 57 |
| 3.3.2 | Volcanic signal reconstructions | 57 |
| 3.4 | Deformation trends at four volcanoes | 58 |
| 3.5 | Similarities in behavior | 59 |
| 3.6 | A simple nonlinear oscillator | 61 |
| 3.7 | Discussion and conclusions | 63 |
| 3.8 | Appendix A: Reconstruction of the volcanic signal | 65 |
| 3.9 | Appendix B : Linear Stability Analysis | 67 |
| 3.10 | Appendix C : Nonlinear stability and Hopf bifurcation | 68 |
| 3.11 | Figures | 69 |
| 4 | A fluid-dynamics–based model of reservoir overpressure oscillations as inferred from geodetic time series | 83 |
| 4.1 | Abstract | 83 |
| 4.2 | Introduction | 84 |
| 4.3 | Multiple reservoirs at Okmok and Piton de la Fournaise | 85 |
| 4.3.1 | Okmok | 85 |
| 4.3.2 | Piton de la Fournaise | 86 |
| 4.4 | Okmok and Piton de la Fournaise geodetic time series | 87 |

| | | |
|----------|--|------------|
| 4.4.1 | Okmok (1997-2008) | 87 |
| 4.4.2 | Piton de la Fournaise (2003-2007) | 88 |
| 4.5 | Theoretical model of magma reservoirs interaction | 88 |
| 4.5.1 | Fluid flow in a cylindrical pipe with temperature dependent viscosity | 88 |
| 4.5.2 | Two shallow magma reservoirs fed by a deeper source | 91 |
| 4.5.3 | Dimensions | 93 |
| 4.5.4 | Linear stability analysis and Hopf bifurcation | 94 |
| 4.6 | Okmok: two successive exponential inflations followed by damped oscillations | 96 |
| 4.6.1 | Two successive exponential inflations | 96 |
| 4.6.2 | The transition between the exponential inflations and the oscillations | 98 |
| 4.7 | Piton de la Fournaise: an irregular behavior | 99 |
| 4.7.1 | On irregular temporal patterns | 99 |
| 4.7.2 | Effect of volatiles on the oscillations | 100 |
| 4.8 | Concluding remarks | 101 |
| 4.8.1 | Summary | 101 |
| 4.8.2 | Relaxation oscillations as a mechanism for triggering eruptions? . . . | 102 |
| 4.8.3 | Conclusion | 103 |
| 4.9 | Appendix A: Linear hydraulic interaction of two shallow reservoirs fed by a source region | 103 |
| 4.10 | Appendix B: The link between the effective bulk modulus of a magma cham- ber and the volatile content of magmas | 104 |
| 4.11 | Table | 106 |
| 4.12 | Figures | 106 |
| 5 | Conclusions and Perspectives | 117 |

LIST OF FIGURES

| | | |
|-----|---|----|
| 2.1 | Univariate synthetic time series (black dots) composed of, from top to bottom in gray, a transient displacement, annual and semi-annual harmonic functions, as well as colored and white noise. | 33 |
| 2.2 | Singular spectrum of the synthetic time series shown in Figure 2.1. Eigenvalues are normalized to represent the appropriate fraction of the total variance of the time series, and they sum to 1. | 33 |
| 2.3 | The five leading temporal empirical orthogonal functions (T-EOFs) extracted from the synthetic time series; they are associated with the first five eigenvalues in Figure 2.2. | 34 |
| 2.4 | The five leading temporal principal components (T-PCs) associated with the five T-EOFs of Figure 2.3. These T-PCs are time coefficients that weigh the corresponding T-EOFs in reconstructing the original time series; they represent the different modes of variability of the time series. | 34 |

| | | |
|-----|---|----|
| 2.5 | Reconstruction of the transient displacement (top panel) and the seasonal oscillations (bottom panel) in our synthetic example. Black dots = synthetic time series, grey lines = synthetic transient and oscillatory signals embedded in the synthetic time series, red lines = reconstructed signals using M-SSA. Top: the reconstruction using the first T-PC and corresponding T-EOF captures the transient displacement signal. Bottom: the reconstruction using the first five T-PCs and corresponding T-EOFs additionally captures the seasonal signal. | 35 |
| 2.6 | Evaluation of the improvement in M-SSA reconstruction as a function of (A) the number L of time series and (B) of window width M . (A) Misfit between the synthetic transient signal and its reconstruction versus the number L of synthetic time series used in M-SSA. (B) Misfit between the synthetic transient signal and its reconstruction versus M , the maximum lag used to compute the covariance matrix. All the synthetic time series are similar to the one in Figure 2.1 and share the same transient displacement. Black dots correspond to the results of an experiment that uses a white noise ($\alpha = 0$), while gray dots correspond to colored noise with a spectral index of $\alpha = 1$ and black diamonds correspond to a noise with a spectral index of $\alpha = 2$. The separating power of M-SSA improves as the number of the series sharing a transient signal increases as well as M increases. | 36 |
| 2.7 | Maps showing the location of the Akutan volcano within the Aleutian arc (inset) and of the eight continuously recording GPS receivers (black triangles) used in this study on the island (main map). | 37 |
| 2.8 | Singular spectrum of the GPS position time series at 8 cGPS sites on Akutan volcano from early 2006 to late 2014. The first 30 M-SSA eigenvalues are plotted for the window widths $M = 400, 500$, and 600 days. Eigenvalues are normalized as in Figure 2.2, so that their sum is unity. | 37 |

2.9 The eleven leading ST-PCs associated either with the trend with non-constant slope or the seasonal oscillations. They are calculated using (A) $M = 400$, (B) $M = 500$, and (C) $M = 600$ days. The persistence of the shape of the ST-PCs for the different values of M — ignoring the occasional change of sign, which is a numerical artefact of PCA in general — is an indicator of the significance of the extracted modes. Regardless of the value of M , ST-PCs 1, 4, 5 and 8 jointly capture the data-adaptive trend, while the ST-PC pair 2-3 represents the annual oscillations. The four ST-PCs 6-7 and 9-11 capture the semi-annual oscillations for $M = 400$, whereas this mode is captured by ST-PCs 6-7 and 9-10 for $M = 500$ and ST-PCs 8-10 and ST-PCs 6-9 for $M = 600$. 38

2.10 Spatio-temporal empirical orthogonal functions (ST-EOFs) associated with eigenvalues 2 (black) and 3 (gray) (see Figure 2.8) calculated using (A) $M = 400$, (B) $M = 500$, and (C) $M = 600$ days. The subpanels show the components of these EOFs for each cGPS site and each direction of motion being measured. These two ST-EOFs capture the annual oscillatory mode of annual period present in the data. The differences between estimates using different values of M are small. 39

2.11 MC-MSSA test of statistical significance using surrogate data containing (A) flicker noise, with spectral index $\alpha = 1$; and (B) random walk noise noise, with $\alpha = 2$. Lower and upper ticks on the error bars correspond to the 2.5% and 97.5% quantiles of an ensemble of 500 surrogate data that are different realizations of the null hypothesis under consideration. These tests show that modes associated with eigenvalues 5 and 8 that lie within the corresponding confidence intervals are possibly generated by the presence of colored noise in the GPS time series recorded at Akutan volcano. 40

2.12 Seasonal variability of the GPS data set for Akutan. Black dots: detrended daily GPS position time series at 8 sites on Akutan volcano, Alaska, with their $1-\sigma$ error bars. Red lines: reconstructed series after M-SSA using the combination of ST-PCs 2–3 (annual) and 6-7 plus 9–11 (semi-annual). The black vertical lines in the topmost panels represent 10 millimeters. The subpanels correspond to the 8 cGPS sites and 3 directions of motion as in Figure 2.10. Note the good visual fit to the data. The pluri-annual modulation of the seasonal signal is clearly visible, for instance, in the lower-amplitude vertical signal for 2009, which appears across all the stations. The light red areas represent the variability of the reconstructions of the seasonal oscillations when the raw time series are perturbed by colored noise with spectral index of 1. 41

2.13 Comparison between the reconstruction of the seasonal signal obtained with M-SSA (red solid curve) and a commonly used fit of the sum (black solid curve) of an annual and a semi-annual harmonic function for each component recorded at site AV10: (A) northward, (B) eastward, and (C) upward. We applied a 20-day moving average to the raw data (black dots) to reduce the data scatter and be able to better distinguish the difference between the M-SSA reconstructions and the four-term Fourier series. The two models are, to first order, very close, but M-SSA reconstructions show a pluri-annual modulation in amplitude that is not present in the constant-amplitude harmonic functions. Note also that these harmonic functions significantly underestimate the observed range of values in the vertical component. The weighted root mean square (WRMS) are $3.29mm$, $2.99mm$ and $8.44mm$ for the M-SSA reconstructions of the seasonal signal for the North, East and Up components respectively. The harmonic functions fit have a WRMS of $3.32mm$, $3.05mm$ and $9.14mm$ which is systematically higher. 42

| | | |
|------|--|----|
| 2.14 | Transient motion at Akutan volcano, Alaska. The subpanels correspond to the 8 cGPS sites and 3 directions of motion as in Figure 2.10. Note the good visual fit to the data. Black dots: detrended daily GPS position time series at the 8 cGPS sites; with their $1\text{-}\sigma$ error bars. Red lines: M-SSA reconstructions, using the trend ST-PCs 1 and 4, which together carry 11% of the total data variance. The black vertical lines in the topmost panels represent 10 millimeters. The light red areas represent the variability of the reconstruction of the data-adaptive trends when the raw time series are perturbed by colored noise with spectral index of 1. | 43 |
| 2.15 | Maps of the horizontal and vertical displacements at Akutan volcano that are associated with the four dominantly monotonic parts of the reconstructed trends derived from ST-PCs 1 and 4. For each event, the two upper panels plot the vector displacements at the 8 cGPS sites, while the lower panel plots the time series of northward displacements at site AV12. In this latter panel, black dots show the raw data and the red solid curves show the M-SSA-reconstructed trend signals, while the blue solid curves show the best-fit prediction from a simple, idealized model of magma chamber expansion (Mogi, 1958). In the upper panels, the red arrows are based on the M-SSA reconstructions and the blue ones are based on the Mogi (1958) model. Note the spatial consistency of the displacements for each of the four successive episodes with a radial pattern centered on the volcano that is consistent with a magmatic origin. | 44 |
| 2.16 | Misfit plots between the deformation predicted by a Mogi source and the observed displacements for each of the four transient events shown in Figure 2.15. The four events are well explained by inflation (uplift and radial extension at the surface) or deflation (subsidence and radial contraction at the surface) of the same point source at 8 ± 1 km. These results strongly support the hypothesis that the small but coherent deformations extracted by M-SSA are of magmatic origin. | 45 |

| | | |
|------|--|----|
| 2.17 | M-SSA analysis of the PBO network of 80 GPS stations from Alaska: (A) geographic distribution of the stations; and (B) the six leading ST-PCs calculated by applying M-SSA to the position time series from this network. ST-PCs 1,2 are in phase quadrature and represent a seasonal oscillation with an annual period. The next 4 ST-PCs represent data-adaptive trends. | 46 |
| 2.18 | Reconstructed time series (solid red lines) using ST-PCs 3–6 of Figure 2.17B, which represent data-adaptive trends. The black vertical lines in the topmost panels represent 10 millimeters. The reconstructions here are for the same 8 cGPS sites on Akutan volcano as plotted in Figure 2.14, and are presented in the same format. Here, however, the reconstructions are calculated from the 80×3 time series from the PBO network covering Alaska and shown in Figure 2.17A. Note the similarity with the reconstructed series derived solely from the 8×3 Akutan GPS time series, plotted in Figure 2.14. For 15 (~60%) of them the correlation coefficients between the reconstructed time series from 8 stations and 80 stations are larger than 0.7. For 7 of them (~30%) the correlation coefficients are less than 0.5. However, these 7 time series are those for which the signal is very weak such as in the three components recorded at AV15. | 47 |
| 2.19 | Map of the horizontal displacements associated with the first transient deformation event identified above for the Alaskan PBO network; this event corresponds to the time interval 2008.0–2008.7, cf. Figure 2.18. The red arrow over the Gulf of Alaska indicates a horizontal displacement of more than 1 mm. To make them visible we indicate GPS sites with displacements less than 1 mm with red dots indicate. Note that displacements at Akutan stand out as anomalously large, with a radial pattern. Figure 2.20 below shows a close-up on Akutan. | 48 |

2.20 Comparison of the horizontal and vertical displacements associated with the first transient-deformation event identified above (2008.0 to 2008.7), as extracted from the 8-site M-SSA (black arrows vs. the 80-site, Alaska-wide M-SSA (white arrows). Note the agreement between the local and the regional-scale M-SSA estimates: both show a radial pattern of extension and uplift centered on the volcano. This pattern is consistent with a magmatic origin, as seen in Figure 2.15 above. 49

2.21 Power Spectral density plots of the raw time series (grey lines) and M-SSA-based seasonal signal (red); the residual component, i.e. raw minus the M-SSA reconstruction of the transient displacements plus the seasonal signals is plotted as black lines. Note the flattening of the spectrum of the residuals at low frequency, indicating that the trend and the oscillatory components are extracted by M-SSA, while preserving the high-frequency noise content. 50

2.22 The four leading ST-PCs obtained from the M-SSA on the synthetic time series of the SCEC transient detection exercise. ST-PC pair 1-2 capture the annual oscillations. ST-PC pair 5-6 capture the semi-annual oscillations. Together these two ST-PCs pairs that represent the seasonal oscillations carry ~ 50% of the variance. ST-PCs 3 and 4 capture the data-adaptive trend and describe ~ 15% of the total variance of the data set. 51

2.23 Reconstructed Transient motion at some GPS sites near the Santa-Monica fault. The subpanels correspond to 8 selected cGPS sites and the horizontal directions of motion. Black dots: detrended daily GPS position time series at the 8 cGPS sites. Red lines: M-SSA reconstructions using the trend ST-PCs 3 and 4 which together carry 15% of the total data variance. Blue lines: synthetic transient displacement generated by a simulated thrust event on the Santa Monica fault. The M-SSA filtered time series are consistent with the transient displacements except in the east component recorded at site "dshs" which contains large-amplitude colored noise. 52

| | | |
|------|--|----|
| 2.24 | Maps of the horizontal displacement at some cGPS sites near the Santa-Monica fault. Red arrows: transient horizontal displacements derived from the M-SSA reconstructions of the data-adaptive trends of the time series. Blue arrows: simulated horizontal displacements associated to a thrust event on the Santa Monica fault. The segment of the Santa Monica fault on which the slip occurred is represented by the rectangular patches. The M-SSA reconstructions are consistent with the simulated thrust event. The large discrepancy at site DSHH is caused by colored noise of large amplitude on the east component (see Figure 2). | 53 |
| 3.1 | Location map of the four volcanoes used in this study, showing the GPS sciteps (grey triangles) from which the displacement time series used here have been extracted. | 70 |
| 3.2 | Spatial and temporal pattern of horizontal displacements at the four volcanoes. The top sub-panels for each volcano show the total horizontal displacements (black and grey arrows) during a selected episode of inflation; these episodes are indicated by the two vertical black lines on the time series in the sub-panels displayed below. Note the difference in scale between the grey and black arrows. The bottom sub-panels show a selected GPS time series: the black dots are the raw GPS time series, while the red line shows the corresponding M-SSA reconstruction. The corresponding GPS receivers are labeled on the maps. | 71 |
| 3.3 | Phase portrait reconstructions in the displacement vs. rate-of-displacement plane and the corresponding displacement time series. The least noisy M-SSA-reconstructed displacement component is plotted for each volcano, normalized so that all four lie between ± 1 . The grey scale, from white to black, indicates the evolving time, in years. | 72 |

| | | |
|------|--|----|
| 3.4 | Nonlinear oscillation of the idealized model governed by Eq. (3.2): (a) phase portrait in the (x, y) -plane, with $y = \dot{x}$; (b) and (c) the associated time series representing, respectively, x and y . All plots are computed using $\mu = 10$, $x_0 = 0.8$ and $y_0 = -0.5$ in the equations. In panel (a), the closed trajectory (heavy solid line) is the limit cycle. The light solid lines are typical trajectories converging to the limit cycle from the interior and the exterior of this cycle. The shaded area is the one where damping is negative, i.e. $\kappa > 0$ in Eq. (3.2). Arrows indicate the direction of motion on the limit cycle and on the trajectories that converge onto it. The light straight line through the origin, denoted by \mathcal{T}^u , indicates the unstable direction along which trajectories are ejected from the origin. Letters M , m and d in panels (a), (b) and (c) show, respectively, the time of maximum amplitude of x , minimum amplitude of x , and the slope break during the deflation phase. See text and Supplementary Materials for details. | 73 |
| 3.5 | Same as Fig. 3.1 in the main text, but only for Akutan. In this case, successive episodes of inflation and deflation are included, as well as a separate map view of the vertical displacements for each episode of monotonic deformation. | 74 |
| 3.6 | Same as Fig. 3.5, but for Shishaldin. | 75 |
| 3.7 | Same as Fig. 3.5, but for Okmok. | 76 |
| 3.8 | Same as Fig. 3.5, but for Piton de la Fournaise. | 77 |
| 3.9 | M-SSA analysis applied to the time series recorded at Akutan: (a) the 30 leading eigenvalues; and (b) the 8 leading PCs. The first and third PCs allow one to describe the temporal evolution of the volcanic system and produce the expected radial pattern of inflation and deflation episodes plotted in Figure 3.5. | 78 |
| 3.10 | Same as Figure 3.9, but for Shishaldin. The number of leading PCs plotted in panel (b) is 9. Here, the second PC suffices to describe the temporal evolution of the volcanic system and reproduce the radial inflation and deflation patterns plotted in Figure 3.6. | 79 |

| | | |
|------|--|-----|
| 3.11 | Same as Figure 3.9, but for Okmok: (a) the 20 leading eigenvalues; and (b) the 7 leading PCs. The first three PCs allow one to describe the temporal evolution of the volcanic system, along with the radial inflation and deflation patterns plotted in Figure 3.7. | 80 |
| 3.12 | Same as Figure 3.11, but for Piton de la Fournaise. The first four PCs allow one to describe the temporal evolution of the volcanic system, along with the radial inflation and deflation patterns in Figure 4.2. | 81 |
| 4.1 | Location map of Okmok showing the GPS sites (grey triangles) from which the displacement time series used here have been extracted | 107 |
| 4.2 | Location map of Piton de la Fournaise showing the GPS sites (grey triangles) from which the displacement time series used here have been extracted. . . . | 108 |
| 4.3 | Geodetic time series products from Okmok volcano. The top sub-panel shows the cumulative volume change estimated from InSAR time series (Biggs et al., 2010). The bottom sub-panels shows a selected GPS time series reflecting the deformation regime before the 2008 eruption. | 109 |
| 4.4 | A selected GPS time series recorded at the summit of Piton de la Fournaise. The top sub-panel shows the time series between 2003 and 2007.5 (black dot) as well as the different intrusive and eruptive events (grey areas). The bottom sub-panel zooms in the pre-eruptive period of the large 2007 eruption. | 110 |
| 4.5 | Schematic representation of the various elements composing the model described in the main text. Two shallow reservoirs, that have volume V_B and V_T and inside which the pressure are denoted P_B and P_T , are supplied by a deeper source region of constant pressure P_S | 111 |
| 4.6 | Changes in the shape of $f(w)$ as the dimensionless parameter A varies. When A is above 6 there is a range of w for which $f(w)$ increases. This is the critical characteristic of f that allows for the emergence of the relaxation oscillations. | 112 |

| | | |
|------|---|-----|
| 4.7 | Nonlinear oscillations of the reduced model governed by Eq. (4.16): (a) phase portrait in the $(\Delta X, w)$ -plane ; (b) and (c) the associated time series representing, respectively, X and w . All plots are computed using $[\gamma, A, B, C, Q] = [10, 150, 1, 3, 4]$ in the equations. In panel (a), the closed trajectory (heavy solid line) is the limit cycle. The dashed curve represents the function $f(w)$ that is responsible for the shape of the limit cycle. As it can be understand from equation 4.24, the trajectory of the limit cycle either follow $f(w)$ or vertical lines. | 113 |
| 4.8 | Time series reflecting the dynamics of the reservoir overpressure that is governed by equations 4.8 :(a) time series of both P_B and P_T ; (b) time series of $P_T - P_B$. Plots are computed using $[\gamma, A, B, C] = [2.5, 350, 10, 20]$ | 114 |
| 4.9 | The effective modulus of the magmatic chambers as a function of both the weight fraction of crystals x and the total weight fraction of volatile. The computation is explained in section 4.10. The curves are computed using $\rho_m = 3000kg.m^{-3}$, $\rho_{ho_c} = 3200kg.m^{-3}$, $T = 1100C$, $P = 60MPa$ and $E = 10^{10}Pa$. | 115 |
| 4.10 | Effect of volatile exsolution on the overpressure oscillations in the top shallow reservoir. Two time series have been computed using two values of γ separated by two orders of magnitude which is approximately the effect that would have volatile exsolution on γ . Exsolution of volatile causes an increase of the value of γ that in turn causes a decrease of the amplitude and period of the oscillations. Both time series have been computed using $A = 150$, $Q = 4$, $B = 1$, $C = 3$ | 116 |
| 5.1 | Phase portrait reconstructions in the displacement vs. rate-of-displacement vs. rate-of-displacement of the co-eruptive subsidence space. The geometric shape draw by the trajectory is reminiscent of a Shilnikov bifurcation (To be compared with figure 6.12 in (e.g. Ghil and Childress, 1987)). | 122 |

LIST OF TABLES

| | | |
|-----|--|-----|
| 3.1 | Summary of the parameters and results of the M-SSA analysis. Here τ_s is the sampling time; N number of data points; D the number of channels, i.e. of stations \times (displacements = 3); M is the window length; and S the number of leading modes retained for further study. | 65 |
| 4.1 | List of main variables and parameters described in the main text. | 106 |

CHAPTER 1

INTRODUCTION

Le contexte moderne des sciences de la Terre se caractérise par la grande quantité de données disponibles et accessibles. Cette abondance est causée en partie par le développement de l'observation de la Terre de l'espace ainsi qu'à la mise en place de réseaux d'instrumentations déployés à des échelles locales, régionales et globales. Ces moyens permettent la collecte de données qui présente un grand intérêt pour l'étude des systèmes naturelles.

La géodésie spatiale représentée notamment par les techniques de positionnements GPS et d'interférométrie radar (InSAR) permet en particulier l'acquisition de mesures de déformations de la surface de la Terre. La nature de ces mesures est intéressante parce que beaucoup de phénomènes géologiques provoquent de telles déformations.

Le déploiement de réseaux GPS proches de certaines zones de subductions par exemple a révélé l'existence d'événements de glissements lents dont l'occurrence est quasi périodique (e.g., Rogers and Dragert, 2003; Radiguet et al., 2012) ou encore l'existence de déformations de longues périodes provoquées par des séismes de magnitudes élevés (dit "megathrusts"). On peut notamment faire l'observation qu'une partie du Chili se déforme toujours à cause de la relaxation visqueuse d'une partie du manteau depuis qu'il a été perturbé par le séisme de Valdivia en 1960 (e.g. Klein et al., 2016).

Outre la découverte de nouveaux phénomènes naturels ces données permettent d'estimer

les valeurs des paramètres qui leurs sont associés ou bien qui sont inhérents aux systèmes géologiques qui sont à l'origine de leurs manifestations. Ce type de pratique nécessite en général l'utilisation de modèles qui permettent de relier les phénomènes étudiés aux observations de déformations de la surface de la Terre. L'utilisation conjointe de données et de modèles dans le but d'obtenir des informations sur un système indirectement observable se fait par le biais de problèmes inverses et de l'assimilation de données (e.g., Tarantola, 2005; Ghil and Malanotte-Rizzoli, 1991).

Dans le cas de l'étude de zones de failles et des volcans les modèles utilisés pour résoudre ces problèmes inverses sont en générales statiques. Ils ne fournissent pas d'information sur les éléments qui contrôlent l'évolution du système dans le temps. En revanche ils permettent de relier des observables — c-à-d. les mesures de déformations— à des grandeurs qui nous renseignent, entre autres, sur la géométrie de l'objet géologique étudié ou sur l'intensité du phénomène qui se manifeste (e.g. Segall, 2010).

Dans le cas des séismes ou des événements de glissement lents par exemple, nous pouvons estimer la quantité de déplacement le long du plan de rupture dont la présence est à l'origine de ces instabilités (e.g. Massonnet et al., 1993; Szeliga et al., 2008). Dans le cas d'épisodes d'inflations ou déflations volcaniques, les variations de volume de chambres magmatiques ainsi que leurs profondeurs sont des grandeurs fréquemment estimées (e.g. Biggs et al., 2009; Lu et al., 2010).

Lorsque les techniques de mesure utilisées permettent d'avoir une résolution temporelle suffisante, ces méthodes d'inversions peuvent être également exploitées pour déterminer l'évolution dans le temps des paramètres estimés. On parle dans ce cas d'inversions cinématiques qui sont des successions d'inversions statiques réalisées à des moments successifs (e.g. Lu et al., 2005; Bletery et al., 2014).

Les problèmes inverses sous ces formes dominent la boîte à outils méthodologique de la communauté des géodésiens qui s'intéressent aux volcans et systèmes de failles. L'augmentation de la résolution spatiale des données —et a fortiori le développement de l'InSAR— permet de réduire l'incertitude liée aux paramètres inversées. En revanche ils ne permettent pas d'exploiter pleinement l'information contenue dans les séries tem-

porelles et dont la durée augmente quotidiennement.

Les séries temporelles offrent une information sur la dynamique qualitative des systèmes géologiques étudiés (e.g. Packard et al., 1980). Cette dynamique ne peut, par définition, être documenté à l'aide de modèles statiques. L'expression "dynamique qualitative" fait référence soit à la variabilité interne du système —c-à-d. l'évolution spontanée du système dans le temps— soit à la réponse du système à un forçage extérieur. L'utilisation quasi systématique des problèmes inverses statiques laisse supposer que davantage d'informations de nature dynamique pourraient être obtenu.

Cette perspective peut être reliée aux méthodes de traitement du signal (e.g. Broomhead and King, 1986a; Abarbanel et al., 1993; Ghil et al., 2002). Les motifs temporels dont on pourrait extraire des informations sur la dynamique qualitative des systèmes naturels sont souvent superposés à d'autres signaux ainsi qu'à du bruit qui peut avoir le désavantage d'être coloré —*i.e.*, possédant une structure temporelle qui s'apparente à un signal géologique. Aussi, le grand nombre de données disponibles rend leur inspection systématique difficile et consommatrice de temps. Une représentation parcimonieuse d'un ensemble de données contenant de l'information redondante peut donc s'avérer utile.

Une des stratégies mise en œuvre consiste à faire un a priori soit sur la structure spatiale soit sur la structure temporelle du signal que l'on souhaite extraire. Dans ce cas on peut ajuster ces structures a priori déterminées aux données et ainsi en extraire les signaux correspondant (e.g. Ohtani et al., 2010; Riel et al., 2014a).

Bien que cette stratégie soit dans certains cas justifiée, on peut vouloir extraire des séries temporelles sans utiliser de tels a priori. Certains motifs présents dans les séries temporelles ne peuvent pas être représentés de manière parcimonieuse par des fonctions analytiques. Ceci peut être relié au fait que certains motifs temporels ne correspondent tout simplement pas à d'éventuelles solutions d'équations différentielles ordinaires pour lesquelles des solutions analytiques existent. C'est pourquoi nous pouvons bénéficier de méthodes d'analyses qui nécessitent aucun a priori sur les structures spatiales et/ou temporelles des champs géophysiques.

Cette dernière constatation fournit le point de départ de la thèse présentée puisque nous

commençons par étudier l'application de la "Multichannel Singular Spectrum Analysis" (M-SSA) à des séries temporelles GPS. Elle constitue justement une méthode d'analyse de séries temporelles dite "non paramétrique" qui nécessite l'utilisation d'aucune information a priori sur la structure spatiale et/ou temporelle du champ géophysique que l'on souhaite étudier.

Dans le second chapitre nous l'appliquons à des séries temporelles GPS enregistrées à Akutan, une île volcanique de l'arc des Aléoutiennes en Alaska. Elle permet efficacement de discriminer entre deux types de signaux: un signal d'origine volcanique et un signal saisonnier. Ces deux signaux sont également extraits du bruit contenu dans les séries temporelles. Un test d'hypothèse statistique dit Monte-Carlos SSA (MC-SSA), permet d'identifier les structures des séries temporelles associées à du bruit mais qui aurait pu éventuellement être confondu avec un signal géophysique. Ce test nécessite de formuler une hypothèse nulle qui constitue un a priori sur le type de bruit présent dans les données.

Le signal volcanique extrait à Akutan forme des événements successifs d'inflations et déflations. Les périodes d'inflations sont rapides et courtes comparées aux périodes de déflations relativement lentes et longues. Des signaux similaires possédant ces caractéristiques sont extraits de trois autres volcans : Okmok et Shishaldin qui font aussi parti de l'arc des Aléoutiennes ainsi qu'au Piton de la Fournaise situé sur l'île de la Réunion. Ces signaux constituent justement un motif temporel qui n'aurait sans doute pas pu être extrait de manière parcimonieuse par des fonctions analytiques. Cette constatation ainsi que la nature oscillatoire de ces signaux suggèrent qu'ils puissent résulter d'une dynamique non linéaire.

Un système d'équations très simple contenant deux variables permet de mimer la dynamique qualitative observée à ces quatre volcans. Un tel modèle mathématique est parfois appelé une "métaphore" par la communauté des mathématiciens qui s'intéresse à la théorie des systèmes dynamiques. Il s'agit d'un analogue mathématique contenant des éléments qui permet de comprendre la dynamique des systèmes étudiés.

Dans le chapitre quatre nous utilisons cet oscillateur non linéaire comme une ligne directrice qui permet de contraindre le modèle physique employé pour expliquer les cy-

cles de déformations observés. Nous exploitons les nombreuses données géochimiques, pétrologiques et géophysiques provenant du Piton de la Fournaise et du volcan Okmok pour contraindre un tel modèle. Ces deux volcans possèdent un système de "plomberie magmatique" similaire caractérisé par la présence de plusieurs zones de stockages de magma alimentées par une source de magma basaltique plus profonde. Nous montrons que les séries temporelles géodésique de ces deux volcans peuvent être expliquées par l'interaction de chambres magmatiques superficielles connectées par un conduit dans lequel la viscosité du magma peut varier avec la température.

CHAPTER 2

DATA-ADAPTIVE ANALYSIS OF GEODETIC TIME SERIES

Ce chapitre a fait directement l'objet d'un article publié dans JGR (Walwer et al., 2016).

2.1 Abstract

The recent development of dense and continuously operating Global Navigation Satellite System (GNSS) networks worldwide has led to a significant increase in geodetic data sets that sometimes capture transient-deformation signals. It is challenging, however, to extract such transients of geophysical origin from the background noise inherent to GNSS time series and, even more so, to separate them from other signals, such as seasonal redistributions of geophysical fluid mass loads. In addition, because of the very large number of continuously recording GNSS stations now available, it has become impossible to systematically inspect each time series and visually compare them at all neighboring sites. Here we show that Multichannel Singular Spectrum Analysis (M-SSA), a method derived from the analysis of dynamical systems, can be used to extract transient deformations, seasonal oscillations, and background noise present in GNSS time series. M-SSA is a multivariate, non-parametric statistical method that simultaneously exploits the spatial and temporal correlations of geophysical fields. The method allows for the extraction of common modes of variability, such as trends with non-constant slopes and oscillations shared across time

series, without a priori hypotheses about their spatio-temporal structure or their noise characteristics. We illustrate this method using synthetic examples and show applications to actual GPS data from Alaska to detect seasonal signals and micro-deformation at the Akutan active volcano. The geophysically coherent spatio-temporal patterns of uplift and subsidence thus detected are compared to the results of an idealized model of such processes in the presence of a magma-chamber source.

2.2 Introduction and motivation

The past decade has seen a rapid increase in the number and spatial density of continuously operating Global Navigation Satellite System (GNSS) stations to monitor crustal deformation in tectonically active regions or simply serve as reference stations for surveying applications. The leading technique as of today is the Global Positioning System (GPS), with two major deformation monitoring networks currently in operation, the Plate Boundary Observatory (PBO) in the Western U.S. with roughly 2 000 stations and the GEONET (<http://www.gsi.go.jp/>) network in Japan with $\sim 5\,000$ stations.

These networks record linear site displacements due to plate motions and interseismic strain accumulation on active faults, as well as transient-deformation events of various origins — volcanic, tectonic or hydrologic (e.g., Feng and Newman, 2009; King et al., 2007; Miller et al., 2002) — whose spatio-temporal scales span several orders of magnitude. Our ability to objectively and reliably detect these transients is of primary importance because they contain information on the rheological properties and stress state of near-surface faults, as well as of the Earth’s crust and mantle. Detecting transients, however, is challenging for two reasons. First, the very large amount of data now available in large geodetic networks make the visual inspection of time series at each site very time consuming and well-nigh impossible. Second, the amplitude of these transients can be close to — or lie even below — the background noise inherent to geodetic time series.

Several methods have recently been proposed to detect transient deformation in GPS time series. Ohtani et al. (2010) model GPS time series as the sum of a spatially coherent signal described as a sum of spatial wavelets weighted by temporally varying coefficients plus

2.2. INTRODUCTION AND MOTIVATION

errors from different sources, such as reference frame, site-specific noise and observation error. Ji and Herring (2013) first smooth the time series using a Kalman filter to increase signal-to-noise ratio, while explicitly estimating annual and semi-annual harmonic terms to model the seasonal oscillations commonly observed in GPS time series. They analyze the data in the temporal dimension first by estimating time-correlated signals, then, in a separate step, use a principal component analysis (PCA) to exploit the spatial correlations between the smoothed and filtered time series.

The approach of Riel et al. (2014a) is to parameterize position time series using a dictionary of temporally varying non-orthogonal functions assumed to represent all possible signal types present in the data. The dictionary contains functions to model known signals, such as sinusoidal functions for seasonal oscillations or logarithmic functions for post-seismic deformation. It also contains B-spline functions with various periods and starting times to represent transient displacements. The method accounts for spatial correlations using common B-spline functions to describe transient mode of variability shared across several time series.

These methods all aim at improving the signal-to-noise ratio, while using the spatial or temporal correlation inherent to GPS position time series to search for transient events. All three use a priori hypotheses on the spatial or temporal structure of the transients to build basis functions — e.g., wavelets or B-splines — onto which the data can then be projected to detect and extract those transients. In Ji and Herring (2013) the a priori hypothesis is the stochastic process that gives rise to the noise and the transient signal.

All these methods also parameterize the seasonal signal as a sum of harmonic functions with annual and semi-annual periods; this assumption prevents one, however, from accounting for interannual variability. Moreover, the stochastic properties of GPS position time series and the temporal and spatial shapes of transient events are not really known at this time. Making educated guesses on the stochastic properties of GPS time series or on the basis functions that best describe their temporal correlations is a valid approach, but one would like in fact to extract this information from the GNSS data sets in a data-adaptive way, i.e., purely based on information contained in the data, without a priori assumptions.

The purpose of this paper is to show that some of these shortcomings can be overcome using Multichannel Singular Spectrum Analysis (M-SSA). M-SSA is an advanced time series analysis method that simultaneously takes advantage of the spatial and temporal correlations in geophysical fields to extract empirical basis functions that represent the common modes of spatio-temporal variability of the data set. The main benefit of this method is to allow unraveling oscillations and trends with non-constant slopes embedded in time series without using any a priori knowledge about their period and amplitude or their spatio-temporal structures. M-SSA was first proposed, in the version used here, in the field of climate studies by Keppenne and Ghil (1993) and Plaut and Vautard (1994) to extract low-frequency oscillations of the atmospheric system from geopotential height field data. It was also used to study surface winds (Jiang et al., 1995) and sea level data (Unal and Ghil, 1995). Ghil et al. (2002) provide a review of the methodology and of many applications; see also <http://web.atmos.ucla.edu/tcd/ssa/> for further details and references.

We show in the following that M-SSA is well-suited to extract geophysically relevant information from GPS position time series. In the next section, we briefly review the methodology and illustrate its application to a set of synthetic time series whose properties resemble those of GPS records. This methodology is then applied in Section 2.4 to a set of recorded displacements at 8 GPS sites on the Akutan volcano in the Aleutian Islands. In Section 2.5, we show that M-SSA can be successfully applied to larger data sets, by using 80 stations from the network covering Alaska, as well as to the extraction of noise characteristics from the Akutan signals.

2.3 Multichannel Singular Spectrum Analysis (M-SSA)

2.3.1 Formulation

Chen et al. (2013) have already proposed using single-channel SSA for the extraction of the seasonal signal from a single GPS time series, and reviewed the univariate methodology. The emphasis here is on the often more powerful multivariate case.

2.3. MULTICHANNEL SINGULAR SPECTRUM ANALYSIS (M-SSA)

Let

$$\{X_l(t) : l = 1, \dots, L; t = 1, \dots, N\} \quad (2.1)$$

be an ensemble of GPS time series: L is the number of channels — each channel here being a time series — and N the number of data points in each channel. The sampling time Δt is constant, hence $(N - 1)\Delta t$ is the duration of the time series.

The key idea of M-SSA is to exploit the covariance information contained in a series of lagged copies of all $X_l(t)$ over a sliding M -point window (Broomhead and King, 1986a,b; Ghil et al., 2002). In M-SSA one starts therefore by considering the matrix $\tilde{\mathbf{X}}_1$ that includes M time-delayed copies of the original time series $X_l(t)$, written as:

$$\tilde{\mathbf{X}}_1 = \begin{pmatrix} X_l(1) & X_l(2) & \cdot & \cdot & \cdot & X_l(M) \\ X_l(2) & X_l(3) & \cdot & \cdot & \cdot & X_l(M+1) \\ \cdot & \cdot & \cdot & \cdot & \cdot & \cdot \\ \cdot & \cdot & \cdot & \cdot & \cdot & \cdot \\ \cdot & \cdot & \cdot & \cdot & \cdot & \cdot \\ X_l(N') & X_l(N'+1) & \cdot & \cdot & \cdot & X_l(N) \end{pmatrix} \quad (2.2)$$

with $N' = N - M + 1$. Here M is the length of the window used to embed the original time series and it must be chosen to optimize the quantity of information extracted while maintaining satisfactory statistical confidence in that information.

The covariance matrix $\mathbf{T}_{l,l'}$ between two time series $X_l(t)$ and $X_{l'}(t)$ is given by

$$(T_{l,l'})_{j,j'} = \frac{1}{\tilde{N}} \sum_{n=\max(1,1+j-j')}^{\min(N,N+j-j')} X_l(t)X_{l'}(t+j'_j), \quad (2.3)$$

where

$$\tilde{N} = \min(N, N + j - j') - \max(1, 1 + j - j') + 1. \quad (2.4)$$

These matrices are the blocks of a grand covariance matrix $\tilde{\mathbf{T}}$, given by

$$\tilde{\mathbf{T}} = \begin{pmatrix} \mathbf{T}_{1,1} & \mathbf{T}_{1,2} & \cdot & \cdot & \cdot & \mathbf{T}_{1,L} \\ \mathbf{T}_{2,1} & \mathbf{T}_{2,2} & \cdot & \cdot & \cdot & \mathbf{T}_{2,L} \\ \cdot & \cdot & \cdot & \cdot & \cdot & \cdot \\ \cdot & \cdot & \cdot & \mathbf{T}_{l,l'} & \cdot & \cdot \\ \cdot & \cdot & \cdot & \cdot & \cdot & \cdot \\ \mathbf{T}_{L,1} & \mathbf{T}_{L,2} & \cdot & \cdot & \cdot & \mathbf{T}_{L,L} \end{pmatrix}. \quad (2.5)$$

The resolution of the eigenvalue problem

$$\tilde{\mathbf{T}}\mathbf{E}^k = \lambda_k \mathbf{E}^k \quad (2.6)$$

yields the $L \times M$ eigenvalues λ_k and eigenvectors \mathbf{E}^k of $\tilde{\mathbf{T}}$. Each \mathbf{E}^k can be seen as a succession of L segments \mathbf{E}_l^k of length M . We can thus associate a segment \mathbf{E}_l^k to each time series $X_l(t)$. The eigenvectors \mathbf{E}^k are called the spatio-temporal empirical orthogonal functions (ST-EOFs). Each eigenvalue carries a given amount of variance from the overall data set.

2.3.2 Synthetic Example

To illustrate the method, we consider first, for the sake of simplicity, the ten-year long univariate time series plotted in Figure 2.1, with $N = 3652$. This synthetic time series is the sum of an arctangent function that simulates a transient displacement, harmonic functions with annual and semi-annual periods that simulate seasonal oscillations, along with a white noise and a colored noise. The latter is associated with the presence of correlations in the time series and it is chosen to be a stochastic process characterized in the spectral domain by the power law (e.g. Agnew, 1992)

$$S(f) = S_0 \left(\frac{f}{f_0} \right)^{-\alpha}. \quad (2.7)$$

Here $S(f)$ is the spectral density, f is the frequency, P_0 and f_0 are constants and α is the spectral index: the larger α , the faster the roll-off, i.e., the faster the decay of the spectral

2.3. MULTICHANNEL SINGULAR SPECTRUM ANALYSIS (M-SSA)

density with increasing frequency f . For this first synthetic example we choose $\alpha = 0.5$. The variance associated with the colored noise account for 50% of the total noise variance.

We apply M-SSA with $M = 400$ days in order to capture the annual signal contained in the synthetic time series. The resulting singular spectrum in Figure 2.2 displays the eigenvalues calculated by solving Eq. (2.6), sorted in decreasing order and normalized so that they represent their corresponding portion of the total variance of the time series. Note that the singular values μ_k are actually the square roots of the eigenvalues λ_k , i.e. $\mu_k^2 = \lambda_k$. We prefer, though, plotting the λ_k 's, since they sum to unity, but will still refer to the plots as singular spectra, which is the more customary terminology in the M-SSA context.

One observes that most of the variance in the time series is contained in the first six eigenvalues, with a drop and a plateau after the sixth eigenvalue (figure 2.2). These six leading eigenvalues represent the signal contained in the time series, while the lower-order ones correspond to noise. One also notices that eigenvalues 2-3 and 4-5 are forming pairs, which indicate the presence of oscillatory modes (Vautard and Ghil, 1989; Ghil et al., 2002). These results illustrate the capacity of M-SSA to extract periodic components, such as the seasonal signals often present in GPS time series.

In studying a single time series one encounters only temporal EOFs (T-EOFs), while using several time series would have given rise to ST-EOFs, cf. Eqs. (2.5) and (2.6). The five leading T-EOFs are shown in Figure 2.3. Note that T-EOFs 2-3 and 4-5, associated with the two pairs of eigenvalues mentioned above, are in phase quadrature. Such pairs of T-EOFs can be seen as data-adaptive counterparts of the sine and cosine functions in the usual Fourier analysis of time series. The advantage of these pairs over the Fourier sine and cosine functions is to allow the representation of periodic signals with time-varying amplitudes with a few EOFs only (Vautard and Ghil, 1989; Ghil et al., 2002).

The projection of the rows of matrix $\tilde{\mathbf{X}} = (\tilde{\mathbf{X}}_1, \tilde{\mathbf{X}}_2, \dots, \tilde{\mathbf{X}}_l)$ onto the eigenvectors \mathbf{E}_k gives the coefficients $A^k(t)$:

$$A^k(t) = \sum_{j=1}^M \sum_{l=1}^L X_l(t+j-1)E_l^k(j). \quad (2.8)$$

The $L \times M$ vectors $A^k(t)$ are called the spatio-temporal principal components (ST-PCs) in M-SSA or temporal PCs (T-PCs) in the case of univariate data. They are time series of

weighting coefficients associated with their corresponding T-EOFs.

Figure 2.4 shows the five leading T-PCs recovered from the synthetic time series. As for the T-EOFs, T-PCs 2-3 and 4-5 are in phase quadrature, with annual and semi-annual periods, respectively. They capture the seasonal oscillations present in the synthetic time series, while the first T-PC captures the transient displacement.

2.3.3 Signal Reconstruction

The ST-PCs and the ST-EOFs allow us to partially reconstruct the time series $X_l(t)$ (Ghil and Vautard, 1991; Vautard et al., 1992; Plaut and Vautard, 1994). The part of the signal $R_l^k(t)$ associated with the k^{th} ST-EOF and ST-PC is given by:

$$\left\{ \begin{array}{ll} R_l^k(t) = \frac{1}{M} \sum_{j=1}^M A^k(t-j+1)E_l^k(j), & M \leq t \leq N-M+1 \\ R_l^k(t) = \frac{1}{i} \sum_{j=1}^i A^k(t-j+1)E_l^k(j), & 1 \leq t \leq M-1 \\ R_l^k(t) = \frac{1}{N-i+1} \sum_{j=1-N+M}^M A^k(t-j+1)E_l^k(j), & N-M+2 \leq t \leq N. \end{array} \right. \quad (2.9)$$

These partial reconstructions are filtered versions of the original time series and capture a given portion of their total variance. No information is lost in the process since one can reconstruct the full time series by summing the $L \times M$ $R_l^k(t)$.

Figure 2.5 shows the reconstructions of the transient displacement and the seasonal oscillations of our example. They faithfully reproduce the transient and oscillatory signals embedded in the synthetic data.

In summary, M-SSA allows one to decompose time series into statistically uncorrelated components that can be classified into trends, oscillatory patterns, and noise. As shown above with the synthetic example of a transient event, trends need not be linear, as emphasized already by Ghil and Vautard (1991). Moreover, oscillations can be amplitude and phase modulated, as will be shown below.

2.3. MULTICHANNEL SINGULAR SPECTRUM ANALYSIS (M-SSA)

2.3.4 M-SSA versus SSA and PCA

At this stage, we have illustrated the method using a univariate synthetic time series, which only gives rise to temporal EOFs and PCs. This particular case of the more generic M-SSA corresponds to $L = 1$ in Eq. (2.1) and is simply called SSA, cf. Broomhead and King (1986a) and Vautard and Ghil (1989). One can also note that the generic case reduces to the classical Principal Component Analysis (PCA) (Preisendorfer et al., 1981), commonly used in statistical analysis, when $M = 1$ in Eq. (2.2).

M-SSA extracts, however, relevant modes of variability in time series more efficiently when using jointly several time series with correlated information. In this case, M-SSA simultaneously exploits the spatial and the temporal correlations in the time series, which allows for a more efficient separation of noise from trends and oscillatory modes.

We illustrate this point by simulating 15 time series in a manner similar to the one described above, all sharing a common transient signal. We apply M-SSA to ensembles of 1 to 15 of those time series and compute the misfit between the synthetic and reconstructed transient signal. As shown in Figure 2.6A, the misfit systematically decreases as the number of time series that are jointly analyzed increases.

We also illustrate the benefit of using both spatial and temporal correlations jointly over using spatial correlations only, as in the case of PCA, by varying M . Figure 2.6B shows that the misfit is maximum for $M = 1$ (PCA case) and systematically decreases as M increases. These two simple synthetic tests show that simultaneously exploiting spatial and temporal correlations in time series, instead of using only one of them, significantly improves our ability to extract the transient signals embedded in the data.

We varied the spectral index α of the noise introduced in the synthetic time series by using the values of $\alpha = 0, 1$ and 2 . These values correspond to white noise, flicker noise and random walk noise (sometimes called brownian or red noise), respectively, all of which are commonly found in GPS time series (e.g. Williams, 2003). We observe in Figure 2.6 that the transient is captured more easily when α is lower and that separating a transient requires more information, i.e. a larger number L of time series, when α is higher. This type of dependence on α is expected because a higher spectral index means that — for the same

total spectral power, given by $\int_0^\infty fS(f)df$ — the spectral density, cf. Eq. (2.7), will be higher at low frequencies f . This reflects the occurrence of more time-correlated patterns with long correlation times, i.e. more patterns that can be similar to the transient signal.

We also conducted a more realistic multivariate synthetic test that is reported in the appendix. This test was formulated by the Southern California Center (SCEC) community and was also performed by Riel et al. (2014a). It consists in a set of synthetic data simulating time series recorded at cGPS sites in California. These time series contains simulated colored noise, seasonal signals, and transient signals related to a slip event on the Santa Monica fault.

2.4 Application to Transient Deformation of the Akutan Volcano, Alaska

We applied M-SSA to a set of GPS data recorded at the Akutan volcano, Alaska, in order to test the method in the case of GPS position time series. Akutan is an active volcano of the Aleutian arc equipped with 8 continuously operating GPS receivers since late 2006; see maps in Figure 2.7. The data are taken from the Plate Boundary Observatory, <http://pbo.unavco.org/>.

We chose this case because Ji and Herring (2011) were able to identify a transient inflation episode in early 2008 given only a few millimeters of horizontal and vertical displacement, i.e. close to the noise level in the GPS time series. To do so, they first smoothed each time series independently by modeling it as the sum of a constant rate, annual and semi-annual harmonic functions, and a first-order Gauss-Markov (FOGM) process that accounts for temporally correlated noise and transient signal. In a second step, they used a PCA analysis to extract spatially correlated information from the FOGM state estimates. They also removed some of the noise common to all Alaska continuous GPS (cGPS) stations — hence not specific to Akutan’s deformation — by estimating a 7-parameter reference frame transformation to the original time series in a first, pre-analysis, stage.

With this composite method, Ji and Herring (2011) were able to successfully identify

2.4. APPLICATION TO TRANSIENT DEFORMATION OF THE AKUTAN VOLCANO, ALASKA

an inflation event with 1–10 mm of radial horizontal displacement and 0–11 mm of uplift centered on the active crater; this event started in February 2008 and ended 4 months later. Their approach, however, makes a number of a priori assumptions, in particular on the shape of the seasonal oscillations with constant amplitude and on the a priori probability density function of the noise and the transient signal. The fact that they are able to identify a transient likely to be of magmatic origin justifies their hypotheses in this specific case.

We would like to test whether one can also identify this transient inflation event by jointly exploiting the spatial and temporal correlations contained in the data, using the M-SSA on the raw, unfiltered time series, with no pre-processing whatsoever. Moreover, we will show that M-SSA can detect additional inflation events in more recent data, as well as being applicable to much larger data sets.

2.4.1 The GPS Data

We use position time series from cGPS stations of the PBO network, sampled on a daily basis and expressed in the Stable North America Reference Frame (SNARF) (Blewitt et al., 2005). Since the cGPS measure displacement in the northward, eastward, and upward direction, and since there are eight such stations on the island (see Figure 2.7), the number of channels in our M-SSA analysis is $L = 8 \times 3 = 24$.

M-SSA requires that all time series analyzed have the same length. Hence we filled missing data in any of the channels over an interval of length at epoch t_m by using the following model:

$$x(t_m) = at_m + b + \sigma r, \quad (2.10)$$

where $x(t_m)$ is an estimation of the missing data, a and b are the slope and intercept of the regression line, respectively, r is a Gaussian random variable with zero mean and unit standard deviation, while σ is the standard deviation of the available data over an interval of the same length.

Filling gaps in this way is justified by the fact that gaussian noise is not correlated in time or space and is thus going to be seen by M-SSA as part of the noise, rather than of the trends or oscillatory signals (Unal and Ghil, 1995).

We also removed the linear trend in each time series before applying the M-SSA to the dataset. The linear trend, associated with stationary deformation, captures in general the largest proportion of variance in the dataset. Because of this, it is useful to remove it to focus on transient-deformation that account often for much less variance.

2.4.2 Choice of window width M

Before we describe the modes of variability, based on the ST-EOFs and ST-PCs, we discuss the choice of the window width M ; it equals the number of lagged time series used to construct the grand covariance matrix $\tilde{\mathbf{T}}$ and it is a key parameter of M-SSA. M determines, in particular, the length of the ST-EOFs and, therefore, it limits the maximum period of the oscillations that can be extracted from the data, which equals approximately $M\Delta t$.

The optimal value of M is a trade-off between the statistical significance of the extracted modes and the maximum period of the oscillations one aims to extract. The larger the N/M ratio — i.e., the smaller the value of M — the larger the statistical significance of the extracted modes (Ghil et al., 2002). This is so because the uncertainty associated with the estimation of the covariances decreases as the number of points used in the estimation, i.e. $N - M + 1$ — increases. On the other hand, extracting the annual signal present in the GPS time series obviously requires that M be greater than 365 days.

We applied M-SSA to the 8 GPS time series recorded at Akutan volcano from late 2006 to early 2014, for a total of 3000 data points in the three displacements — N-S, E-W and up-down — and obtained the singular spectra shown in Figure 2.8. The singular spectra in the figure were obtained for 3 different values of M : 400, 500, and 600 days. The three spectra show a similar shape, with a first eigenvalue well above the others and accounting for a large portion of the data variance. It is followed by a first plateau formed by two eigenvalues for $M = 400$ or three eigenvalues for $M = 500$ and $M = 600$. Vautard and Ghil (1989) already noticed that, as M increases, the same feature in the spectrum will require a larger number of modes to be described fully.

All three spectra show a second plateau, sloping down to a third one that ends at eigenvalue 15. The ST-EOFs and ST-PCs for these value of M are plotted in Figures 2.10

2.4. APPLICATION TO TRANSIENT DEFORMATION OF THE AKUTAN VOLCANO, ALASKA

and 2.9, respectively. They also show similar shapes, for instance the letter-M-like trend visible in the first ST-PC for all values of the window width M , cf. Figure 2.9.

The similarity of the spectra, together with the robustness of the shape of the ST-EOFs and ST-PCs, suggests that they capture the same dynamic processes. This parametric robustness — in addition to standard statistical significance tests — gives us further confidence in the extracted modes being physically meaningful (Ghil et al., 2002, Section 5.2). In the following, we will discuss results obtained with $M = 400$.

2.4.3 Singular Spectrum, ST-EOFs and ST-PCs

The ST-PCs associated with the first eleven eigenvalues are plotted in Figure 2.9. We observe that the first ST-PC describes 6% of the total variance of the data set and corresponds to an M-shaped trend and a relatively long-periodic temporal variability. ST-EOFs 2 and 3 carry 7% of the variance and, as shown in Figure 2.10, they are in phase quadrature. They form a pair that captures an oscillatory component of annual period and represents 7% of the total variance (Figure 2.9).

ST-PCs 4, 5 and 8, together with ST-PC 1, capture the trend with non-constant slope; this triplet contains 4% of the variance, for a total of 12% in the data-adaptive trend. ST-PCs 6–7 and ST-PCs 9–11 form two pairs that together capture an oscillatory component of semi-annual period; together, these four ST-PCs contain 6% of the data variance (Figure 2.9). ST-PC 10 captures also an oscillatory component with mostly annual period and contains 1% of the data variance.

2.4.4 Testing the statistical significance of the extracted modes

As first pointed out by Allen and Smith (1994), colored noise in geophysical time series can lead to the false detection of modes that resemble those of geophysical origin when applying the M-SSA. To make sure that the modes that we consider when reconstructing our time series are not associated with colored noise, appropriate tests of statistical significance have to be applied.

Monte Carlo SSA (MC-SSA) was first proposed by Allen and Smith (1994) as such a test

for the univariate SSA and then extended by Allen and Robertson (1996) to the multivariate case. This test helps discriminate between the modes associated with signals and those associated with noise. MC-SSA relies on constructing sets of “surrogate data” (Theiler et al., 1991) and it allows one to formulate several distinct null hypotheses.

The main idea of MC-SSA is to compare the partial variances in the dataset being analyzed, in the directions spanned by its ST-EOFs, with the corresponding variances resulting from a particular null hypothesis. The null hypothesis here takes the form of an ensemble of surrogate data \mathbf{X}_R of the same length N and dimension L as the dataset we wish to analyze.

The partial variances of the null hypothesis in the directions defined by the ST-EOFs \mathbf{E}^k are estimated by the diagonal elements of

$$\Lambda_R = \mathbf{E}' \tilde{\mathbf{T}}_R \mathbf{E}. \quad (2.11)$$

Here \mathbf{E}' denotes the transpose of the matrix \mathbf{E} whose $L \times M$ columns are the ST-EOFs \mathbf{E}^k deduced from the covariance matrix of the data via equation (2.6), and $\tilde{\mathbf{T}}_R$ is the covariance matrix of the null hypothesis, calculated using the ensemble of surrogate data \mathbf{X}_R and equation (2.3).

By calculating Λ_R for a sufficiently large ensemble of surrogate data, one can estimate confidence intervals for the diagonal elements of Λ_R . If the eigenvalues of the data covariance matrix lie inside or below these confidence intervals, we conclude that the associated modes are not significant with respect to the null hypothesis under consideration.

This test, however, turns out to be too lenient in the multivariate case; in particular when the covariance matrix $\tilde{\mathbf{T}}$ deduced from the data is rank deficient, i.e. when $L \times M \gg N$ (Allen and Robertson, 1996). This limitation, however, can be overcome by an improvement of the test proposed by Groth and Ghil (2015b). The M-SSA results reported in the following use the improved MC-SSA algorithm of Groth and Ghil (2015b).

The difficulty in this kind of test is the choice of the null hypothesis against which the data are tested. Here we choose to test only the statistical significance of the first eleven modes described above and represented in Figure 2.9. It is indeed amongst these modes

2.4. APPLICATION TO TRANSIENT DEFORMATION OF THE AKUTAN VOLCANO, ALASKA

that we identified the different signals that are discussed in the next sections of the paper.

The surrogate data are therefore constructed in two steps. First, we reconstruct the GPS time series using all ST-EOFs and ST-PCs except the first eleven ones. In other words, we reconstruct the time series using equation (2.9), with k ranging from 12 to $L \times M$. In the second step, we add to these reconstructed time series a noise model against which we wish to test the significance of the first eleven modes. Here, two canonical types of noise models are considered : flicker noise with $\alpha = 1$ and random walk noise with $\alpha = 2$. These two types of colored noise are often considered to be present in GPS time series (e.g. Williams, 2004).

Figure 2.11 shows the MC-SSA test results. Error bars represent the two-sided 95% confidence intervals derived from 500 realizations of the surrogate data set, and we concentrate on the first eleven eigenvalues. For the null hypothesis that contains flicker noise (Figure 2.11 A), only eigenvalues 5 and 8 lie within the error bars. They are, however, relatively close to the upper ticks of their associated error bars, i.e. to the 97.5% quantile, and especially so in the case of the eighth eigenvalue, which lies almost on the upper tick. In this case, for eigenvalues 5 and 8, our test does not reject the null hypothesis. However, the proximity of the eigenvalues to the upper tick may be indicative of a type II error, or false negative.

For the MC-SSA test against random walk noise (Figure 2.11 B) eigenvalues 5 and 8 clearly lie within their associated error bars. Hence ST-EOFs 5 and 8 and the corresponding ST-PCs (figure 2.9) may have been generated by the presence of random walk noise in the data set and are consequently not used to reconstruct the signals considered in the next sections.

2.4.5 Seasonal Signals

Seasonal signals with annual and semi-annual periods are ubiquitous in GPS position time series, and are known to be caused in a large part by mass transport and redistribution in the atmosphere, oceans, and continental water reservoirs, whose load triggers deformation of the Earth surface that is measurable with space-geodetic techniques (e.g., van Dam and

Wahr, 1998; Dickey, 2002; Bevis et al., 2005; Fu et al., 2012).

Seasonal signals contain important geophysical information on the rheological structure of the Earth's crust and mantle (Chanard et al., 2014) and on the spatio-temporal characteristics of the load (e.g. Blewitt, 2001; Heki, 2004). They must, therefore, be extracted as objectively as possible from the data.

However, our ability to extract transient deformations from GPS time series depends on our capacity to identify correctly the seasonal signal, since, the transients we are interested in may share some of the characteristics of seasonal signals. In particular, the spectral content of the seasonal and transient signals may overlap, which renders classic time series analysis based on the Fourier transform unsuitable. Thus, for instance, Heki (2004) showed that Fourier analysis of interannually modulated seasonal oscillations may yield transient-like residuals.

Seasonal signals in GPS time series are commonly modeled using the sum of sinusoidal functions with annual and semi-annual periods fitted to the data, which provides an estimate of their phase and amplitude. This procedure is efficient in the case of purely harmonic signals but cannot account, for instance however, for interannual amplitude modulations or asymmetric oscillations, two characteristics that often are present in actual GPS time series (Heki, 2004).

M-SSA has long been used in meteorology and climatology to extract such anharmonic and amplitude-modulated oscillatory modes of variability for the atmosphere and oceans (e.g., Keppenne and Ghil, 1993; Plaut and Vautard, 1994; Unal and Ghil, 1995; Jiang et al., 1995). Here we take advantage of this capacity of M-SSA to extract and reconstruct the seasonal signal present in GPS time series without constraining a priori their period, shape, or time-dependent amplitude.

Figure 2.10 shows the pair of ST-EOFs 2-3 that captures the annual oscillations in the Akutan GPS time series. The phase quadrature between the two members of the pair emphasizes their being data-adaptive counterparts of the fixed sine and cosine basis functions of Fourier transforms. Their main advantage is that these two ST-EOFs alone describe the annual oscillations in the $L = 24$ time series and their interannual amplitude variation (Ghil

2.4. APPLICATION TO TRANSIENT DEFORMATION OF THE AKUTAN VOLCANO, ALASKA

et al., 2002, and references therein). The three panels of the figure show very small differences in results for the window widths $M = 400, 500$ and 600 days, a finding that supports the robustness of the M-SSA results. ST-EOFs 6-7 and 9-11 (not shown) jointly capture the semi-annual variability.

The vertical component of the annual signal in Figure 2.9 is weaker than its horizontal components. The weakness of the vertical component is consistent with Akutan being an island of small size, where vertical deformation caused by atmospheric or hydrological loading — the latter in the form of continental water or snow — is expected to be small (van Dam and Herring, 1994). In such a setting, nontidal ocean mass loading, unaccounted for in the cGPS analysis used here, should represent the largest contribution to seasonal deformation (Munekane and Matsuzaba, 2004).

The reconstructed series using the combination of ST-EOFs 2-3, 6-7, and 9-11 and the corresponding ST-PCs (Figure 2.9) together capture well the seasonal oscillations that are readily apparent in the data, as shown in Figure 2.12. In spite of the small number of ST-EOFs used, the reconstructed time series exhibits fairly complex waveforms; in particular, a lower-amplitude episode in the vertical component of the seasonal signal rightmost column in Figure 2.12 is shared in 2009 by all the stations. This lower-amplitude episode is also visible in Figure 2.13 for the specific site AV10.

We find, in fact, that this modulation is present in the semi-annual oscillations associated with ST-PCs 6-7 but not in those associated with ST-PCs 2-3 and 9-11, an observation that may indicate that the ST-PC pair 6-7 captures a specific dynamic process that is different from the one captured by ST-PCs 2-3 and 9-11. Further investigation of these seasonal signals and their multi-annual modulation is beyond the scope of the present paper but our observations illustrate that M-SSA can extract information relevant to the dynamics and the physics driving these signals.

We compare in Figure 2.13 the seasonal signals extracted using M-SSA from the three components recorded at station AV10, on the one hand, with a curve fit to the data that uses the classical four-term Fourier series

$$x(t) = A_1 \cos(2\pi t) + A_2 \sin(2\pi t) + B_1 \cos(\pi t) + B_2 \sin(\pi t), \quad (2.12)$$

on the other. Here A_1 , A_2 , B_1 , and B_2 are the coefficients for the annual and semi-annual terms estimated from the daily positions $x(t)$, and the fits were done for each one of the three components — north, east, and up — separately.

The difference between M-SSA reconstructions of the seasonal oscillations and the four-term Fourier expansion is most pronounced for the vertical component, which shows interannual modulations of larger amplitude. Furthermore, the M-SSA reconstruction and four-term Fourier estimates for the seasonal oscillations in the vertical are not always exactly in phase, since the coefficients $A_{1,2}$ and $B_{1,2}$ are constant, and thus the phase as well as the amplitude is constant, while the M-SSA results have both phase and amplitude modulation.

In addition, the reconstruction of the seasonal modes and their interannual modulations owes to ST-PCs 2–3 and 6–7 for the vertical but ST-PCs 2–3 and 9–11 for the horizontal components. This shows that M-SSA is able to extract annual, semi-annual, and interannual oscillations with actually fewer parameters than a least-squares fit to a Fourier for which at least six sinusoidal functions would have been necessary to account for such variability.

These observations show that the M-SSA reconstructions faithfully capture the interannual variability of the seasonal oscillations, with respect to both amplitude and phase modulation. This pluri-annual modulation of the seasonal signal identified by M-SSA may be indicative of multi-annual oscillations in the regional hydro-climatic regime; see Ghil and Robertson (2002) and references therein, including, in particular, Wallace and Gutzler (1981).

2.4.6 Transient Signals

We now focus on ST-PCs 1 and 4 (Figure 2.9), which carry the data-adaptive trend shared by all 24 GPS time series at Akutan volcano. These ST-PCs together capture 11% of the total variance in the data set (Figure 2.8) and are associated with transient behavior, mostly described by the shape of ST-PC 1. This transient is shown by the reconstructions in Figure 2.14.

The M-SSA-filtered time series (red curves in the figure) display a transient deformation

2.4. APPLICATION TO TRANSIENT DEFORMATION OF THE AKUTAN VOLCANO, ALASKA

event starting in early 2008 and lasting for about a half a year. This transient event is similar in shape and duration to the one identified by Ji and Herring (2011), and it is visible in Figure 2.14 at all 8 sites and in all 3 directions of motion; the amplitude of the motion and its direction vary, though, from site to site.

The event is already visible in some of the raw time series, such as the northward component at AV12, or the eastward component at AV07. But its shape and duration in the raw data, where all the signals and the noise are mixed, sometimes resemble part of a seasonal cycle — e.g., in the eastward component at AV12 — or a sharp step function that could be mistaken for an equipment problem — e.g., in the northward component at AV10.

In Figure 2.15, we consider four transient episodes dominated by vertical uplift. We compare the associated ground motions (red arrows in the figure) with those given by a calculation that uses the simple model of a point source volume change, simulating a magma chamber, embedded in an elastic half-space (blue arrows in the figure). Such a model — also used by Ji and Herring (2011) — was first proposed by Mogi (1958) as a simple way of calculating surface deformation in active volcanic systems.

The spatial representation of the site displacements from 2008.0 to 2008.7 in Figure 2.15A shows that this event is associated with a radial extension and uplift centered on the volcano, with amplitudes decreasing outward. This is consistent with the observations reported by Ji and Herring (2011) and validates the extraction of this transient by M-SSA.

Figures 2.15A–D also show other features shared amongst the filtered time series, across the four episodes, although these features are more subtle than the one described above. We observe that the first transient, from 2008.0 to 2008.7 (panel A), is followed at all sites by another monotonic trend with an opposite slope, from 2010.5 to 2010.8 (panel B), then by a shorter monotonic trend, from 2010.8 to 2011.5 (panel C), with the same slope as in panel A. Finally, we observe fourth monotonic trend, from 2011.5 to the end of the data used here (panel D), whose slope is again opposite to the previous one.

The amplitudes and slopes of these trends vary from site to site: they are subtle and very difficult to see in the raw time series, in particular in the noisier vertical component, where they are buried in the noise but still extracted by our M-SSA analysis. The match

between the horizontal component of the raw series and the filtered reconstruction, though, is readily visible at those sites and for those components for which the amplitude of these trends is relatively large, such as the eastward component at AV07, the northward component at AV12 or the eastward component at AV13.

The site displacements associated with the three following transients are plotted in panels B, C and D of Figure 2.15. They also show a well-organized pattern of radial contraction (episode 2), extension (episode 3), and compression (episode 4), associated with subsidence, uplift, and subsidence, respectively. All three events have amplitudes of less than 4 mm, i.e., they are much smaller than the first. Event 3 is the least pronounced one, with displacements that do not exceed 2 mm. In spite of these very small displacements, their common features — to wit, the radial pattern centered on the volcano, the good correlation between horizontal and vertical components, and the decreasing amplitudes with distance from the volcano summit reinforce our confidence that they represent a signal of geophysical origin rather than noise.

We are, therefore, observing — over the roughly 8 years of data analyzed — two cycles of uplift and radial extension, followed by subsidence and radial contraction, and both cycles consistently display features that strongly suggest a magmatic origin. We test this hypothesis by running a series of ‘Mogi models’, as described above, for each of the four transient deformation episodes. For each episode we vary the depth and volume change of the source, while its horizontal position is kept constant at the latitude and longitude used by Ji and Herring (2011). Figure 2.16 shows that the minimum misfit between model and data analysis results is obtained for a source located at a depth of close to 8 km for all four sources. The fact that a single source location can describe all four transient events is a strong indication that they are, indeed, of magmatic origin and, therefore, that the very small transients extracted by M-SSA are indeed representative of a geophysical signal.

2.5 Discussion

2.5.1 Implications for Transient Detection in Large GPS Networks

We have so far been using GPS stations located within roughly 25 km of each other and thus strong spatial and temporal correlations are expected, making M-SSA particularly efficient at extracting common modes of variability from the data. We now address the question of whether the transient signal described above would have been detected across a larger station footprint and with no a priori information on its location.

The latter situation is particularly relevant given the large number of GPS stations now commonly deployed across wide areas. Visually combing through these large data sets for transient events is becoming more and more difficult and it is necessary therefore to develop automated approaches to identifying geophysical signals in a systematic and objective way.

We applied, therefore, M-SSA to GPS position time series from 80 sites distributed across Alaska, including those on the Akutan volcano; Their geographical distribution is plotted in Figure 2.17A. The computational burden increases rapidly because of the dimension of the spatio-temporal lag covariance matrix $\tilde{\mathbf{T}}$, which is $(L \times M)^2$. We then resampled the data weekly. It allows us to reduce the window width M without making the ST-EOFs length smaller than 365 days which is necessary to extract the seasonal oscillations as explained in section section 2.4.2. The M-SSA analysis proceeds the same way as described in Section 2.4 above and it produces six leading ST-PCs, shown in Figure 2.17B; this set of ST-PCs describes 31% of the data variance.

We observe that over such a large spatial scale the first two ST-PCs correspond to an oscillatory component with an annual period, while the remaining four ST-PCs represent trends. The time series reconstructed using these trends, plotted in Figure 2.18, display the same transients as described above using the 8-site M-SSA of Figure 2.9. The corresponding site displacements, plotted in Figure 2.19, stand out as a local anomaly at the scale of Alaska. The displacements over Akutan, as obtained by the Alaska-wide M-SSA analysis, are plotted in Figure 2.20. They show a radial pattern of extension as seen by the M-SSA

with the 8 sites on Figure 2.15 A.

Having applied M-SSA to 80 GPS stations covering a large footprint, we thus found that the method is still able to identify common modes of variability at the specific location of the Akutan volcano. As a consequence, applying M-SSA to the uncorrected raw data of a regional network of stations — i.e., without removing a seasonal signal, modifying the frame of reference, or assuming a given set of noise characteristics — should allow one to detect statistically significant local anomalies. Such anomalies can then be further investigated by zooming in on them and verifying that the corresponding spatial patterns are consistent with a geophysical process (e.g. Ji and Herring, 2011). This result opens the way for the automated detection of transient events in large GNSS networks.

2.5.2 Noise Extraction from GPS Time Series

Noise in GPS position time series is temporally correlated with more power at low frequencies than at high frequencies (e.g. Zhang et al., 1997; Mao et al., 1999; Williams, 2003). The power spectrum of GPS time series on the Akutan volcano (grey lines in Figure 2.21) follows this characteristic behavior with a slope of roughly -1 of the spectral density at high frequencies indicative of temporally correlated noise.

Such temporal correlations can lead to time-dependent patterns similar to geophysical signals, in particular when the spectral index is greater than one (Agnew, 1992); see also the discussion of the spectral index α in Section 2.3.2, cf. Equation (2.7) and Figure 2.6. It is clear from the figure, furthermore, that the power spectrum of the raw time series at low frequencies is not flat and includes the contributions from trends and oscillatory signals described above.

We take advantage of the ability of M-SSA to extract common modes of variability amongst time series jointly in space and time. In particular, we do expect it to discriminate between the spectral content associated with time-dependent noise, on the one hand, and signals such as transient deformation and seasonal motions, on the other hand.

This expectation is tested in Figure 2.21, where black lines show the power spectrum of the noise, i.e., the raw time series minus the reconstruction of the transient plus the

2.5. DISCUSSION

seasonal signals. We observe that the noise carries much less low-frequency variance than the raw time series, and that its spectrum is quite flat at low frequencies. This finding confirms our expectation that the low-frequency part of the raw-data spectrum (grey lines in Figure 2.21) is mostly due to the sum of the seasonal and transient signals extracted by M-SSA. The high-frequency content of the residual time series is, however, unaffected, with a slope identical to that of the raw data. This shows that M-SSA act here as a low-pass filter.

The power spectra of the reconstructed seasonal oscillations in Figure 2.12 are plotted in red in Figure 2.21. Two well-defined peaks are visible at annual and semi-annual periods. The transient signal also contributes to the variance present at these periods but M-SSA is able to unravel the spectral content associated with these transients from the one associated with the seasonal oscillations.

This efficient extraction of trends, oscillatory modes, and noise by M-SSA is possible because the method captures the different temporal and spatial scales of the physical processes responsible for the generation of the time series.

2.5.3 M-SSA, GPS Time Series and Nonlinear Dynamical Systems

The idea that time series analysis could be applied to extract information about underlying nonlinear dynamical systems was proposed by Mañé (1981) and by Takens (1981a). Broomhead and King (1986a,b) and subsequent authors (Vautard and Ghil, 1989; Ghil and Vautard, 1991; Vautard et al., 1992) reformulated the early “method of delays” in the setting of the classical Karhunen-Loève representation of time series, as reviewed by Ghil et al. (2002), which is at the basis of the M-SSA methodology.

Single-channel SSA and M-SSA have thus been linked to the framework of nonlinear dynamical system theory. This connection helps explain the fact that M-SSA allows one to extract physically relevant modes of variability common to several GPS time series because these modes reflect the structure of the underlying attractor.

This make the M-SSA particularly suitable to analyse GPS time series generated by geophysical nonlinear dynamical systems and a fortiori by volcanoes. Volcanoes are intrinsically chaotic nonlinear dynamical systems as highlighted by Sparks (2003). The processes

often invoked to explain inflations and subsidences observe with geodetic data are cristallisation, melting and gaz exsolutions along with the dynamic of the hydrothermal systems (e.g., Caricchi et al., 2014). All these phenomenons can be coupled with each others and account (among others) for the nonlinearity of volcanic systems (Sparks, 2003).

The deformation of the Akutan volcano that has been extracted with the M-SSA reflect well this nonlinear dynamic. They are cyclic – we observe successions of inflations and subsidences – but not periodic. This kind of chaotic behavior arise typically from nonlinear dynamical systems that have at least three degrees of freedom as first shown by Lorenz (1963a) in his famous paper.

GPS time series can obviously provide information not only on magmatic processes — as shown here — but also on tectonic, hydrological, and seismological processes that affect systems constituted of faults, volcanoes, crust, and mantle. Such systems are complex and can be seen as well as nonlinear dynamical systems for which we often have limited knowledge of the physics that precisely controls their evolution in time.

Regardless of this limitation, M-SSA allows us to efficiently and objectively separate processes and to rank them as a function of their importance, i.e. of the fraction of variance in the observed time series that they generate. Some of these processes correspond to what is classically considered as the “signal,” i.e. as the deterministic part, while others correspond to what is classically considered as “noise,” i.e. as the stochastic part.

2.6 Conclusion

We have shown that M-SSA allows us to extract signals of geophysical significance from GPS position time series and to efficiently separate them from noise. The data-adaptive nature of the method results in a simple and parsimonious representation, using only a few spatio-temporal EOFs (ST-EOFs) to describe complex spatio-temporal fluctuations, such as anharmonic oscillations and trends with non-constant slopes. This representation is achieved without any a priori assumptions on the stochastic characteristics of the noise or on the cause of the underlying physical processes.

Like other methods, M-SSA is sensitive to the quality of the data. In particular, the

2.7. APPENDIX: SOUTHERN CALIFORNIA EARTHQUAKE CENTER (SCEC) VALIDATION EXERCISE

presence of colored noise can lead to the occurrence of modes that resemble those of geophysical origins. We have shown however that hypothesis tests, such as the MC-SSA, help us to discriminate between modes associated with correlated noise and modes associated with signals. The presence of discrete offsets, due for example to equipment changes at the GPS sites can also lead to bad reconstructions of the time series. Visual inspection of the data may, therefore, be necessary, although new techniques are being proposed to automatically detect and correct such shifts in time series (Montillet et al., 2015; Tran, 2013).

An other limitation of the M-SSA is that the size of the $(M \times L)^2$ lag-covariance matrix $\tilde{\mathbf{T}}$ grows rapidly with the size of the GPS network considered. This can lead to computational issues in solving the eigenvalue problem described in Eq. (2.6).

Despite these limitations M-SSA presents an attractive alternative to existing methods to objectively extract information embedded in geodetic time series. Its ability to filter and compress the information contained in GPS time series through the calculation of robust and parsimonious representations opens the perspective to use it as a tool to detect signals hidden in the large amount of geodetic data now available worldwide.

2.7 Appendix: Southern California Earthquake Center (SCEC) validation Exercise

We test the M-SSA on a realistic synthetic multivariate data set. This data set contains synthetic GPS time series generated by the fakenet package (Agnew, 2013). This exercise was created by the SCEC community and was also performed by Riel et al. (2014b). It consists in a set of synthetic data simulating time series recorded at cGPS sites in California. These time series contains colored noise of different types and amplitudes, seasonal signals and transient displacements signals related to a thrust event on the Santa Monica fault.

Before applying the M-SSA to the data set we applied the procedure explained in section 3.1. Figure S1 shows the first 6 ST-PCs obtained from application of the M-SSA on the East and North components recorded at 60 cGPS stations around the Santa Monica fault. Some segments of the fault, on which the simulated thrust occurred, are represented in figure

S3. ST-PCs pair 1-2 capture the annual seasonal signal while ST-PC pair 5-6 capture the semi-annual seasonal signal. Together these two pairs carry $\sim 50\%$ of the dataset variance. ST-PCs 4 and 5 describe the data-adaptive trend of the time series and contains $\sim 15\%$ of the total variance. It can readily be seen from ST-PCs 4 and 5 that a transient signal emerges around 2002.

Figure S2 shows some of the reconstructed time series that uses ST-PCs 4-5 and their corresponding ST-EOFs. These reconstructions are compared with their corresponding time series (black dots) and the signal related to the thrust event (blue lines).

The spatial representation of the horizontal displacements at some cGPS sites are shown in figure S3. The M-SSA derived transient displacements (red arrows) are consistent with the synthetic displacements associated with the simulated thrust event (blue arrows).

2.8 Figures

2.8. FIGURES

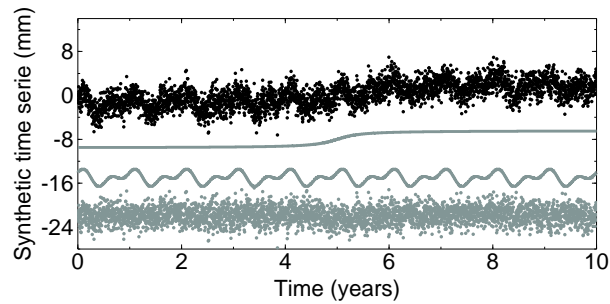


Figure 2.1: Univariate synthetic time series (black dots) composed of, from top to bottom in gray, a transient displacement, annual and semi-annual harmonic functions, as well as colored and white noise.

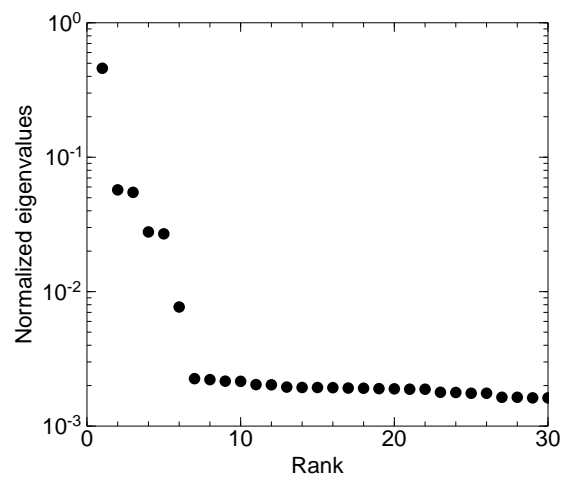


Figure 2.2: Singular spectrum of the synthetic time series shown in Figure 2.1. Eigenvalues are normalized to represent the appropriate fraction of the total variance of the time series, and they sum to 1.

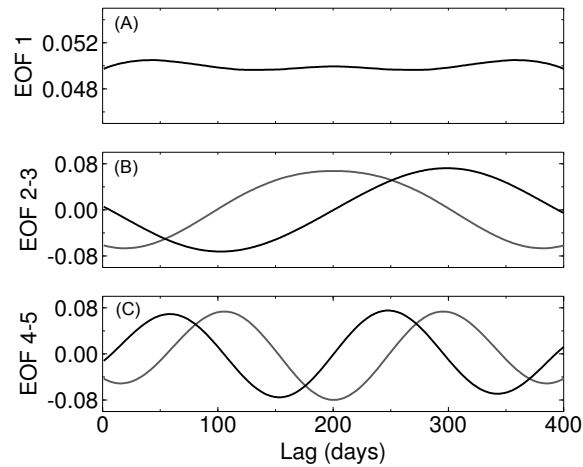


Figure 2.3: The five leading temporal empirical orthogonal functions (T-EOFs) extracted from the synthetic time series; they are associated with the first five eigenvalues in Figure 2.2.

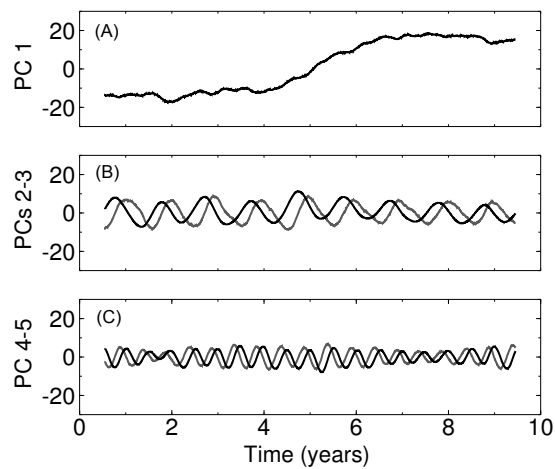


Figure 2.4: The five leading temporal principal components (T-PCs) associated with the five T-EOFs of Figure 2.3. These T-PCs are time coefficients that weigh the corresponding T-EOFs in reconstructing the original time series; they represent the different modes of variability of the time series.

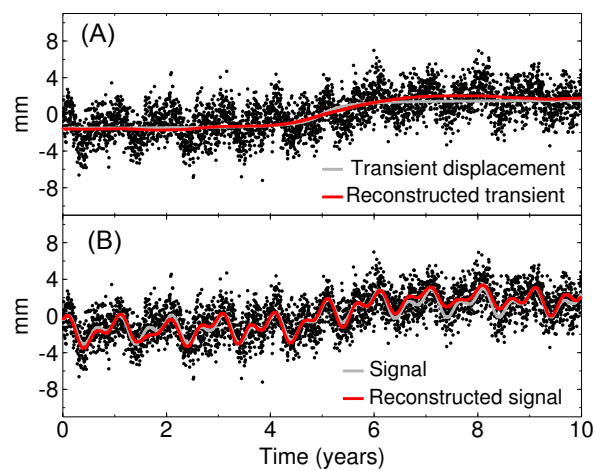


Figure 2.5: Reconstruction of the transient displacement (top panel) and the seasonal oscillations (bottom panel) in our synthetic example. Black dots = synthetic time series, grey lines = synthetic transient and oscillatory signals embedded in the synthetic time series, red lines = reconstructed signals using M-SSA. Top: the reconstruction using the first T-PC and corresponding T-EOF captures the transient displacement signal. Bottom: the reconstruction using the first five T-PCs and corresponding T-EOFs additionally captures the seasonal signal.

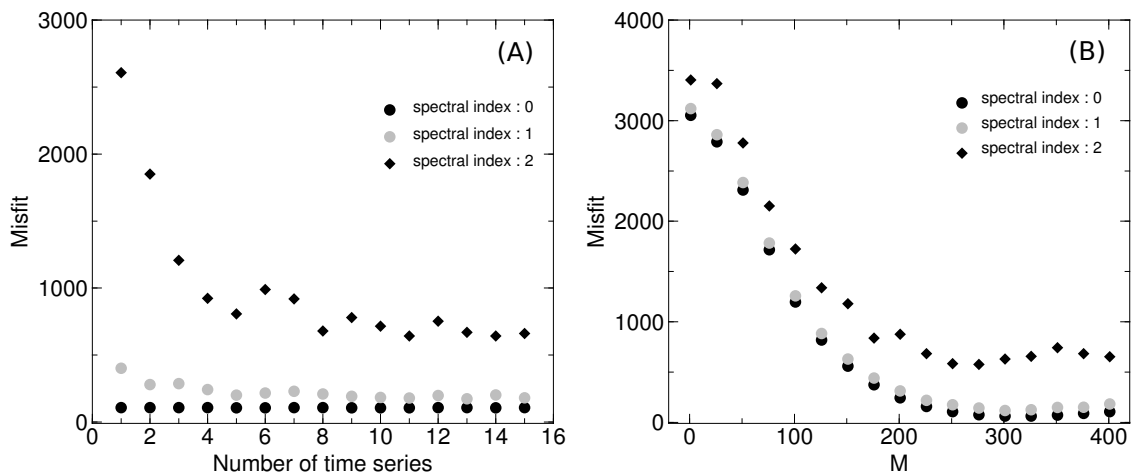


Figure 2.6: Evaluation of the improvement in M-SSA reconstruction as a function of (A) the number L of time series and (B) of window width M . (A) Misfit between the synthetic transient signal and its reconstruction versus the number L of synthetic time series used in M-SSA. (B) Misfit between the synthetic transient signal and its reconstruction versus M , the maximum lag used to compute the covariance matrix. All the synthetic time series are similar to the one in Figure 2.1 and share the same transient displacement. Black dots correspond to the results of an experiment that uses a white noise ($\alpha = 0$), while gray dots correspond to colored noise with a spectral index of $\alpha = 1$ and black diamonds correspond to a noise with a spectral index of $\alpha = 2$. The separating power of M-SSA improves as the number of the series sharing a transient signal increases as well as M increases.

2.8. FIGURES

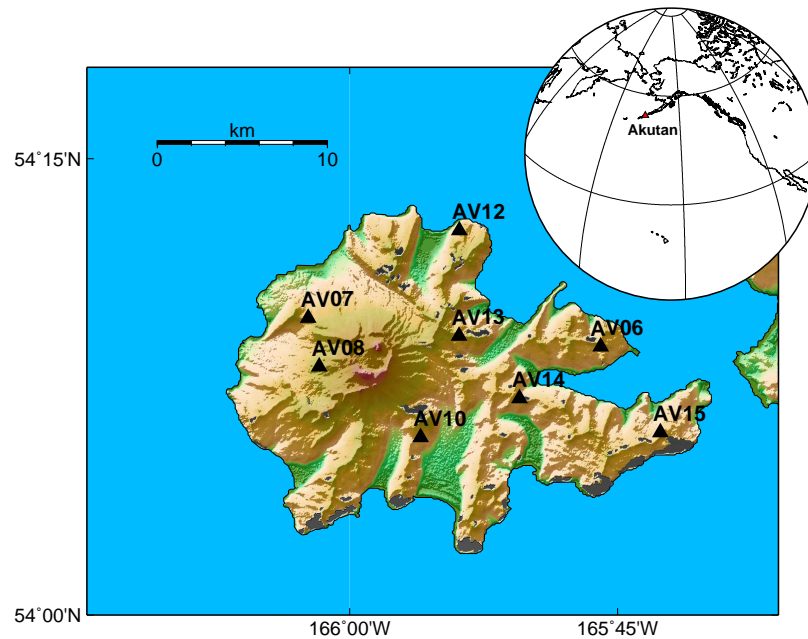


Figure 2.7: Maps showing the location of the Akutan volcano within the Aleutian arc (inset) and of the eight continuously recording GPS receivers (black triangles) used in this study on the island (main map).

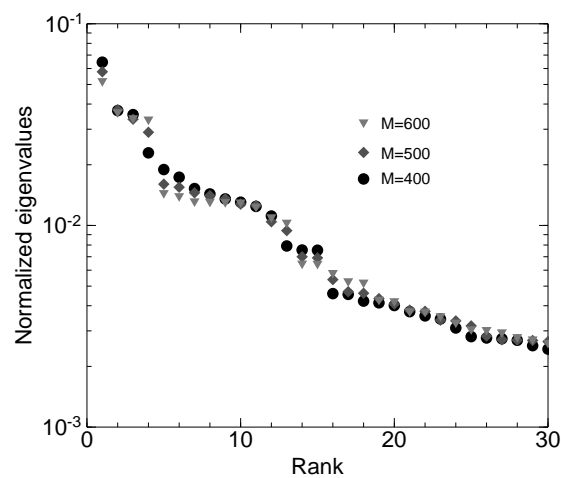


Figure 2.8: Singular spectrum of the GPS position time series at 8 cGPS sites on Akutan volcano from early 2006 to late 2014. The first 30 M-SSA eigenvalues are plotted for the window widths $M = 400, 500,$ and 600 days. Eigenvalues are normalized as in Figure 2.2, so that their sum is unity.

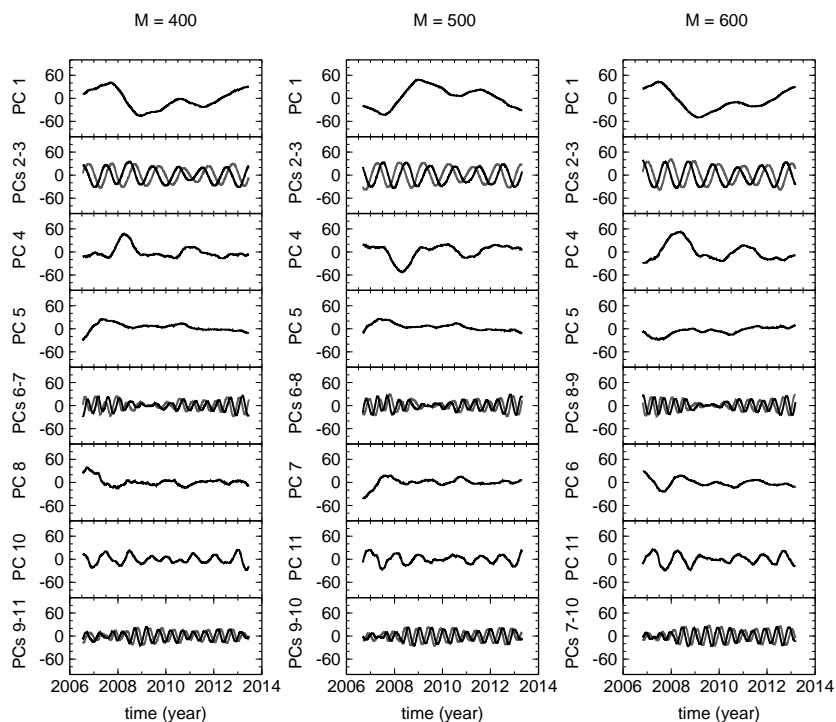


Figure 2.9: The eleven leading ST-PCs associated either with the trend with non-constant slope or the seasonal oscillations. They are calculated using (A) $M = 400$, (B) $M = 500$, and (C) $M = 600$ days. The persistence of the shape of the ST-PCs for the different values of M — ignoring the occasional change of sign, which is a numerical artefact of PCA in general — is an indicator of the significance of the extracted modes. Regardless of the value of M , ST-PCs 1, 4, 5 and 8 jointly capture the data-adaptive trend, while the ST-PC pair 2-3 represents the annual oscillations. The four ST-PCs 6-7 and 9-11 capture the semi-annual oscillations for $M = 400$, whereas this mode is captured by ST-PCs 6-7 and 9-10 for $M = 500$ and ST-PCs 8-10 and ST-PCs 6-9 for $M = 600$.

2.8. FIGURES

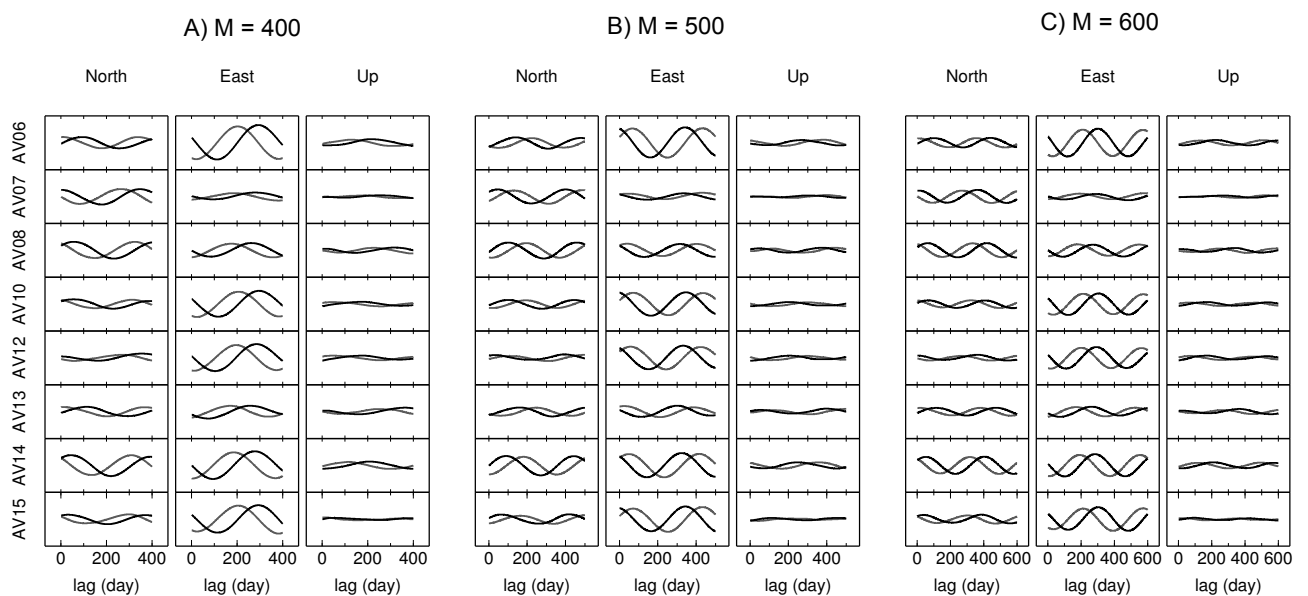


Figure 2.10: Spatio-temporal empirical orthogonal functions (ST-EOFs) associated with eigenvalues 2 (black) and 3 (gray) (see Figure 2.8) calculated using (A) $M = 400$, (B) $M = 500$, and (C) $M = 600$ days. The subpanels show the components of these EOFs for each cGPS site and each direction of motion being measured. These two ST-EOFs capture the annual oscillatory mode of annual period present in the data. The differences between estimates using different values of M are small.

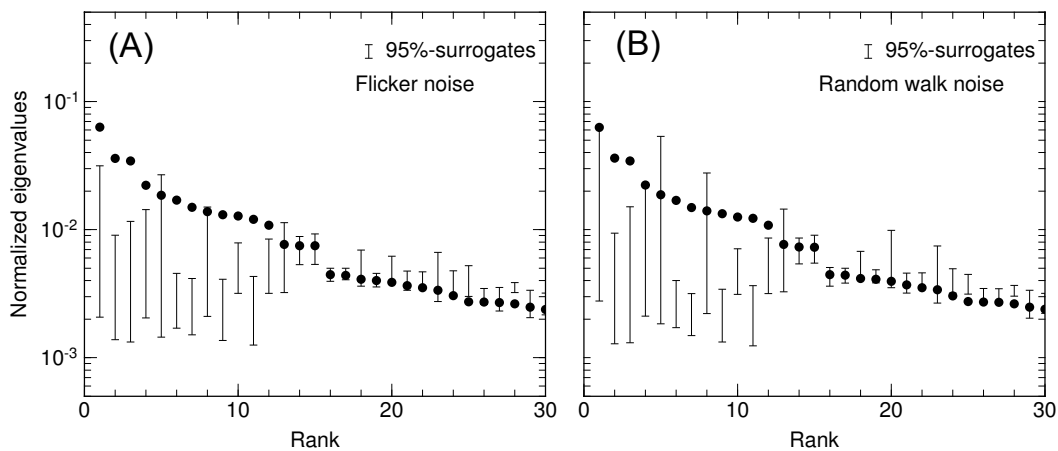


Figure 2.11: MC-MSSA test of statistical significance using surrogate data containing (A) flicker noise, with spectral index $\alpha = 1$; and (B) random walk noise noise, with $\alpha = 2$. Lower and upper ticks on the error bars correspond to the 2.5% and 97.5% quantiles of an ensemble of 500 surrogate data that are different realizations of the null hypothesis under consideration. These tests show that modes associated with eigenvalues 5 and 8 that lie within the corresponding confidence intervals are possibly generated by the presence of colored noise in the GPS time series recorded at Akutan volcano.

2.8. FIGURES

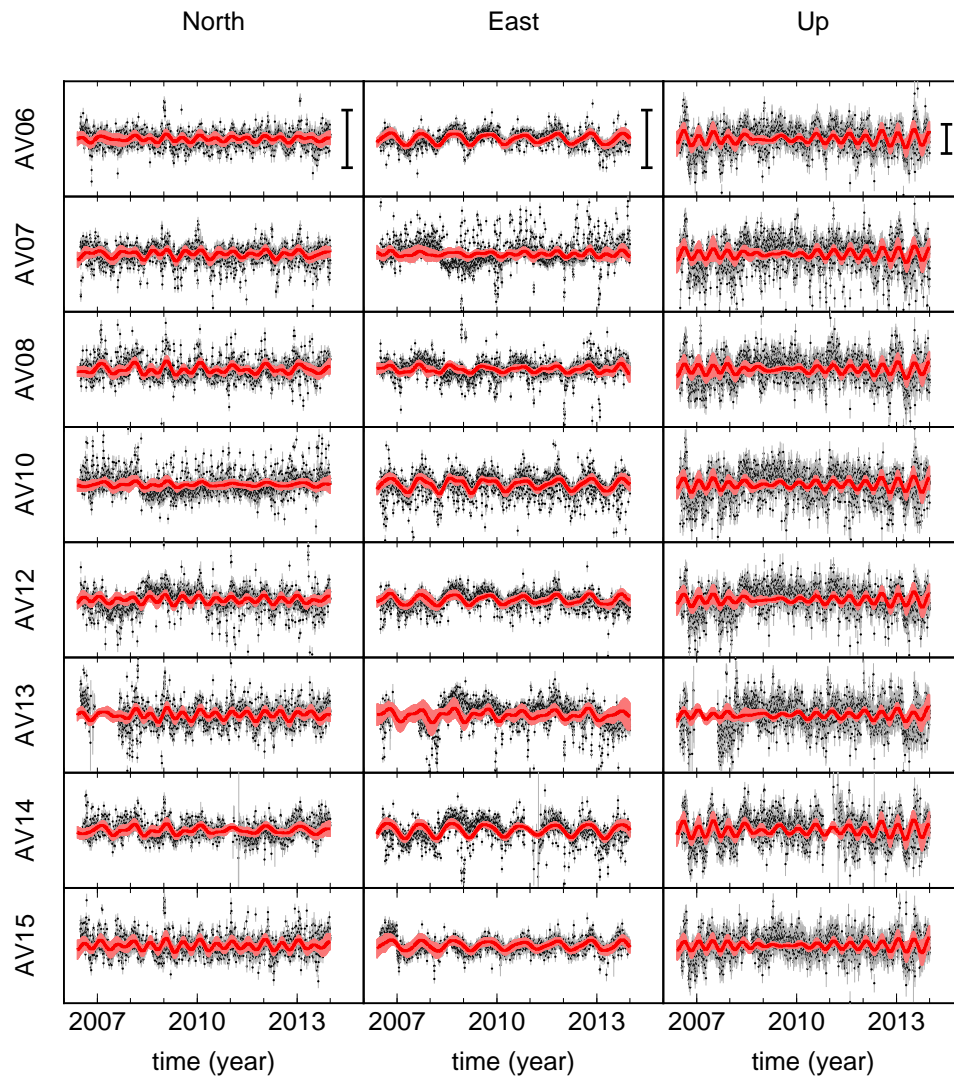


Figure 2.12: Seasonal variability of the GPS data set for Akutan. Black dots: detrended daily GPS position time series at 8 sites on Akutan volcano, Alaska, with their $1\text{-}\sigma$ error bars. Red lines: reconstructed series after M-SSA using the combination of ST-PCs 2–3 (annual) and 6–7 plus 9–11 (semi-annual). The black vertical lines in the topmost panels represent 10 millimeters. The subpanels correspond to the 8 cGPS sites and 3 directions of motion as in Figure 2.10. Note the good visual fit to the data. The pluri-annual modulation of the seasonal signal is clearly visible, for instance, in the lower-amplitude vertical signal for 2009, which appears across all the stations. The light red areas represent the variability of the reconstructions of the seasonal oscillations when the raw time series are perturbed by colored noise with spectral index of 1.

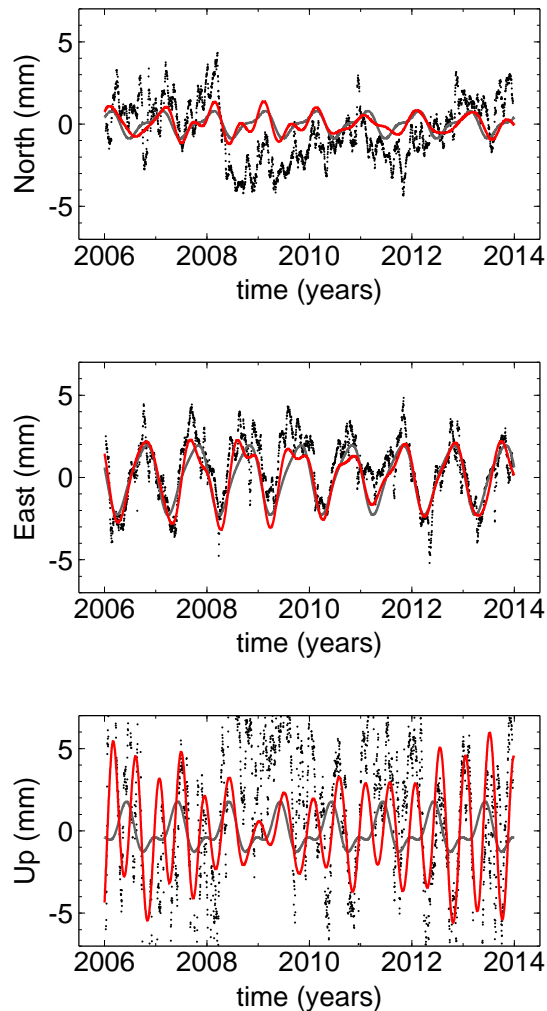


Figure 2.13: Comparison between the reconstruction of the seasonal signal obtained with M-SSA (red solid curve) and a commonly used fit of the sum (black solid curve) of an annual and a semi-annual harmonic function for each component recorded at site AV10: (A) northward, (B) eastward, and (C) upward. We applied a 20-day moving average to the raw data (black dots) to reduce the data scatter and be able to better distinguish the difference between the M-SSA reconstructions and the four-term Fourier series. The two models are, to first order, very close, but M-SSA reconstructions show a pluri-annual modulation in amplitude that is not present in the constant-amplitude harmonic functions. Note also that these harmonic functions significantly underestimate the observed range of values in the vertical component. The weighted root mean square (WRMS) are 3.29mm , 2.99mm and 8.44mm for the M-SSA reconstructions of the seasonal signal for the North, East and Up components respectively. The harmonic functions fit have a WRMS of 3.32mm , 3.05mm and 9.14mm which is systematically higher.

2.8. FIGURES

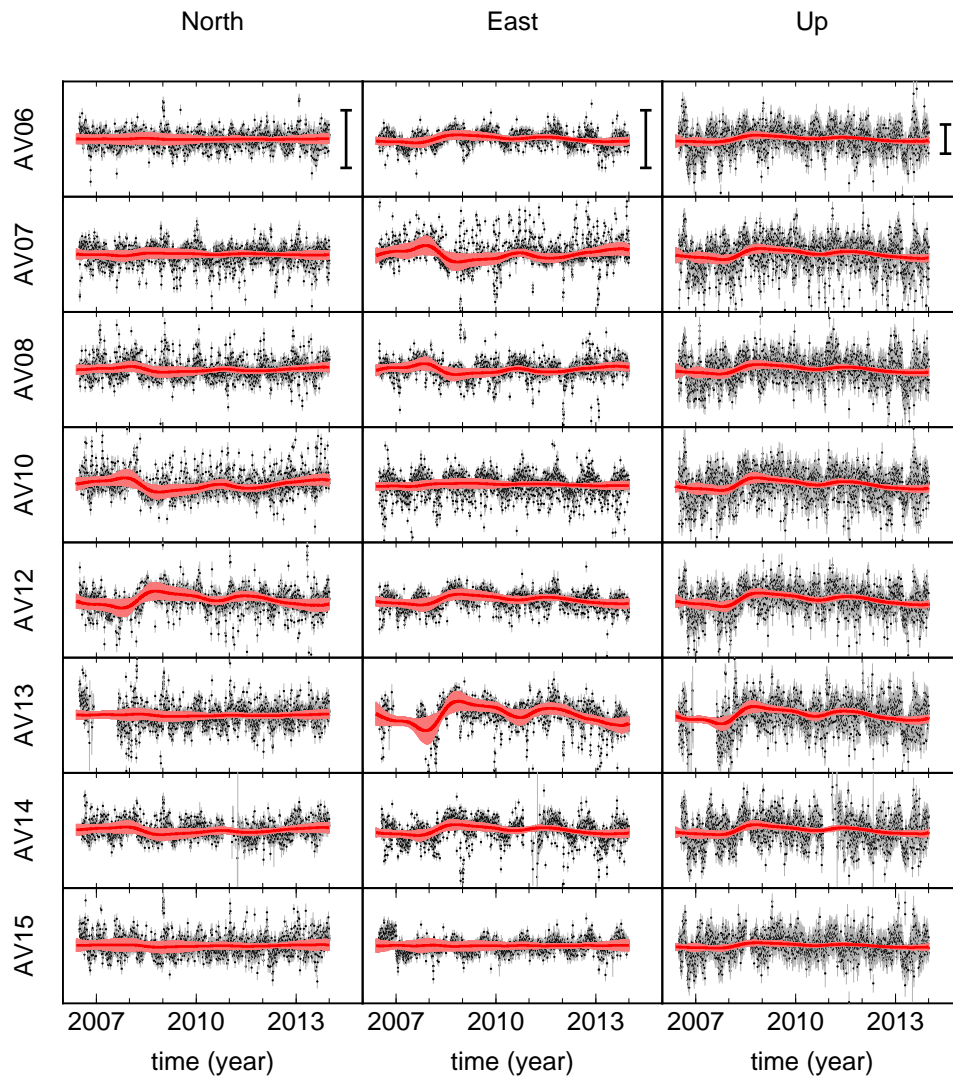


Figure 2.14: Transient motion at Akutan volcano, Alaska. The subpanels correspond to the 8 cGPS sites and 3 directions of motion as in Figure 2.10. Note the good visual fit to the data. Black dots: detrended daily GPS position time series at the 8 cGPS sites; with their $1\text{-}\sigma$ error bars. Red lines: M-SSA reconstructions, using the trend ST-PCs 1 and 4, which together carry 11% of the total data variance. The black vertical lines in the topmost panels represent 10 millimeters. The light red areas represent the variability of the reconstruction of the data-adaptive trends when the raw time series are perturbed by colored noise with spectral index of 1.

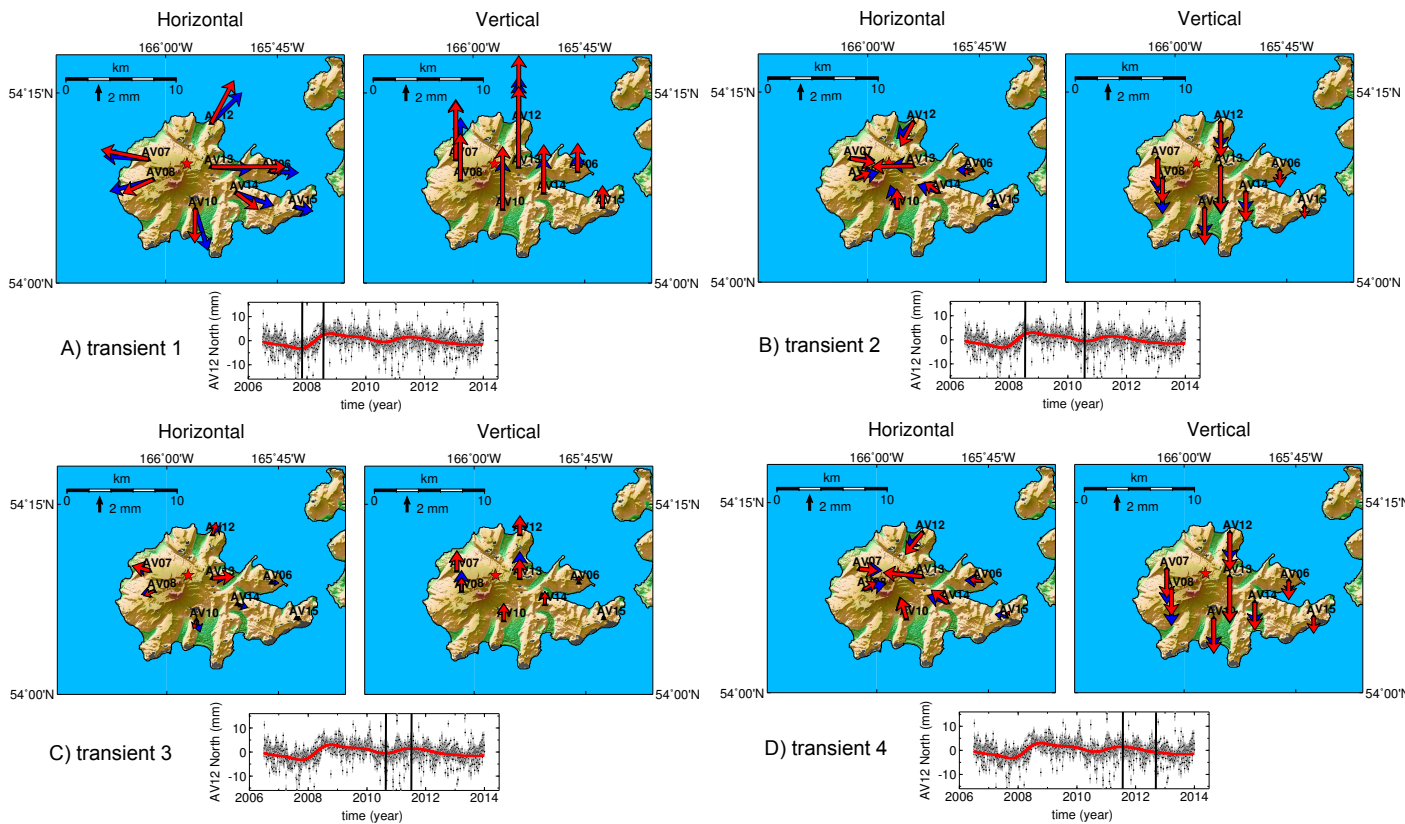


Figure 2.15: Maps of the horizontal and vertical displacements at Akutan volcano that are associated with the four dominantly monotonic parts of the reconstructed trends derived from ST-PCs 1 and 4. For each event, the two upper panels plot the vector displacements at the 8 cGPS sites, while the lower panel plots the time series of northward displacements at site AV12. In this latter panel, black dots show the raw data and the red solid curves show the M-SSA-reconstructed trend signals, while the blue solid curves show the best-fit prediction from a simple, idealized model of magma chamber expansion (Mogi, 1958). In the upper panels, the red arrows are based on the M-SSA reconstructions and the blue ones are based on the Mogi (1958) model. Note the spatial consistency of the displacements for each of the four successive episodes with a radial pattern centered on the volcano that is consistent with a magmatic origin.

2.8. FIGURES

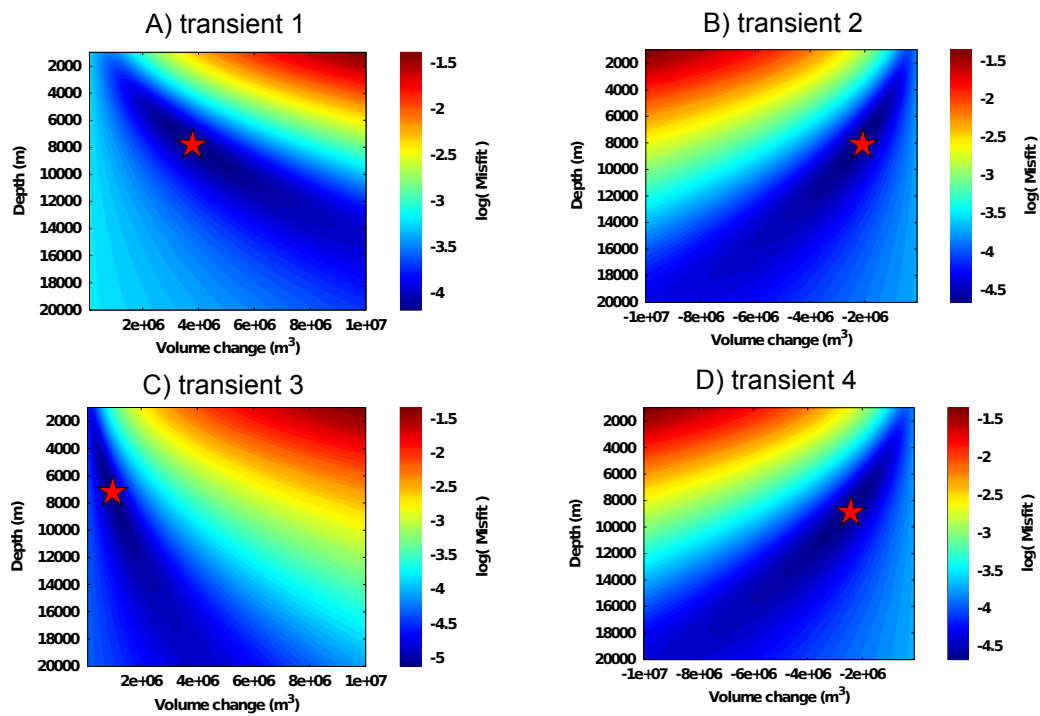


Figure 2.16: Misfit plots between the deformation predicted by a Mogi source and the observed displacements for each of the four transient events shown in Figure 2.15. The four events are well explained by inflation (uplift and radial extension at the surface) or deflation (subsidence and radial contraction at the surface) of the same point source at 8 ± 1 km. These results strongly support the hypothesis that the small but coherent deformations extracted by M-SSA are of magmatic origin.

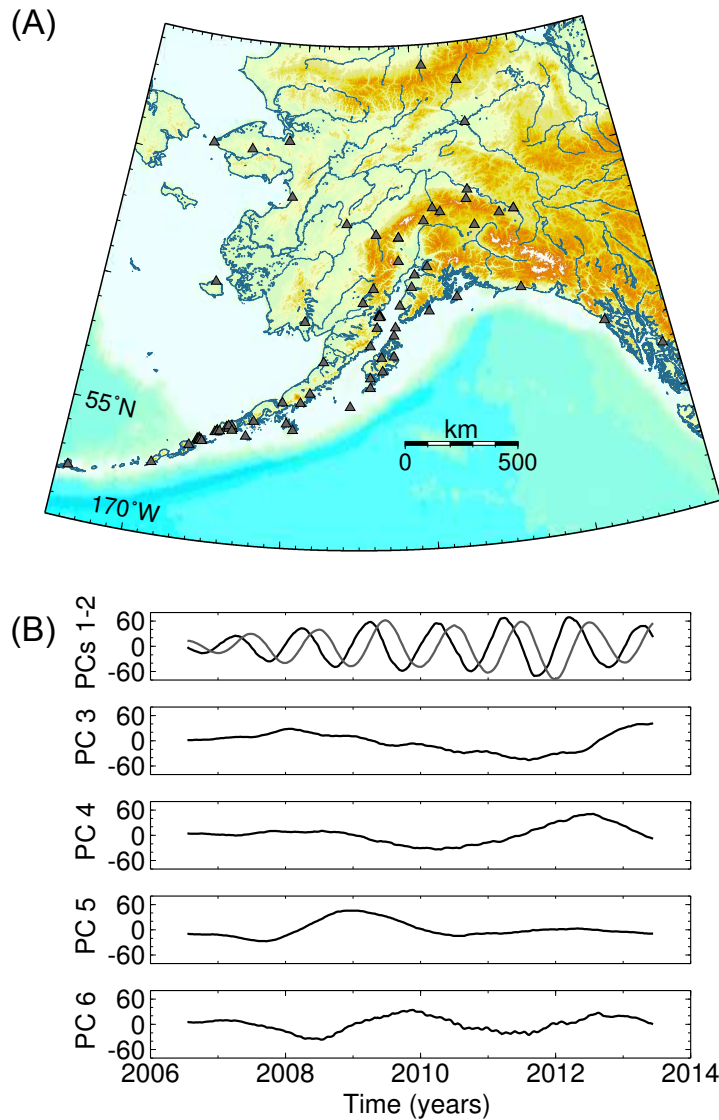


Figure 2.17: M-SSA analysis of the PBO network of 80 GPS stations from Alaska: (A) geographic distribution of the stations; and (B) the six leading ST-PCs calculated by applying M-SSA to the position time series from this network. ST-PCs 1,2 are in phase quadrature and represent a seasonal oscillation with an annual period. The next 4 ST-PCs represent data-adaptive trends.

2.8. FIGURES

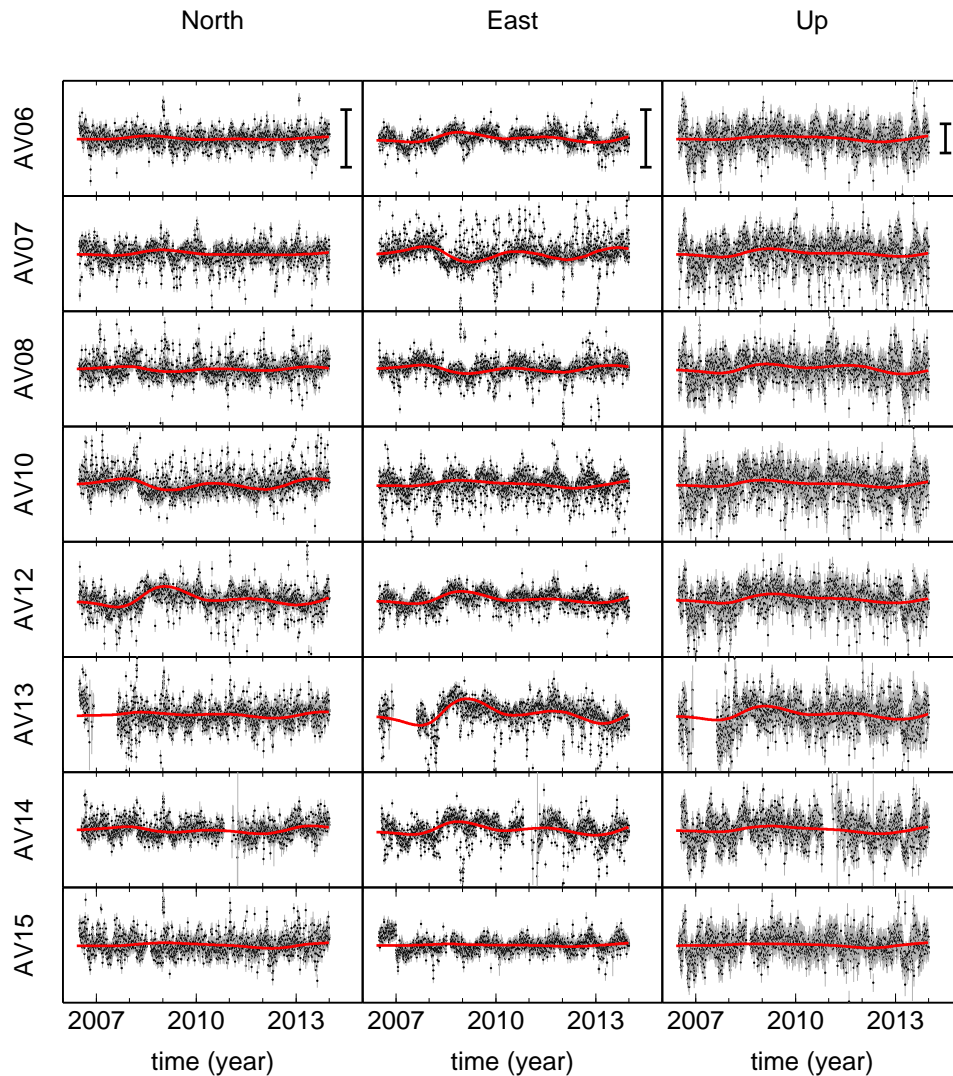


Figure 2.18: Reconstructed time series (solid red lines) using ST-PCs 3–6 of Figure 2.17B, which represent data-adaptive trends. The black vertical lines in the topmost panels represent 10 millimeters. The reconstructions here are for the same 8 cGPS sites on Akutan volcano as plotted in Figure 2.14, and are presented in the same format. Here, however, the reconstructions are calculated from the 80×3 time series from the PBO network covering Alaska and shown in Figure 2.17A. Note the similarity with the reconstructed series derived solely from the 8×3 Akutan GPS time series, plotted in Figure 2.14. For 15 ($\sim 60\%$) of them the correlation coefficients between the reconstructed time series from 8 stations and 80 stations are larger than 0.7. For 7 of them ($\sim 30\%$) the correlation coefficients are less than 0.5. However, these 7 time series are those for which the signal is very weak such as in the three components recorded at AV15.

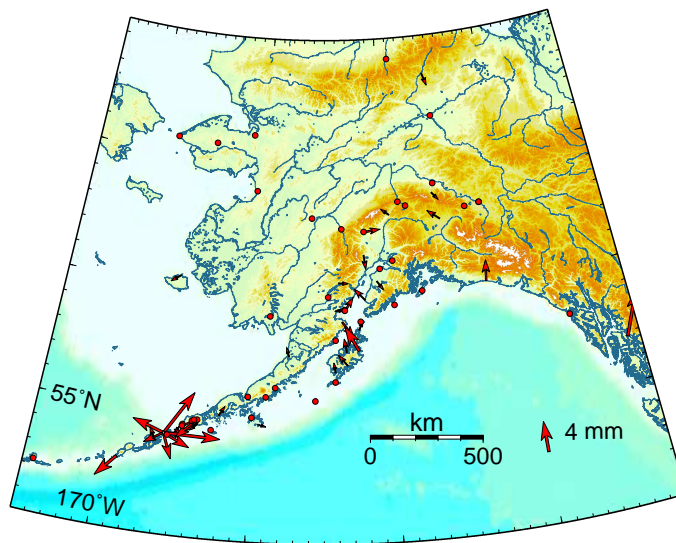


Figure 2.19: Map of the horizontal displacements associated with the first transient deformation event identified above for the Alaskan PBO network; this event corresponds to the time interval 2008.0–2008.7, cf. Figure 2.18. The red arrow over the Gulf of Alaska indicates a horizontal displacement of more than 1 mm. To make them visible we indicate GPS sites with displacements less than 1 mm with red dots indicate. Note that displacements at Akutan stand out as anomalously large, with a radial pattern. Figure 2.20 below shows a close-up on Akutan.

2.8. FIGURES

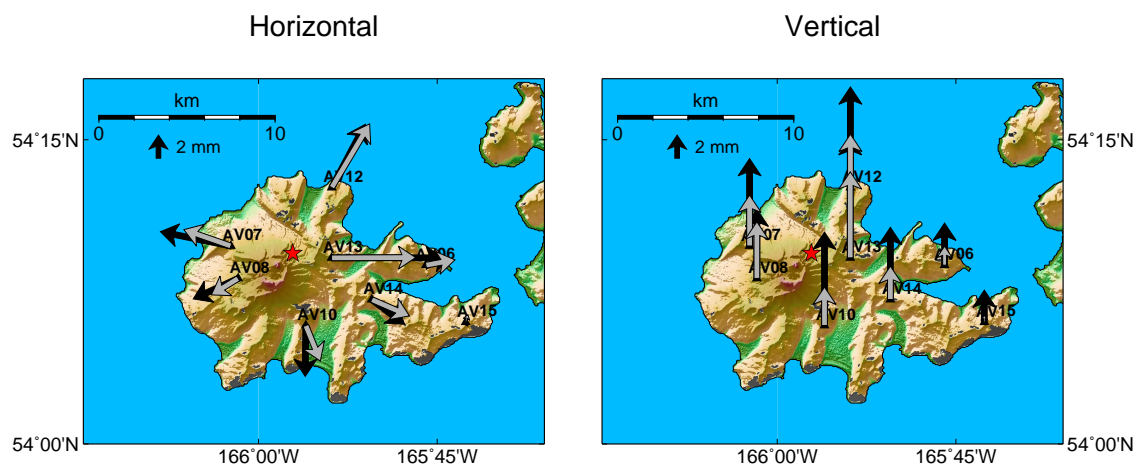


Figure 2.20: Comparison of the horizontal and vertical displacements associated with the first transient-deformation event identified above (2008.0 to 2008.7), as extracted from the 8-site M-SSA (black arrows vs. the 80-site, Alaska-wide M-SSA (white arrows). Note the agreement between the local and the regional-scale M-SSA estimates: both show a radial pattern of extension and uplift centered on the volcano. This pattern is consistent with a magmatic origin, as seen in Figure 2.15 above.

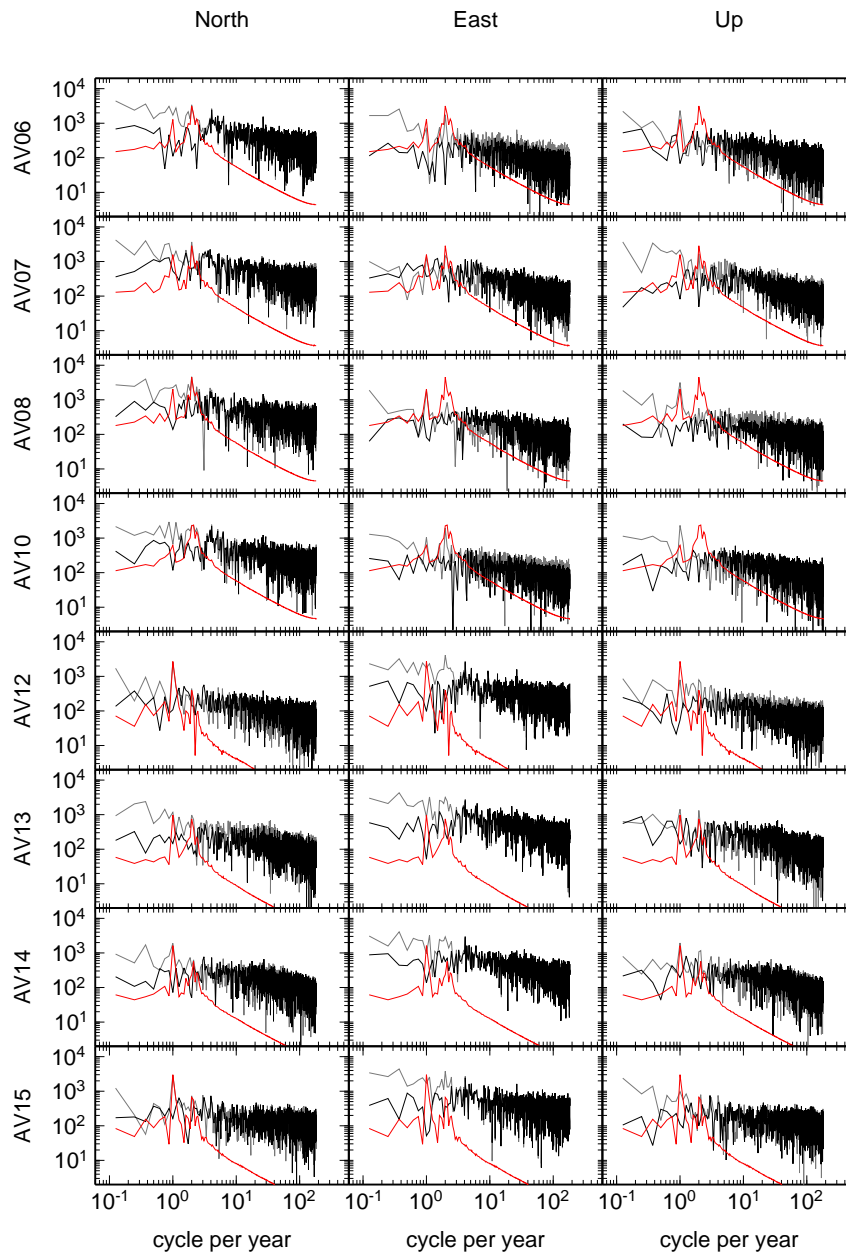


Figure 2.21: Power Spectral density plots of the raw time series (grey lines) and M-SSA-based seasonal signal (red); the residual component, i.e. raw minus the M-SSA reconstruction of the transient displacements plus the seasonal signals is plotted as black lines. Note the flattening of the spectrum of the residuals at low frequency, indicating that the trend and the oscillatory components are extracted by M-SSA, while preserving the high-frequency noise content.

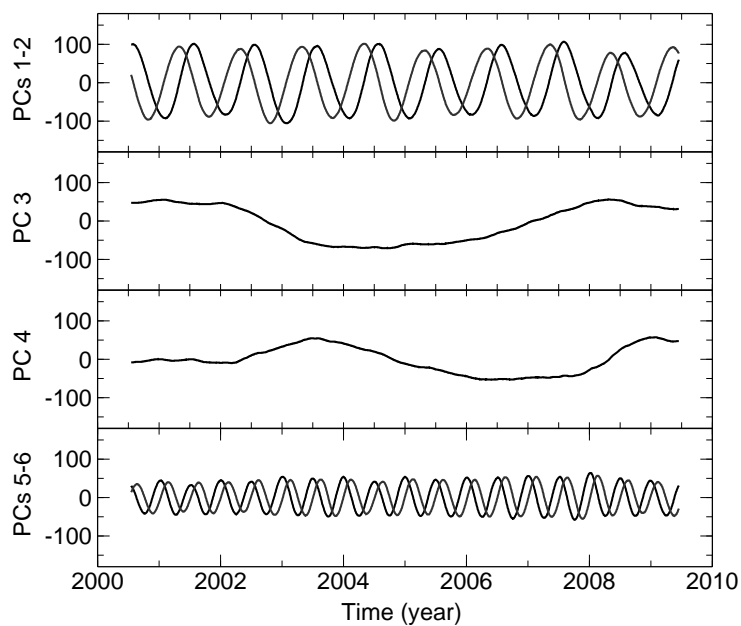


Figure 2.22: The four leading ST-PCs obtained from the M-SSA on the synthetic time series of the SCEC transient detection exercise. ST-PC pair 1-2 capture the annual oscillations. ST-PC pair 5-6 capture the semi-annual oscillations. Together these two ST-PCs pairs that represent the seasonal oscillations carry $\sim 50\%$ of the variance. ST-PCs 3 and 4 capture the data-adaptive trend and describe $\sim 15\%$ of the total variance of the data set.

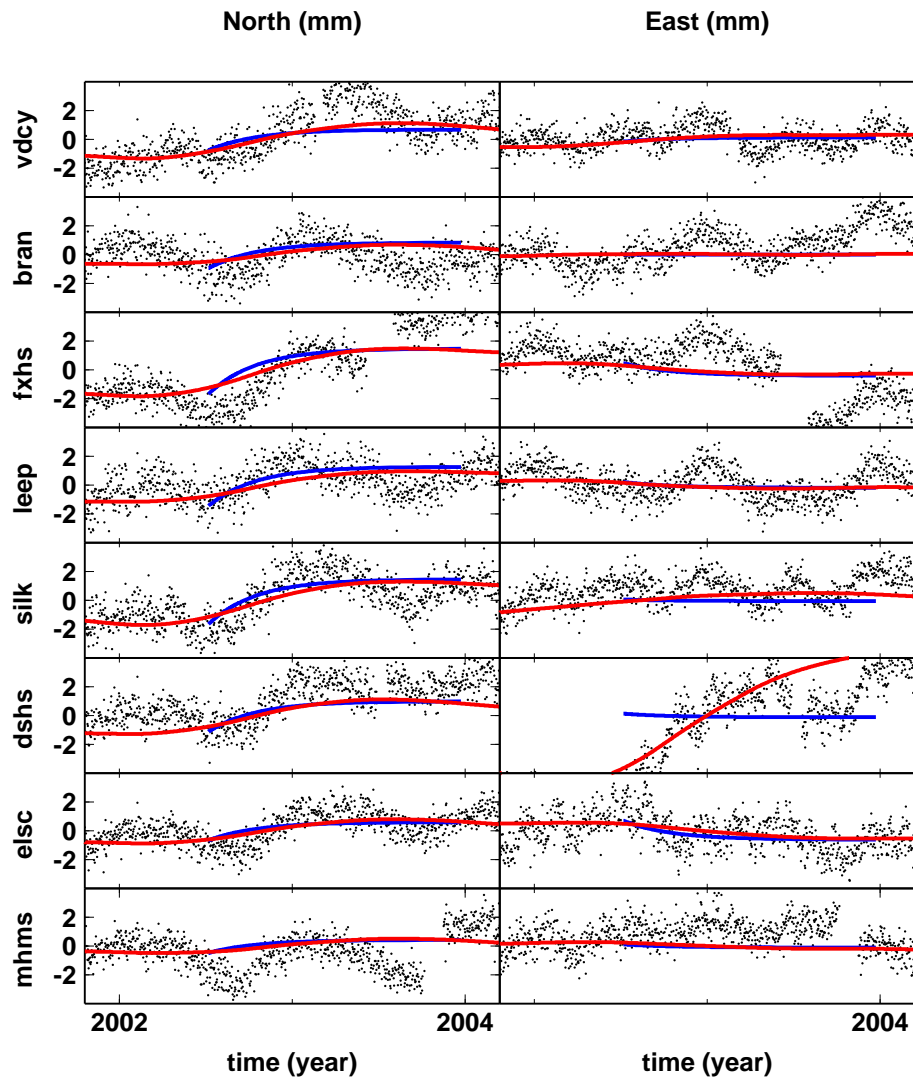


Figure 2.23: Reconstructed Transient motion at some GPS sites near the Santa-Monica fault. The subpanels correspond to 8 selected cGPS sites and the horizontal directions of motion. Black dots: detrended daily GPS position time series at the 8 cGPS sites. Red lines: M-SSA reconstructions using the trend ST-PCs 3 and 4 which together carry 15% of the total data variance. Blue lines: synthetic transient displacement generated by a simulated thrust event on the Santa Monica fault. The M-SSA filtered time series are consistent with the transient displacements except in the east component recorded at site "dshs" which contains large-amplitude colored noise.

2.8. FIGURES

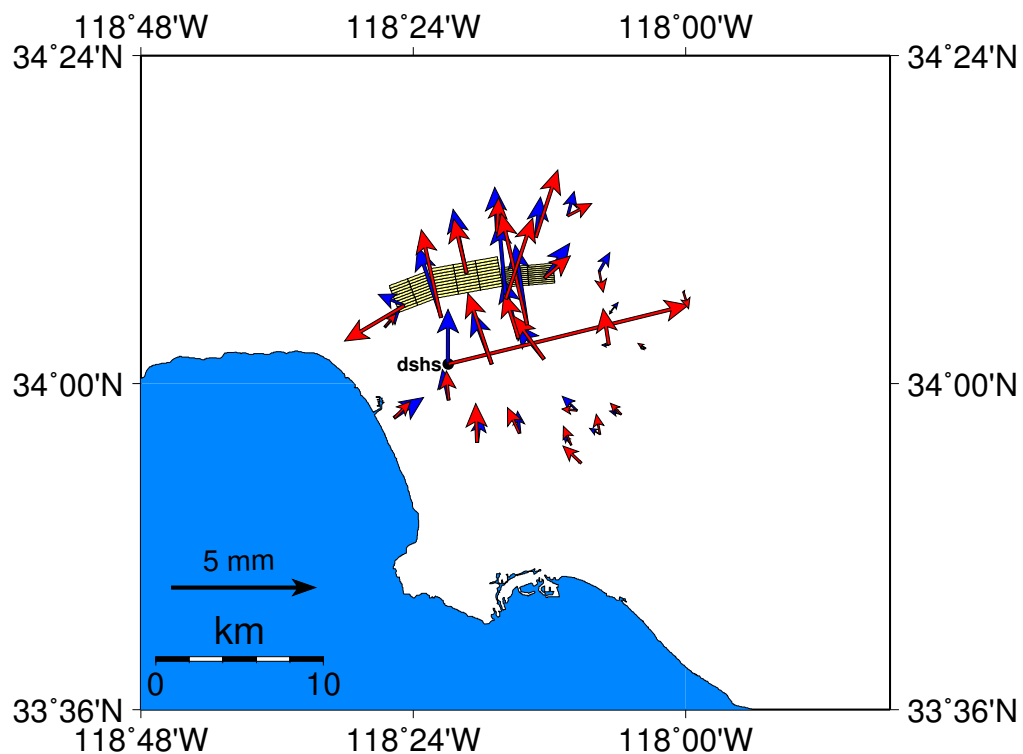


Figure 2.24: Maps of the horizontal displacement at some cGPS sites near the Santa-Monica fault. Red arrows: transient horizontal displacements derived from the M-SSA reconstructions of the data-adaptive trends of the time series. Blue arrows: simulated horizontal displacements associated to a thrust event on the Santa Monica fault. The segment of the Santa Monica fault on which the slip occurred is represented by the rectangular patches. The M-SSA reconstructions are consistent with the simulated thrust event. The large discrepancy at site DSHS is caused by colored noise of large amplitude on the east component (see Figure 2).

CHAPTER 3

NONLINEAR DYNAMICS OF VOLCANIC INFLATION/DEFLATION CYCLES

3.1 Abstract

Ground motion from space geodetic techniques — such as the Global Positioning System (GPS) and radar interferometry (InSAR) — is typically used in areas of volcanic unrest to constrain static or kinematic models that relate change of pressure in a chamber with surface deformation. The rapidly increasing amount of geodetic data opens up the additional possibility to mine for information on the qualitative dynamics of volcanic systems directly from the continuous deformation data, without using any prior assumptions on the underlying processes. Here we study four volcanoes that have been continuously monitored by GPS and identify common sawtooth-shaped inflation–deflation cycles. Application of data-adaptive, nonparametric time series analysis methods permits the reliable detection of such oscillations when they lie close to, or even below, the data scatter. We show that these cycles bear similarities with the relaxation oscillations of a simple oscillator that involves a nonlinear dissipative mechanism.

3.2 Introduction

The numerous – and rapidly increasing – continuous space geodetic observations now available from InSAR and GPS in areas of active volcanic unrest show nonlinear surface deformations that reflect the dynamics of the underlying magmatic processes. These processes include magma flux within the volcanic plumbing system (Dvorak and Okamura, 1987; Mériaux and Jaupart, 1995; Parks et al., 2012), crystallization and degassing in melt reservoirs (Biggs et al., 2009; Larsen et al., 2013; Caricchi et al., 2014) and hydrothermal circulation driven by the magmatic thermal anomaly (Hutchison et al., 2015, 2016). The resulting surface deformation is sometimes readily visible from the data time series (Newman et al., 2006; Feng and Newman, 2009), but it is often hidden in the measurement noise. Recent advances in time series analysis have shown, however, that nonlinear deformation caused by magmatic processes can be present during seemingly quiet time intervals in which little to no deformation is apparent in the data (Ji and Herring, 2011; Walwer et al., 2016).

Although the temporarily varying observations can be explain by an *ad hoc* time dependent forcing process — be it magma flux, degassing, heat flux — our goal here is different. We seek instead to extract temporal variability patterns from continuous deformation measurements and determine their level of similarity in order to find common types of behavior that contain qualitative information on the underlying dynamics. To do so, we objectively extract repeating transient deformation signals at four volcanoes using continuous GPS time series. We illustrate the resemblance of their deformation patterns using phase portrait reconstructions, which suggest dynamical similarity between them (Guckenheimer and Holmes, 1983; Ghil and Childress, 1987; Jordan and Smith, 2007). We show that a simple nonlinear oscillator shares the qualitative behavior of the inflation–deflation cycles observed at these volcanoes.

3.3 Methods

3.3.1 Data and preprocessing

We used position time series provided by the Plate Boundary Observatory (*pbo.unavco.org*) and the Nevada Geodetic Laboratory (*geodesy.unr.edu*). They are derived from continuous GPS data at stations located on four volcanoes: Akutan (8 stations), Shishaldin (8 stations), Okmok (5 stations), and Piton de la Fournaise (5 stations); see Figure 3.1. Because we are interested in the dynamics of the volcanic systems, we first removed from each time series a linear trend that represents the sum of tectonic plate motion and long-term elastic loading on neighboring faults, and focus the analysis on the nonlinear deformation signals.

In order to isolate the displacements associated with the activity of the volcanic systems from other geophysical signals, such as seasonal oscillations of hydrological origin, and from the GPS measurement noise, we filtered the detrended position time series using Multichannel Singular Spectrum Analysis (M-SSA). M-SSA is a data-adaptive, nonparametric method that simultaneously exploits the spatial and temporal correlations in geophysical fields in order to extract their common modes of variability (Walwer et al., 2016; Ghil et al., 2002; Alessio, 2016); see the Supplementary Materials for details. This distinguishes M-SSA from filters that rely on prior hypotheses and search for signals using a library of functions whose shape is determined from a priori models (Alessio, 2016; Ohtani et al., 2010; Riel et al., 2014a).

3.3.2 Volcanic signal reconstructions

M-SSA decomposes a set of L time series into common modes of spatio-temporal variability that correspond to nonlinear trends, oscillations, or noise. These modes are the eigenvectors of the covariance matrix computed from the ensemble of M lagged copies of the L time series composing the dataset we wish to analyse. The eigenvectors are ordered according to the amount of data variance each of them account for which is given by the associated eigenvalues. The maximum period of the modes that are extracted with M-SSA is $\sim M\tau_s$ where τ_s is the sampling interval of the time series. For the four dataset analyzed $\tau_s = 1 \text{ day}$.

Signals that are common to all time series are accounted by the modes describing the largest part of the total variance. In the context of this study, we expect therefore that signals of volcanic origin will be accounted by modes describing a significant part of the total variance of the dataset.

Two others criteria are exploited to select the modes used to reconstruct the volcanic signals. First we are looking for temporal patterns that is similar for the four volcanoes under study and consist in inflations followed by slower and longer deflations. Second, the reconstructed signals must have the shape of radial deformation patterns in map view that are consistent with magmatic inflation or deflation.

A key point of the approach that is presented here is that the number of modes used to reconstruct the signals, S , is an output of our analysis. For Akutan, we find that the first and the second modes capture the nonlinear trend associated with the volcanic signal. We computed therefore the volcanic signal time series using these two modes meaning that $S = 2$. This result is consistent with a similar analysis done already for Akutan volcano (Walwer et al., 2016). For Shishaldin, we need to use only the second mode ($S = 1$), while for Okmok and the Piton de la Fournaise, we used respectively first two modes ($S = 3$) and the first three modes ($S = 4$). Table 3.7 gives a summary of the M-SSA analysis for each volcano (see also the supplementary materials for further details about the methodology.)

3.4 Deformation trends at four volcanoes

Time series at selected GPS sites (raw data as black dots) and the M-SSA-based reconstruction (red lines) are displayed in Figure 3.2. The corresponding horizontal displacements for a selected time interval, displayed in map view as arrows in the appropriate panel of the same figure, are radial and centrifugal, and they are accompanied by vertical uplift (Supplementary Figures S1–S4). Such a pattern is typical of an inflation episode caused, for instance, by the pressurization of a magma reservoir at depth, as already shown for Akutan (Ji and Herring, 2011). Map views of sites displacements for other time intervals with monotonic position variations show similar radial patterns, alternating inflation and deflation episodes (Supplementary Figures S1–S4).

3.5. SIMILARITIES IN BEHAVIOR

Inflation–deflation episodes are readily visible in some position time series with no need for pre-filtering, as seen at Okmok or Piton de la Fournaise, (Figure 3.2), others are close to — or even below — the data scatter, such as Akutan in 2011 (see Supplementary Figure S1). These episodes, too, can be extracted effectively and reliably by M-SSA because they induce spatial and temporal correlations in the ensemble of time series analyzed (Walwer et al., 2016) (see Supplementary Information). As a result, time intervals that would otherwise appear as devoid of deformation now show repeating inflation–deflation episodes that resemble their larger-amplitude counterparts.

The combined information in Figure 3.2 (see also Supplementary Figures S1–S4) shows that all the reconstructed time series — for the three components, north–south, east–west, and vertical — on each volcano exhibits a behavior similar to that in Figure 3.2 for Akutan. In all cases, the first inflation episode is followed by a slower and longer deflation, marked by subsidence and radial contraction of the volcanoes.

At Akutan and Okmok this pattern repeats with an amplitude that decreases with time, reminiscent of damped oscillations. At Akutan the last deflation is followed by an inflation that ends in 2016. At Shishaldin, the deflation phase is also followed by an inflation that ends around 2015. At Okmok and Piton de la Fournaise, a rapid inflation occurs again after the last deflation episode, directly followed by a rapid and large deflation associated with an eruption.

The characteristic time and displacement scales of the four systems are different. At Akutan and Okmok the oscillations last roughly 2 years, with a maximum horizontal displacement at Akutan that is much smaller, of barely 1 cm, than at Okmok, where it is of up to about 60 cm. Shishaldin has the longest deformation cycle, of about 4 years, with a maximum horizontal amplitude less than 1 cm. Piton de la Fournaise has the shortest deformation cycle, of about 0.5 year, with a maximum displacement larger than 10 cm.

3.5 Similarities in behavior

To learn more about the dynamics reflected by the filtered time series, let us consider here the four volcanoes as nonlinear oscillators. Such a simple analogy does not capture the

detailed physics of the natural processes at play, but it will allow us to identify some of the features that lead to the qualitative behavior observed in the data. To identify the proper design features for our oscillators, we compute phase portraits for the four volcanoes by differentiating the reconstructed time series with respect to time and embedding them in the plane of displacement versus rate-of-displacement (Packard et al., 1980; Roux et al., 1980; Takens, 1981b).

Phase portraits show the evolution of dynamical systems as trajectories that depict, as time increases, geometrical structures characterizing their dynamics. In this phase space, stationary solutions appear as points and periodic ones as closed trajectories. These representations highlight in particular how an out-of-equilibrium system is organized around stationary solutions (Ghil and Childress, 1987; Deremble et al., 2009). Since the position time series in all the components of deformation show the same pattern, we use the least noisy ones for each volcano to compute the phase portraits shown in Figure 3.3. Also, since our goal is to extract qualitative features of the system dynamics, we normalized both the displacements and the displacement rates to their maximum absolute values.

A first-order feature common to the four phase portraits is the spiraling in and out of their trajectories. This geometry is reminiscent of nonlinear dynamical systems that are in an oscillatory regime with modulated amplitude around an equilibrium point (Guckenheimer and Holmes, 1983; Jordan and Smith, 2007). Note that the two damped oscillation cycles described above at Akutan and Okmok, based on their filtered time series in Figure 3.2, are quite obvious in their phase portraits here. Also common to the four phase portraits is the fact that the trajectories are highly asymmetric about the horizontal line of null displacement rate, since they only reach the $+1$ value above this line, but not the -1 value below it. This asymmetry reflects inflation rates that are larger than the deflation rates.

Another feature shared by the four phase portraits is that each deflation phase shows variations in the deflation rate, which alternates between increases and decreases. This feature is associated with small ripples in the orbits as they evolve through negative values of the displacement rate in the phase plane. In other words, the deflation episodes

3.6. A SIMPLE NONLINEAR OSCILLATOR

systematically slow down before accelerating again at the end. At Okmok and Piton de la Fournaise, where the inflation and deflation displacements are large — measuring tens of centimeters — this feature is visually clear upon careful examination of the time series itself. At Akutan and Shilshaldin, where displacements measure a mere few millimeters, visual examination is no longer sufficient for detecting this rippling in deflation episodes. But the subtle variations in the deflation rates are still detected by the M-SSA filter.

3.6 A simple nonlinear oscillator

The phase portraits in Figure 3.3 and their discussion above suggest that further insight into the nature of the observed oscillations will be provided by formulating and analyzing a simple, nonlinear oscillatory model. Such a model does, as we shall see herewith, reproduce key qualitative features of the phase portraits above.

Our model is governed by a set of two coupled ordinary differential equations:

$$\begin{cases} \dot{x} = y, \\ \dot{y} = -\mu[(x + x_0)^2 + (y + y_0)^2 - 1]y - x; \end{cases} \quad (3.1)$$

here x and its time derivative y are the two coupled variables of the system, while x_0 , y_0 , and μ are independent parameters. The nonlinearity in Eq. (3.2) results from the form of the damping coefficient $\kappa = \kappa(x_0, y_0, \mu) \equiv -\mu[(x + x_0)^2 + (y + y_0)^2 - 1]$. Our model is similar to the classic Van der Pol oscillator (Van der Pol, 1926), except for the supplementary quadratic dependence on y in the damping term. Moreover, the parameters $x_0 \neq 0 \neq y_0$ added herein make the damping asymmetric with respect to both the displacements x and the rates y .

For $\kappa = \mu = 0$, all the solutions of Eq. (3.2) are circles centered on the origin $(x, y) = (0, 0)$, which is neutrally stable. For $\kappa < 0$, all the circles that are sufficiently close to the origin become spirals that end up in the origin, which is then said to be a stable fixed point. For $\kappa > 0$, the situation is a bit more complicated, and will be analyzed forthwith. The two situations, of $\kappa < 0$ and of $\kappa > 0$, are also referred to as positive and negative damping,

respectively.

For simplicity, let us assume at first that $x_0^2 + y_0^2 < 1$. In this case, the regime into which the system evolves is controlled by the value of μ . For $\mu < 0$ — and hence $\kappa < 0$ as long as $x^2 + y^2$ is small enough — this regime has exactly one fixed point, i.e. one steady-state solution, at the origin; this fixed point is linearly stable for the dissipative situation characterized by $\mu < 0$. Linear stability means that, for any initial state sufficiently close to the origin, the system will spontaneously evolve towards the latter. As long as the parameters (x_0, y_0) lie within the unit circle, the origin undergoes a loss of linear stability when μ , and hence κ , become positive.

Further details of this simple case appear in the Supplementary Materials, where we also analyze the more complicated cases in which the quadratic nonlinearity in the damping term becomes crucial. The upshot of this analysis is the phase portrait displayed in Figure 3.4.

The change in the dynamics of a nonlinear deterministic system from a unique stable fixed point to a stable closed orbit — like the one seen in Figure 3.4 — is called a Hopf bifurcation and the closed orbit is itself a limit cycle (Ghil and Childress, 1987; Guckenheimer and Holmes, 1983; Jordan and Smith, 2007). The particular type of nonlinear oscillations that involve sawtooth-type behavior, with rapid escape from a no-longer stable fixed point followed by slow relaxation back to it, are called relaxation oscillations (Ghil and Childress, 1987; Van der Pol, 1926; Grasman, 2011).

A first-order feature noticeable in Figure 3.4 that is common to the GPS observations at our four volcanoes and to the simple system governed by Eq. (3.2) is the presence of asymmetric oscillations, with inflations that are faster and shorter than the deflations. These episodes are marked in the two panels of Figure 3.4 by the letters M and m at the end of the inflation and deflation episodes, respectively. In our dynamical model, higher inflation rates are caused by the asymmetry of the damping with respect to $y = 0$. The closer y_0 is to -1 , the larger this asymmetry becomes.

A second-order feature common to the observations and to our simple model is the variation in the deflation rates. In the model, this is caused by the quadratic dependence

3.7. DISCUSSION AND CONCLUSIONS

of the damping term on x and it is emphasized by this term's asymmetry with respect to $x = 0$. The break in the slope of the time series for $x(t)$ during deflation is marked by the letter d in Figure 3.4.

3.7 Discussion and conclusions

An important aspect of our results is that the number of leading modes S retained for study at each of the four volcanoes in Figure 3.1 is small, $1 \leq S \leq 4$, but different among the four. Vautard and Ghil (1989) showed that, in general, the value of S used to reconstruct a given signal is not unique and depends on the data quality, as well as on M-SSA parameters such as M , τ_s and D . Thus, a simple experiment of theirs demonstrated that increasing M or the signal-to-noise ratio tends to increase S .

Because of the different characteristics of the data sets used here, M , D and the signal-to-noise ratio are different for each volcano; see Table 3.7. Still, a common feature of the four M-SSA analyses is that the signal reconstructions using the small resulting S all exhibit inflation–deflation cycles with certain common characteristics, cf. Figures 3.2 and 3.3. These characteristics were discussed and summarized in Sec. 3.5.

We also showed that a highly idealized dynamical analog as formulated in Eqs. (3.2) — is able to explain the qualitative dynamics reflected in the surface deformation data. This finding implies that the amount of information needed to describe the state of a volcanic system in terms of surface deformation may be fairly small.

Together, the smallness of the number S of leading modes needed to describe the deformation signal, with $1 \leq S \leq 4$, and that of our model's number of degrees of freedom, namely 2, suggest that the number of variables needed to specify the state of the volcanic system within the accuracy of the data is quite small (Farmer et al., 1983; Broomhead and King, 1986a; Vautard and Ghil, 1989). Two interpretations can be proposed to explain this. First, the observables themselves, i.e., the deformation data — provide only limited information on the mechanism leading to the observed signal. Second, although volcanic systems possess a priori a large number of degrees of freedom, the qualitative nature of the oscillatory phenomenon observed here requires only the interaction of a few variables

to generate the observed dynamics, which “lives” on the system’s center manifold (Carr, 2012). In any case, a reduced dynamical system provides a useful framework to model the observations presented here.

That the relaxation oscillations observed here can be explained with a simple nonlinear oscillator provides an interesting guideline for understanding and modeling volcanic inflation–deflation cycles. To wit, physical models capable of explaining such observations should possess a Hopf bifurcation from a fixed point to a limit cycle that gives rise to asymmetric, sawtooth-shaped oscillations.

Note also that equally simple nonlinear dynamical systems can reproduce the same phenomenon of relaxation oscillations. But the one we presented was quite straightforward in terms of helping explain this type of behavior to interested readers who might not be familiar with dynamical system theory in general, and with concepts like positive and negative damping, in particular. Our choice was mainly pedagogically motivated, given that the emphasis is on the connection between the M-SSA analysis and the modeling using dynamical system theory, rather than the physics that gives rise to the observations.

The present work could thus stimulate new research to establish such a physical model and determine to which extent a given volcano’s inflation–deflation cycles may lie — for a given set of parameter values — in a stable oscillatory regime or, to the contrary, be subject to an instability that, in turn, may lead to irregular behavior, as observed at Piton de la Fournaise and Okmok (Larsen et al., 2013; Rivet et al., 2014). Being able to distinguish between regimes with amplifying vs. damped spirals in the phase plane of Figure 3.3 also hints at the possibility of predicting a volcano’s eruptive potential on short-to-intermediate times, compared to the typical cyclicity.

3.8. APPENDIX A: RECONSTRUCTION OF THE VOLCANIC SIGNAL

| <i>Volcano</i> | $\vartheta_s(\text{day})$ | N | L | M | S | <i>Signal/noise ratio</i> |
|------------------------------|---------------------------|-------------|-----------|------------|----------|---------------------------|
| Akutan | 1 | 3900 | 24 | 400 | 2 | $\sim 10\%$ |
| Shishaldin | 1 | 3331 | 21 | 400 | 1 | $\sim 4\%$ |
| Okmok | 1 | 1951 | 12 | 150 | 3 | $\sim 30\%$ |
| Piton de la Fournaise | 1 | 449 | 12 | 60 | 4 | $\sim 65\%$ |

Table 3.1: Summary of the parameters and results of the M-SSA analysis. Here τ_s is the sampling time; N number of data points; D the number of channels, i.e. of stations \times (displacements = 3); M is the window length; and S the number of leading modes retained for further study.

3.8 Appendix A: Reconstruction of the volcanic signal

In this section, we provide details on how the leading modes were chosen in order to reconstruct the deformation signal for each volcano. The volcanic signals that we are looking for correspond to the aperiodic or long-periodic, nonlinear trend present in each deformation time series. We expect, therefore, that they account for a significant amount of the total variance of the dataset. The singular spectrum — i.e., the eigenvalues ranked in decreasing order — allows one to estimate the relative variance captured by each mode, and the leading RCs provide the appropriate visualization of the signal after filtering out the lower-variance noise (Ghil et al., 2002; Alessio, 2016, and references therein).

The final check on the number S of modes to retain at each volcano relies on the consistency of the spatial pattern of the reconstructed displacements. The spatial patterns that we retained all correspond to the radial patterns that are usually associated with episodes of inflation and deflation.

In the absence of this type of spatial information, there is always a part of arbitrary decision when choosing the modes to reconstruct a given signal. This part of educated guesswork can be minimized by applying one or more significance tests to specifically determine which modes are likely to be associated with colored noise, as opposed to the signal; see for instance, Groth and Ghil (2015a) and Walwer et al. (2016). Doing so was not found to be necessary here, since each reconstructed signal gives fairly consistent spatial patterns.

Akutan

Walwer et al. (2016) already applied M-SSA to the Akutan GPS time series and provided details on the choice of M-SSA parameters. We invite the interested reader to consult this reference for further details.

Figure S3.9 shows the first 30 eigenvalues given by applying M-SSA to the time series recorded at Akutan, as well as the first 8 PCs. We can clearly distinguish two groups of PCs: PCs 5–8 display oscillations with either an annual or a semi-annual period, while PCs 1–4 correspond to a long-periodic nonlinear trend. It follows that, to reconstruct the volcanic signal, we have to choose among the first four modes.

The best combination that allows one to reconstruct a spatially consistent signal corresponding to both inflation and deflation is the combination of PCs 1 and 3. Adding PCs 2 and 4 would not change much the reconstruction of the signal in time, nor its spatial pattern; hence we select only the minimum number of $S = 2$ modes. These two modes, PC1 and PC3, together account for $\simeq 10\%$ of the total variance. The spatial patterns of selected episodes of inflation and deflation, as well as an example of a reconstructed time series are displayed in Figure S3.5. This result is consistent with the more detailed analysis of Walwer et al. (2016).

Shishaldin

For Shishaldin, the first three PCs in Figure S3.10(b) capture the overall nonlinear trend that may be associated with volcanic deformations. By testing signal reconstruction using all the possible combinations of the first three modes, we found that the radial shape of the inflation and deflation episodes is better reconstructed when using only the second mode. Spatial patterns of selected episodes of inflation and deflation, and an example of a reconstructed time series are displayed in Figure S3.6.

The first and third modes may correspond to another type of signal or to colored noise. Investigating this additional component of the time series is, however, beyond the scope of the present study. The second mode accounts for $\simeq 3\%$ of the total variance of the dataset.

Okmok

The singular spectrum resulting from the M-SSA analysis of Okmok time series is displayed in Figure S3.11, along with the first four PCs. The singular spectrum shows that the two first eigenvalues stand clearly above the rest of the spectrum, meaning that the first two modes, which capture $\sim 30\%$ of the total variance, are very serious candidates for representing the volcanic signal. Hence, we used these first two modes to reconstruct the signal, and found indeed that the spatial patterns are characterized by the radial displacement consistent with inflation and deflation; see Figure S3.7.

Piton de la Fournaise

For Piton de la Fournaise, the singular spectrum in Figure S4.2(a) shows that the first three modes account for $\sim 65\%$ of the total variance. Afterwards there is a substantial drop in variance, by almost a full order of magnitude, implying that the remaining modes are quite likely to be associated with colored noise. We simply chose these first three modes to reconstruct the volcanic signal at Piton de la Fournaise, and found once more that spatial patterns are consistent with inflation and deflation; see Figure S4.2.

3.9 Appendix B : Linear Stability Analysis

Linear stability analysis allows one to study the effect of infinitesimal perturbations $\Xi(t)$ on a system at equilibrium. Our highly idealized model of relaxation oscillations — analogous, cf. Figs. 3 and 4 in the main text, to those found in our geodetic observations at four volcanoes — is governed by the following set of two coupled ordinary differential equations (ODEs):

$$\begin{cases} \dot{x} = y \equiv f(x, y), \\ \dot{y} = -\mu((x + x_0)^2 + (y + y_0)^2 - 1)y - x \equiv g(x, y). \end{cases} \quad (3.2)$$

The evolution of small perturbations $\Xi(t) = (\xi(t), \eta(t))$ about the fixed point $(x, y) =$

$(0,0)$ is governed by the following set of linear ODEs:

$$\begin{cases} \dot{\xi} = \left. \frac{\partial f}{\partial x} \right|_{(0,0)} \xi + \left. \frac{\partial f}{\partial y} \right|_{(0,0)} \eta, \\ \dot{\eta} = \left. \frac{\partial g}{\partial x} \right|_{(0,0)} \xi + \left. \frac{\partial g}{\partial y} \right|_{(0,0)} \eta, \end{cases} \quad (3.3)$$

which is simply the linearized version of system (3.2).

Expanding system (3.3) gives

$$\begin{cases} \dot{x} = y, \\ \dot{y} = -\mu(x_0^2 + y_0^2 - 1)y - x. \end{cases} \quad (3.4)$$

The evolution of ξ and η around the origin $(0,0)$ is controlled by the eigenvalues λ_{\pm} of the coefficient matrix of the linear system (3.4):

$$\begin{cases} \lambda_+ = \frac{-\mu(x_0^2 + y_0^2 - 1) + \sqrt{\mu^2(x_0^2 + y_0^2 - 1)^2 - 4}}{2}, \\ \lambda_- = \frac{-\mu(x_0^2 + y_0^2 - 1) - \sqrt{\mu^2(x_0^2 + y_0^2 - 1)^2 - 4}}{2}. \end{cases} \quad (3.5)$$

When the real parts $\Re(\lambda_{\pm})$ of both eigenvalues are negative, small perturbations decay and the origin is stable, while it is unstable if one of the eigenvalues has a positive real part.

In the simpler case in which $x_0^2 + y_0^2 < 1$, one has $\Re(\lambda_{\pm}) < 0$ as long as $\mu < 0$, and the origin is linearly stable. As μ crosses zero and becomes positive, the origin loses its stability, small perturbations can amplify, and one needs to consider nonlinear stability. In Figure 4 of the main text, the direction that corresponds to the eigenvalue λ_+ , along which trajectories are ejected from the origin, is indicated by the two-sided light arrow labeled \mathcal{T}^u .

3.10 Appendix C : Nonlinear stability and Hopf bifurcation

When $x_0^2 + y_0^2 < 1$, there always exists a neighborhood of the origin within which $(x + x_0)^2 + (y + y_0)^2 < 1$ as well, so that — as previously stated — the linear stability of the

3.11. FIGURES

origin is governed by the values of μ alone. When $x_0^2 + y_0^2 > 1$, however, there is — at least a small — neighborhood of the origin within which $(x + x_0)^2 + (y + y_0)^2 > 1$; hence, even when $\mu < 0$, the damping is negative in this neighborhood, and trajectories escape from it. Such is the situation illustrated in Figure 4 of the main text.

This negative damping causes the origin to become unstable, with the system's trajectories spiraling out, until they enter a region within which κ changes sign and thus limits further increase of the distance $x^2 + y^2$ away from the origin. As a result, the situation changes from an infinite number of circular trajectories, for $\mu = \kappa = 0$, to one in which a single closed trajectory exists, and this trajectory is typically not circular.

In fact, the limit cycle in Figure 4 is precisely of the relaxation-oscillation type: not only is its shape not circular, but the velocities along it are non-uniform. This non-uniformity is highlighted by the changes in the slope of the $x(t)$ curve in the lower panel, with the three types of velocity, high, intermediate and low, separated by the points marked as M , d and m in both panels.

3.11 Figures

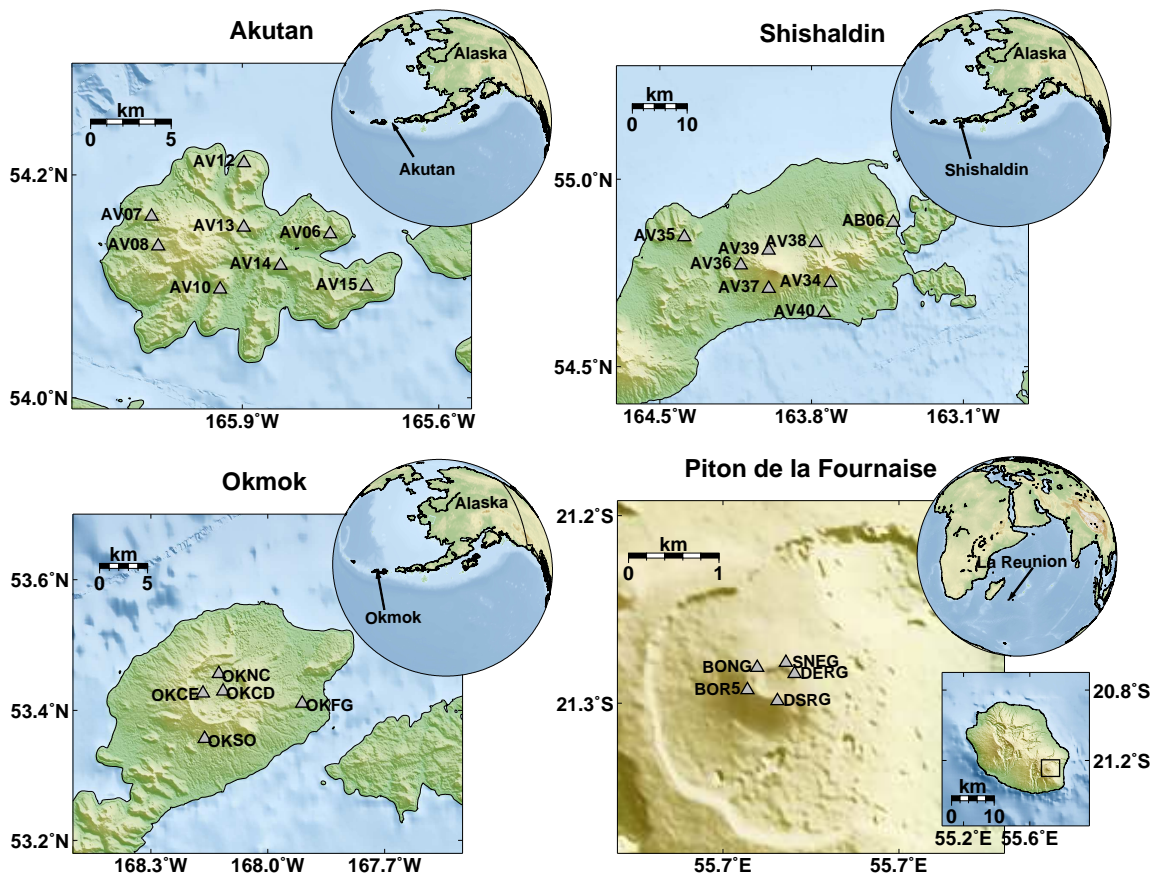


Figure 3.1: Location map of the four volcanoes used in this study, showing the GPS sciteps (grey triangles) from which the displacement time series used here have been extracted.

3.11. FIGURES

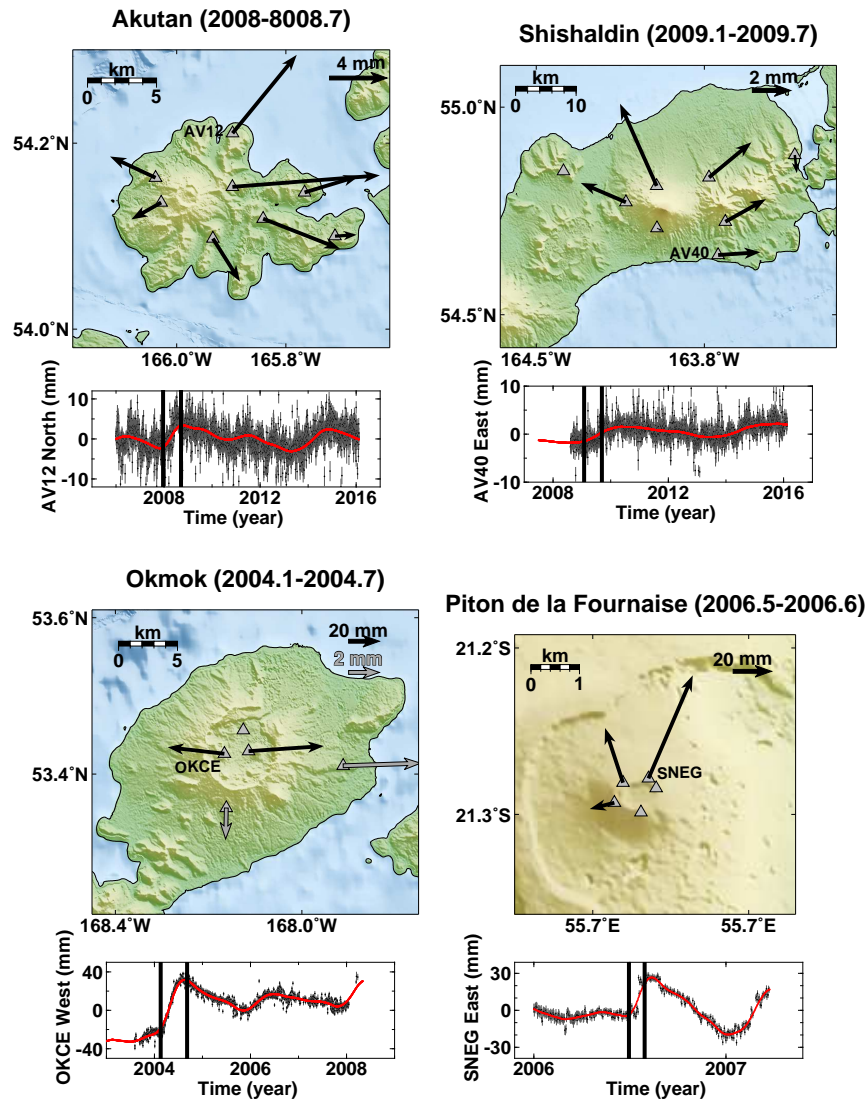


Figure 3.2: Spatial and temporal pattern of horizontal displacements at the four volcanoes. The top sub-panels for each volcano show the total horizontal displacements (black and grey arrows) during a selected episode of inflation; these episodes are indicated by the two vertical black lines on the time series in the sub-panels displayed below. Note the difference in scale between the grey and black arrows. The bottom sub-panels show a selected GPS time series: the black dots are the raw GPS time series, while the red line shows the corresponding M-SSA reconstruction. The corresponding GPS receivers are labeled on the maps.

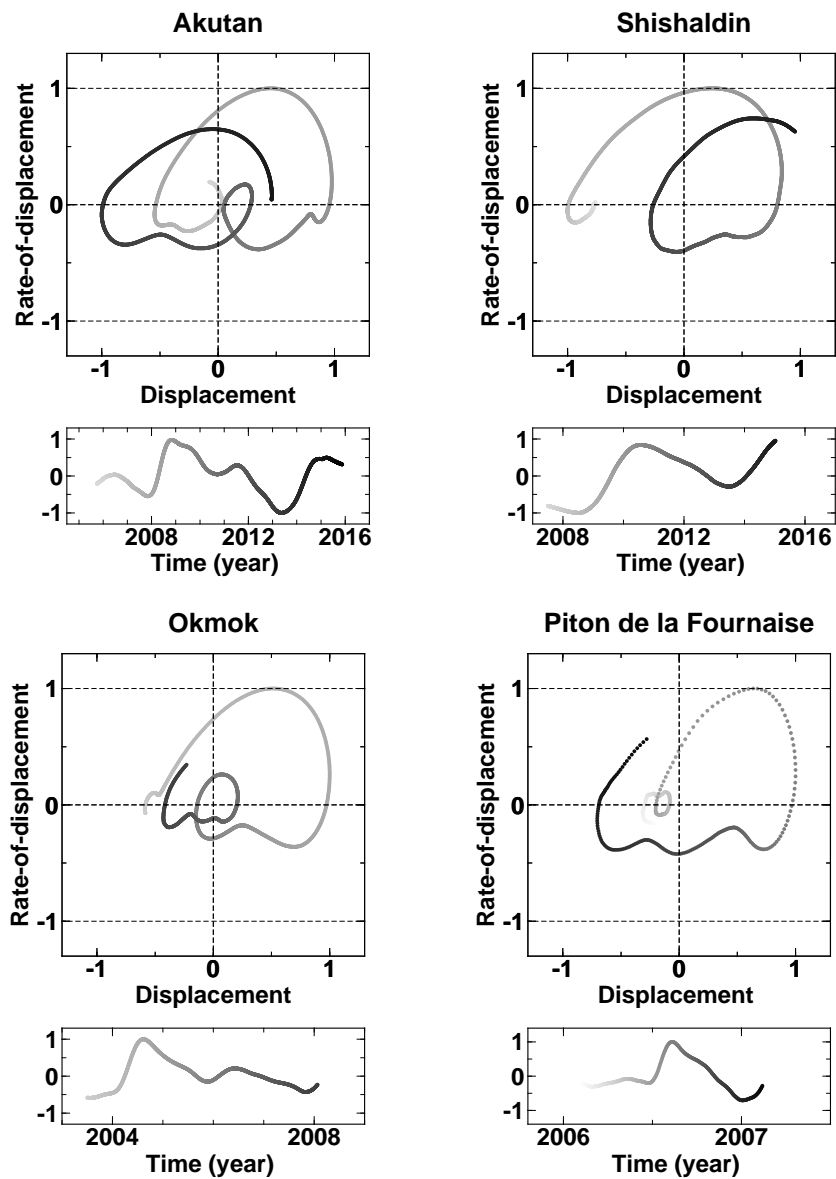


Figure 3.3: Phase portrait reconstructions in the displacement vs. rate-of-displacement plane and the corresponding displacement time series. The least noisy MSSA-reconstructed displacement component is plotted for each volcano, normalized so that all four lie between ± 1 . The grey scale, from white to black, indicates the evolving time, in years.

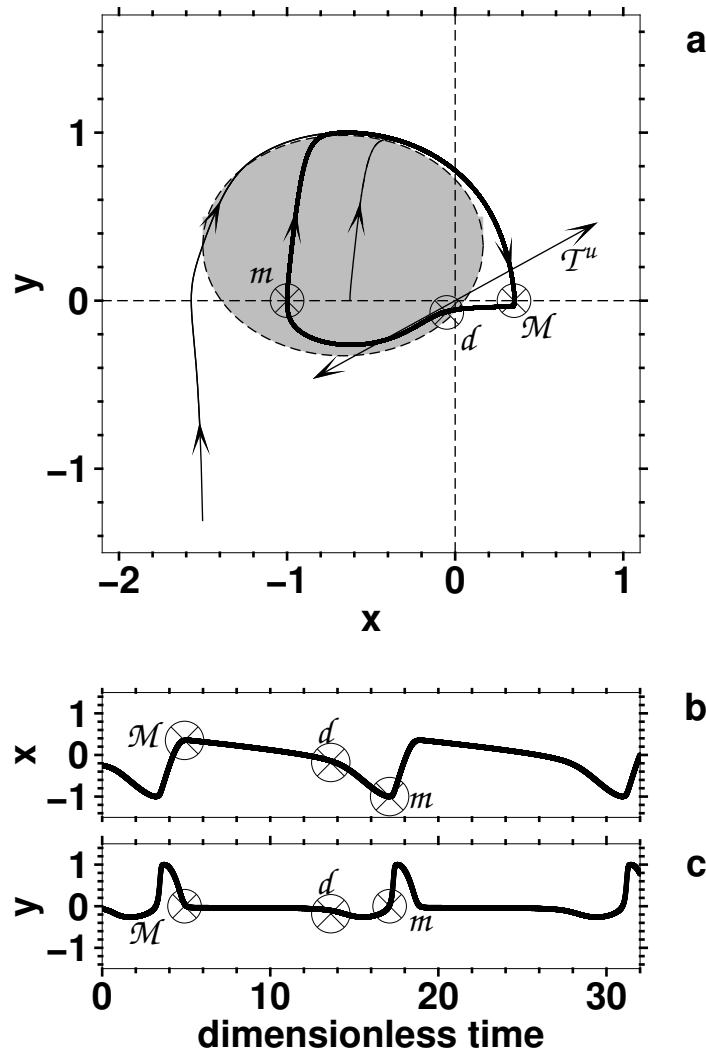


Figure 3.4: Nonlinear oscillation of the idealized model governed by Eq. (3.2): (a) phase portrait in the (x, y) -plane, with $y = \dot{x}$; (b) and (c) the associated time series representing, respectively, x and y . All plots are computed using $\mu = 10$, $x_0 = 0.8$ and $y_0 = -0.5$ in the equations. In panel (a), the closed trajectory (heavy solid line) is the limit cycle. The light solid lines are typical trajectories converging to the limit cycle from the interior and the exterior of this cycle. The shaded area is the one where damping is negative, i.e. $\kappa > 0$ in Eq. (3.2). Arrows indicate the direction of motion on the limit cycle and on the trajectories that converge onto it. The light straight line through the origin, denoted by \mathcal{T}^u , indicates the unstable direction along which trajectories are ejected from the origin. Letters M , m and d in panels (a), (b) and (c) show, respectively, the time of maximum amplitude of x , minimum amplitude of x , and the slope break during the deflation phase. See text and Supplementary Materials for details.

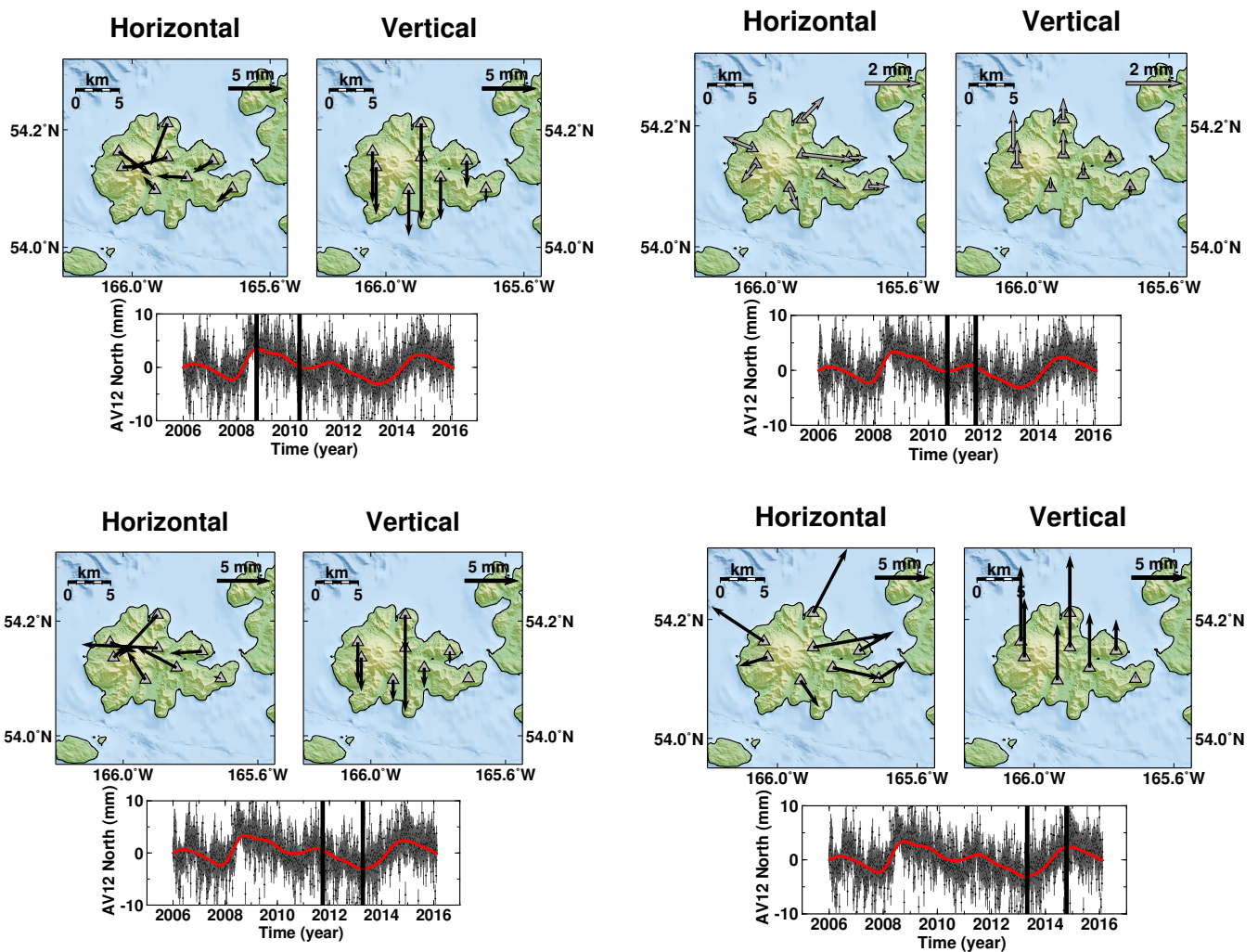


Figure 3.5: Same as Fig. 3.1 in the main text, but only for Akutan. In this case, successive episodes of inflation and deflation are included, as well as a separate map view of the vertical displacements for each episode of monotonic deformation.

3.11. FIGURES

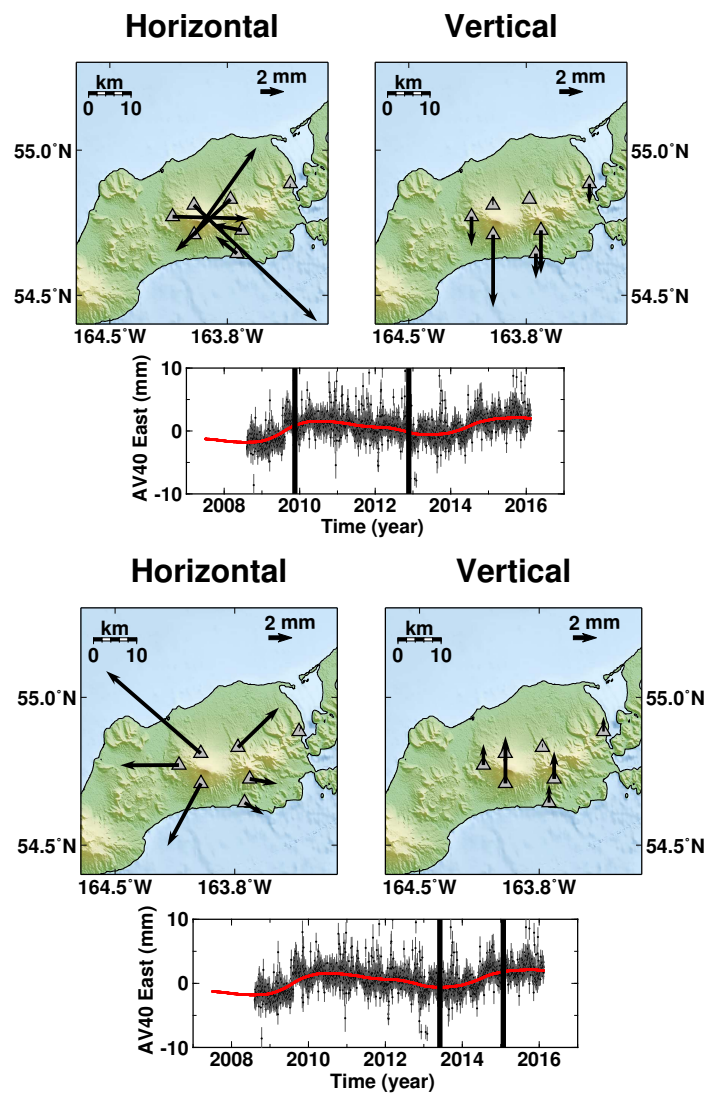


Figure 3.6: Same as Fig. 3.5, but for Shishaldin.

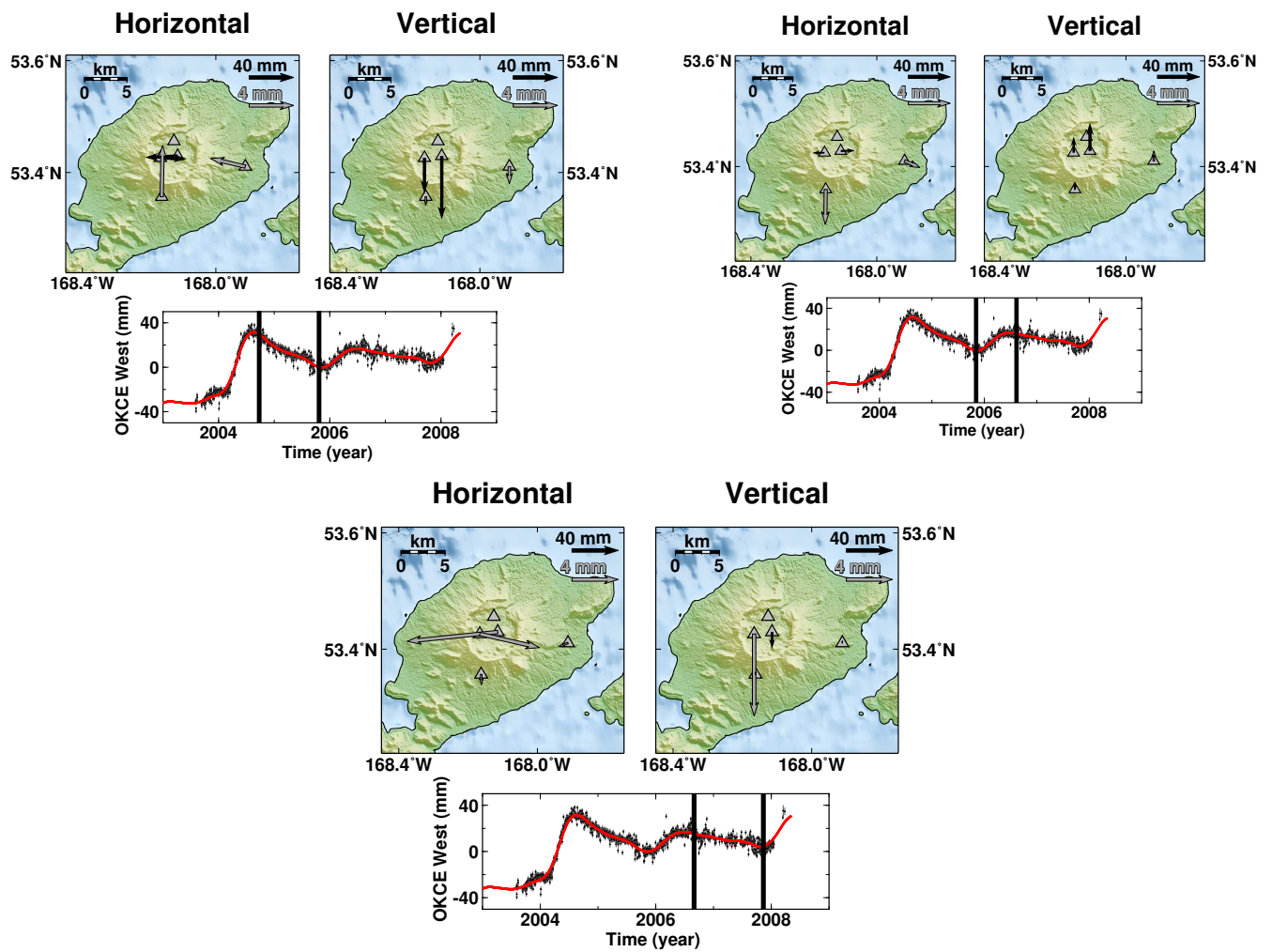


Figure 3.7: Same as Fig. 3.5, but for Okmok.

3.11. FIGURES

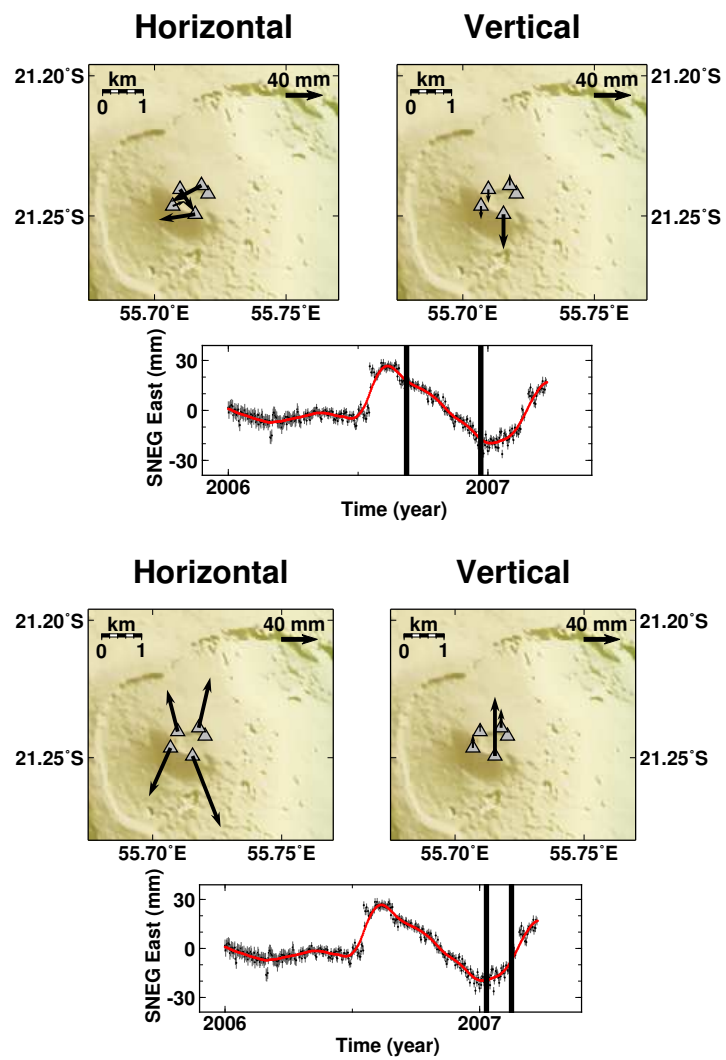


Figure 3.8: Same as Fig. 3.5, but for Piton de la Fournaise.

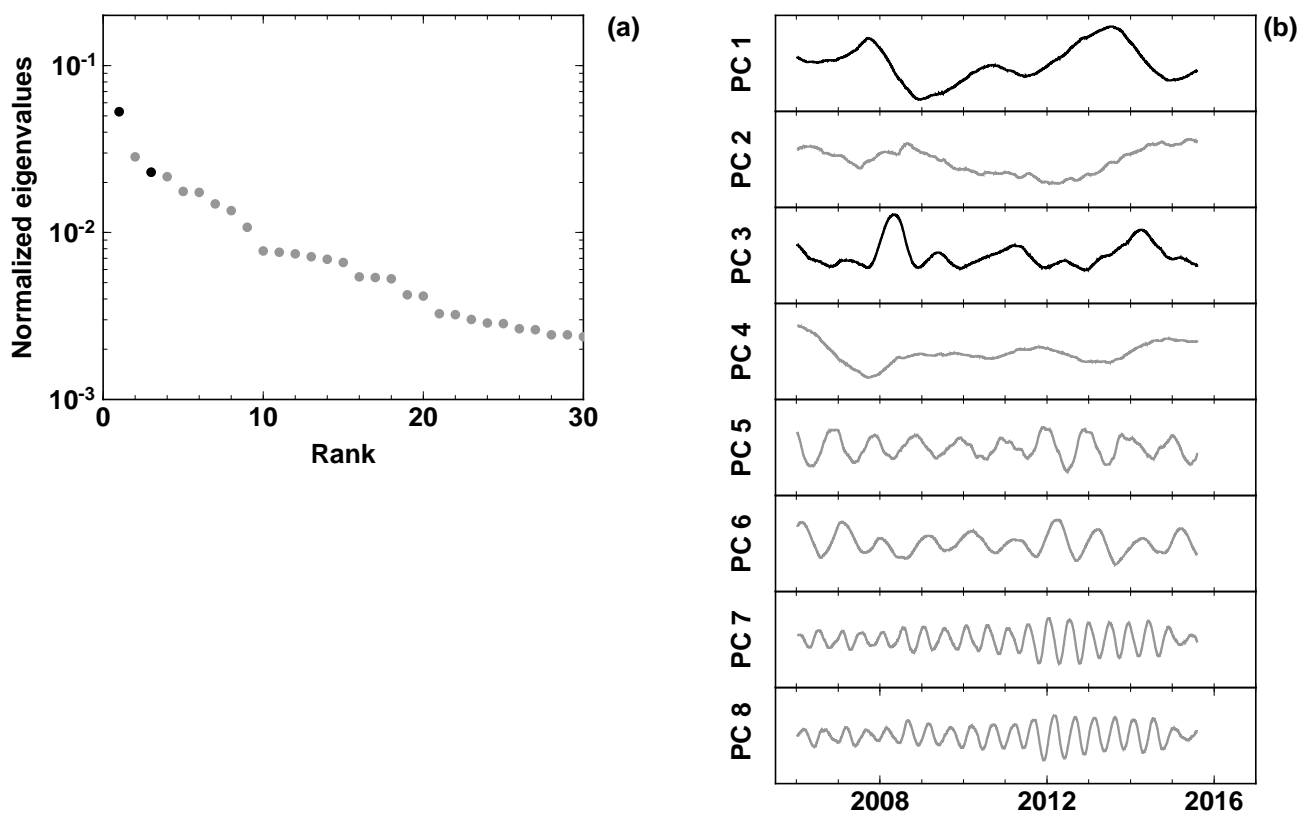


Figure 3.9: M-SSA analysis applied to the time series recorded at Akutan: (a) the 30 leading eigenvalues; and (b) the 8 leading PCs. The first and third PCs allow one to describe the temporal evolution of the volcanic system and produce the expected radial pattern of inflation and deflation episodes plotted in Figure 3.5.

3.11. FIGURES

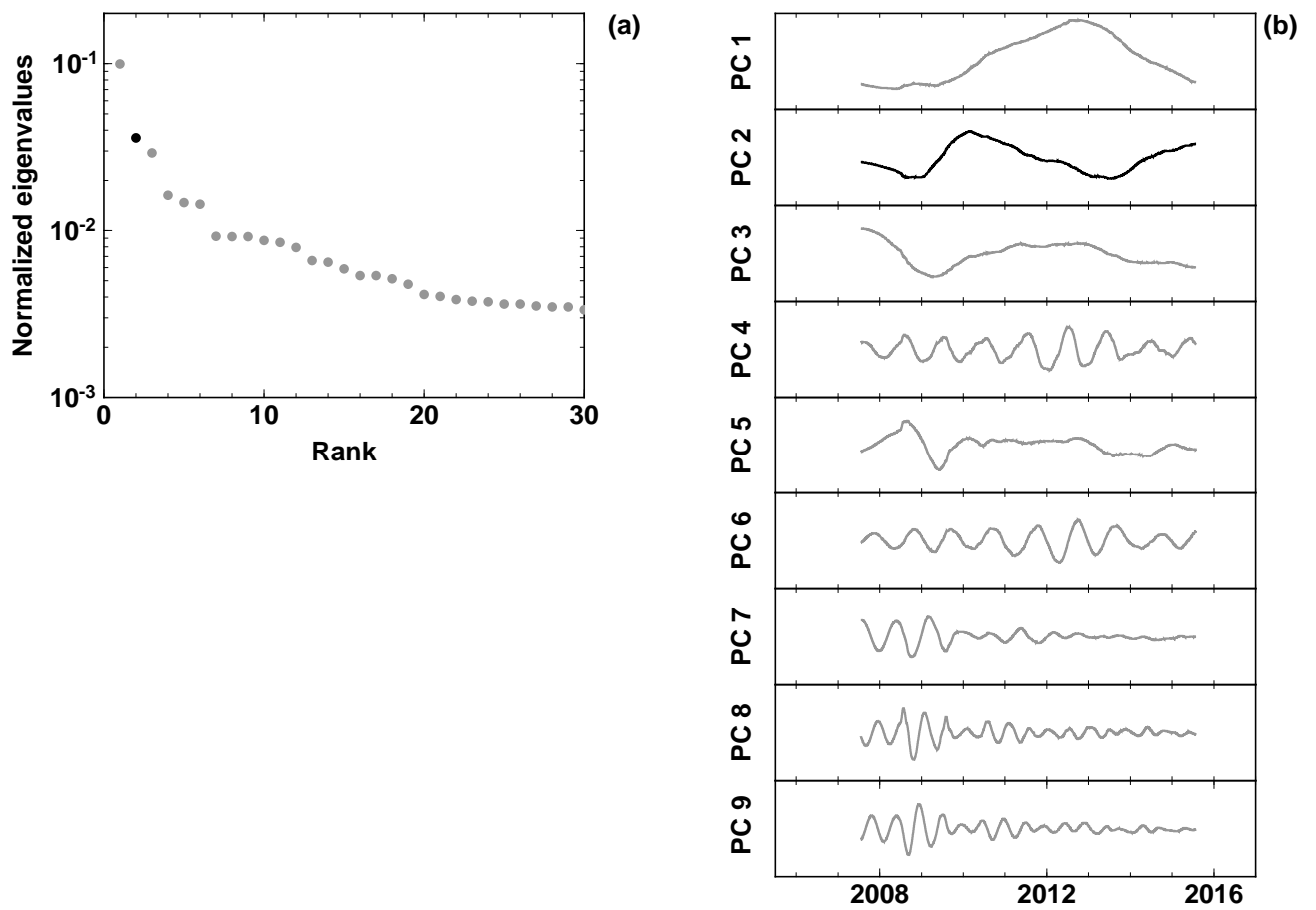


Figure 3.10: Same as Figure 3.9, but for Shishaldin. The number of leading PCs plotted in panel (b) is 9. Here, the second PC suffices to describe the temporal evolution of the volcanic system and reproduce the radial inflation and deflation patterns plotted in Figure 3.6.

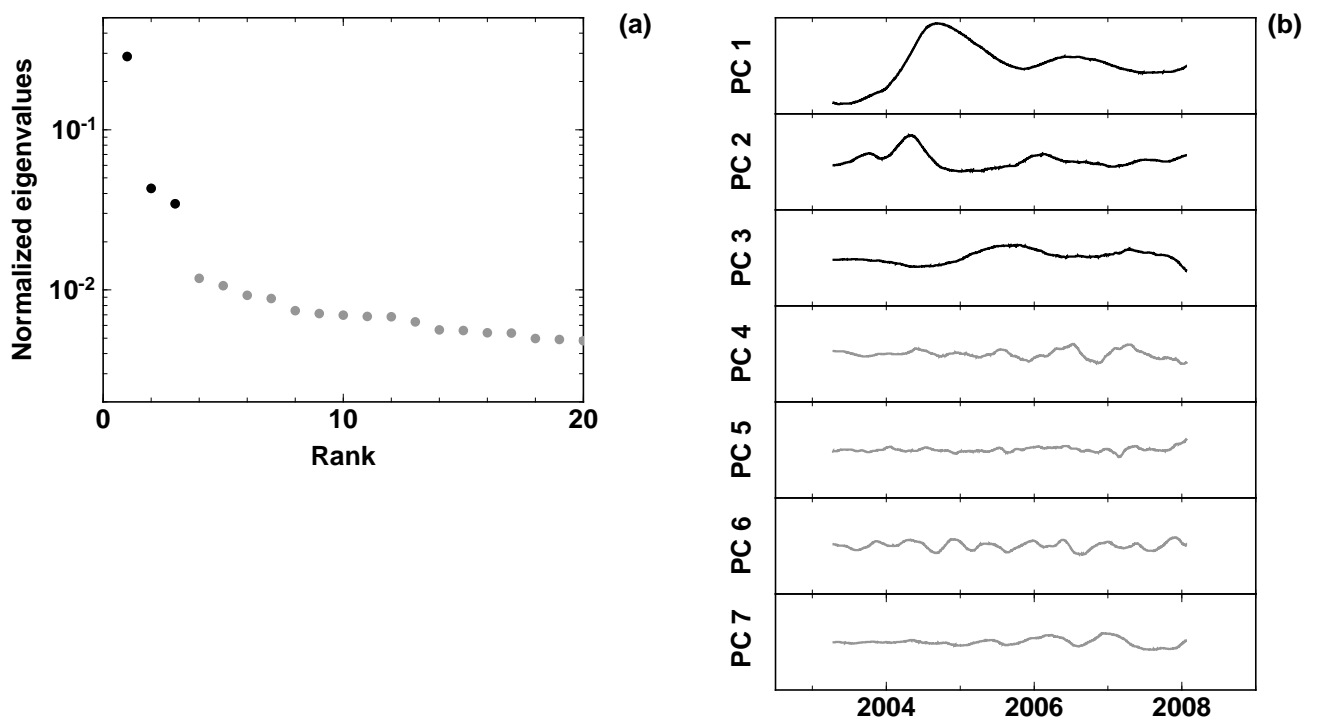


Figure 3.11: Same as Figure 3.9, but for Okmok: (a) the 20 leading eigenvalues; and (b) the 7 leading PCs. The first three PCs allow one to describe the temporal evolution of the volcanic system, along with the radial inflation and deflation patterns plotted in Figure 3.7.

3.11. FIGURES

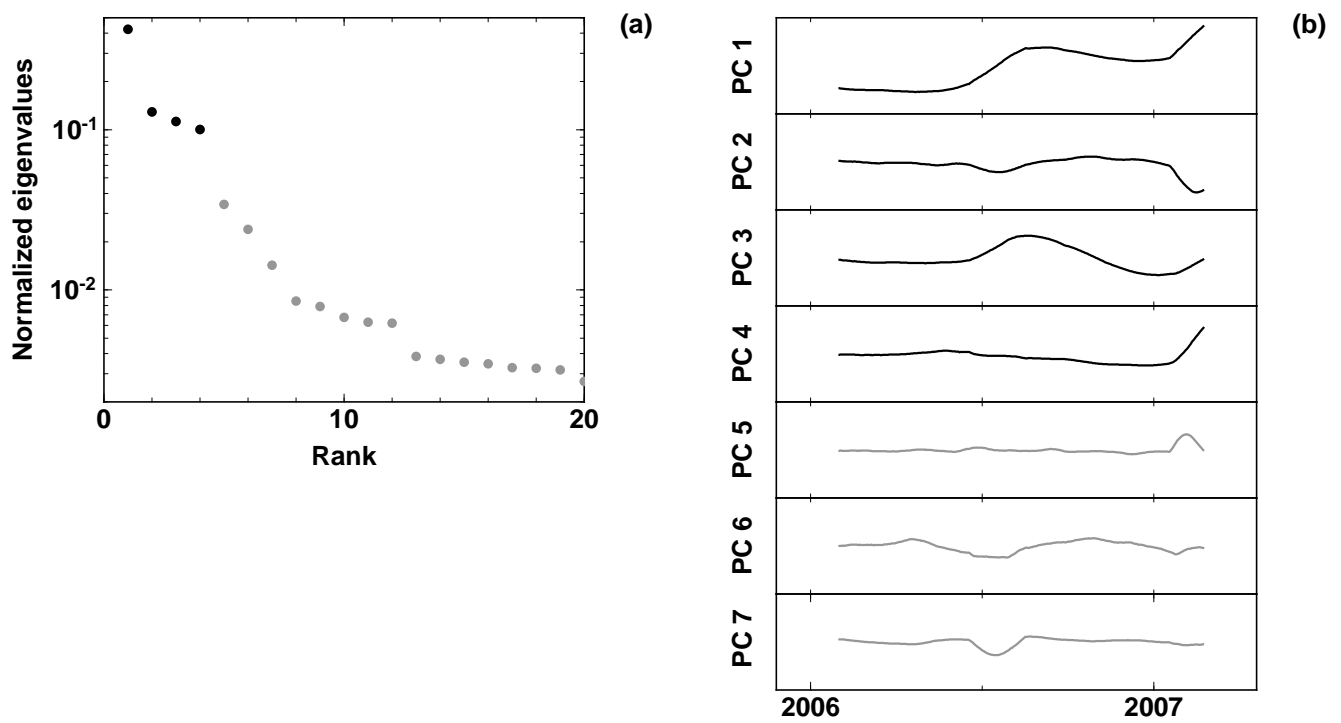


Figure 3.12: Same as Figure 3.11, but for Piton de la Fournaise. The first four PCs allow one to describe the temporal evolution of the volcanic system, along with the radial inflation and deflation patterns in Figure 4.2.

CHAPTER 4

A FLUID-DYNAMICS–BASED MODEL OF RESERVOIR OVERPRESSURE OSCILLATIONS AS INFERRED FROM GEODETTIC TIME SERIES

4.1 Abstract

Geodetic time series recorded at Okmok and Piton de la Fournaise reveal a pattern of fast and short inflations (that may be referred to as "pulses") followed by a longer time interval with no deformation or slower deflations. Such events are superimposed onto a longer period inflation. For both volcanoes a rapid inflation occurred just before a large eruption (in 2007 for Piton de la Fournaise and 2008 for Okmok), which suggests that the phenomenon underlying this kind of event may eventually trigger eruptions. Because geochemical, petrological, and geophysical data for both volcanoes suggest that their plumbing systems are composed of multiple reservoirs, we model such phenomenon as resulting from the hydraulic interaction between two shallow magma chambers connected by a vertical pipe and fed by a deeper source region. Episodes of periodic fast inflations occur when (1) a viscosity gradient is present in the vertical pipe, for instance as a result of a temperature gradient and (2) the flux supplying the shallow chambers is bounded by values that we derive analytically.

4.2 Introduction

Eruptions are often considered to occur when the overpressure inside a shallow magma chamber is large enough such that the tensile stress acting on the chamber's walls reach the tensile strength of the surrounding rock. The induced fracture can lead to the propagation of a dyke filled with magma from the reservoir that may reach the surface (e.g. Blake, 1981). Other scenarios involve for instance the failure of pre-existing magma-filled crack (McLeod and Tait, 1999). Monitoring the evolution of overpressure in a magmatic reservoir is key to understand the mechanism behind the onset of eruption. Deformation observations offer the opportunity to accomplish this task because the deformation of volcanic edifices is often directly related to magma chamber overpressure (e.g. Mogi, 1958; Segall, 2010).

The most common temporal pattern of deformation observed at volcanoes is that of exponential inflations and deflations (e.g. Dvorak and Okamura, 1987; Reverso et al., 2014). They can be explained by the linear dynamics of magma influx or outflux driven by a pressure gradient between a storage reservoir embedded in an elastic medium and either a deeper source region or the surface (e.g. Lenglin et al., 2008; Pinel et al., 2010; Jaupart and Tait, 1990). In this case, the characteristic time of deflation is smaller than the characteristic time of inflation, as observed for example at Kilauea volcano in Hawaii (Dvorak and Okamura, 1987).

Other deformation patterns, such as the one presented in the previous chapter, are more difficult to relate to physical processes and are thereby sometimes interpreted as the manifestation of ad hoc time-dependent forcing mechanisms — be it “pulses” of magma flux, degassing or heat flux — (e.g. Biggs et al., 2010, 2009; Peltier et al., 2009). Here we seek instead to understand these pulses as a manifestation of the internal variability of the magmatic system. As we shall see such an approach allows us to understand the conditions for which the occurrence of such "pulses" is possible.

4.3 Multiple reservoirs at Okmok and Piton de la Fournaise

4.3.1 Okmok

Okmok is a tholeiitic basaltic shield volcano located in the Aleutians island arc (figure 4.1). Larsen et al. (2013) have analyzed samples coming from cones and vents created during various eruptions in the last 1000-2000 yr. Their trace element compositions plotted against the SiO_2 weight fraction clearly show two distinct poles: (1) one for which the SiO_2 weight fraction of the lavas represent less than 53wt.% and (2) another corresponding to a slightly more evolved melt with a weight fraction of SiO_2 superior to 53wt.%. The two poles are clearly separated by $\simeq 1wt.$ % of SiO_2 (see figure 4 in Larsen et al. (2013)).

At first order, the magma evolved from 2000 years ago to present to become more enriched in silica. But recent materials from eruptions that occurred between 1900 and 1997 were more mafic than the preceding ones and correspond to pole (1), significantly breaking the long term evolution trend. The materials from the 2008 eruption shifted back to a more evolved magma, corresponding to pole (2). Melt inclusions in the crystals from some ejectas of the 2008 eruption are less evolved than the bulk magma of that eruption with a composition similar to the lavas from the 1997 eruption. According to Larsen et al. (2013) these observations suggest that a chamber containing an evolved magma was filled with a more mafic magma coming from a deeper reservoir before the 2008 eruption.

Seismic noise tomography reveals the presence of two distinct low velocity zones in Okmok subsurface (Masterlark et al., 2010). The deepest one is located ~ 5 km below the surface and is interpreted as a large reservoir connected to a more shallow low velocity zone. It is unclear however if the shallow low velocity zone corresponds to a single storage zone or is composed of several smaller reservoirs. Magnetotelluric tomography at Uturuncu volcano in Bolivia suggest a similar configuration with one large reservoir connected to several smaller shallow chambers (Comeau et al., 2015).

All the observations reported above suggest that the plumbing system of Okmok is composed of several shallow reservoirs containing magma of different compositions. The model proposed by Larsen et al. (2013) consist in one large reservoir around 5km depth that

supplies multiple smaller reservoirs around 2km depth. The presence of multiple reservoirs with magma of different compositions explains the rapid shift in lava composition between the 1997 eruption and the 2008 eruptions.

4.3.2 Piton de la Fournaise

Geochemical and petrological data obtained on samples from Piton de la Fournaise are reviewed in Peltier et al. (2009). All the erupted lavas are transitional basalts between the alkalic and the tholeiitic domain. The lavas from the recent activity can be separated in three types. The most abundant one is the so called "Steady State basalts" (SSB) characterized by a small range of variability of MgO content [5 – 8wt.% MgO]. The second one is an olivine-rich basalt that results from the crystallization and accumulation of forsterite, making it more concentrated in MgO than the "SSB" [8 – 28wt.% MgO]. Some authors suggest that crystals contained in this type of lava crystallized in a shallow storage zone located at $\simeq 2km$ depth (Famin et al., 2009). The third one is the "abnormal" group characterized among others things by a concentration of MgO that ranges between the SSB and the oceanite basalts [7.5 – 10wt.% MgO]. In the recent period, this last type of lava erupted in 1998.

The study of melt inclusions in Piton de la Fournaise lavas that erupted during the 2005 eruptions suggests that the crystallization depth of the olivine was shallow between 0km and 2.5km depth (Famin et al., 2009). The maximum estimated depth for the entrapment of melt inclusions is consistent with the depth of the source as determined from geodetic measurements of deformation and with the source of most of the seismicity that is between 200m and 2.5km (Peltier et al., 2009).

Some seismic events were also located at 7.5km depth in 2005 and 2007. Before the March 1998 eruption a seismic swarm migrated from 7.5km to the surface (Battaglia et al., 2005). The geochemistry of the "abnormal" type of lava (erupted in 1998) shows that it has undergone a fractionation process suggesting an origin that is consistent with the depth of this type of seismicity (Boivin and Bachèlery, 2009).

These observations all together led some authors to propose that the shallow plumbing

4.4. OKMOK AND PITON DE LA FOURNAISE GEODETIC TIME SERIES

system of Piton de la Fournaise is composed of at least two storage zones. The first one corresponds to the source of surface deformation and is located around 2km below the surface. It is probably connected to a shallower network of dikes and sills. The second one corresponds to the source of the deepest seismicity located around 7.5km below the surface. The presence of several storage zones also explains the differences in the chemistry of the recently erupted lavas. A schematic representation of the plumbing system described here is proposed in figure 8 of Famin et al. (2009).

4.4 Okmok and Piton de la Fournaise geodetic time series

4.4.1 Okmok (1997-2008)

The history of the surface deformations at Okmok from the end of the 1997 eruption to the beginning of 2008 eruption (figure 4.3a and 4.3b) derived from InSAR and GPS data shows that the 1997 co-eruptive deflation was followed by an inflation. The rate of inflation exponentially decreases until becoming almost null in mid-2002 (see also *e.g.*, Lu et al. (2010) for the corresponding InSAR images).

Then Okmok starts to inflate again with a progressively decreasing rate until the eruption of 2008. Two time scales associated with these two episodes of inflation have been estimated by fitting exponential functions to the InSAR time series and are respectively $\tau_1 \simeq 2.2\text{year}$ and $\tau_2 \simeq 1.1\text{year}$ (figure 4.3a). The rate of inflation of the second phase of deformation is decreasing faster than the first one.

An interesting observation revealed by the higher temporal resolution and accuracy of GPS data is a change in the temporal deformation pattern before the 2008 eruption. From 2004 to 2008, oscillations characterized by two cycles of fast and relatively short inflation followed by longer, almost flat, subsidence are superimposed to the second phase of inflation mentioned above (figure 4.3b and see also Biggs et al. (2010)). The amplitude of the second cycle is smaller than the first one so the whole pattern is reminiscent of damped oscillations. The last deflation of the second cycle is followed by a fast inflation that is directly followed by the co-eruptive subsidence caused by the 2008 eruption.

4.4.2 Piton de la Fournaise (2003-2007)

An example of GPS position time series recorded at the summit of Piton de la Fournaise is displayed in figure 4.4a and 4.4b. Before the large 2007 eruption, the time series shows a roughly linear inflation of the summit, punctuated by phases of sharp inflations. The discrete phases of rapid inflations are sometimes directly followed by eruptive or intrusive activities that are indicated by the grey areas in figure 4.4a. Some of the eruptions caused small amplitude deflations.

Similarly to Okmok volcano, a large eruption in 2007 is preceded by successive episodes of fast inflations that started around 2006.5 (figure 4.4b). We may also notice that the co-eruptive subsidence of April 2007 is directly preceded by a fast inflation.

4.5 Theoretical model of magma reservoirs interaction

4.5.1 Fluid flow in a cylindrical pipe with temperature dependent viscosity

Classical linear hydraulic interactions between reservoirs cannot spontaneously give rise to oscillations or to alternating fast and slow dynamics as observed at Piton de la Fournaise and Okmok (appendix 4.9). Here we introduce a model of fluid flow in a vertical cylindrical pipe along which a vertical, temperature-driven viscosity gradient exists. As the magma rises through the pipe, part of the advected heat is lost by heat diffusion through the pipe wall in the surrounding medium. The resulting change of temperature of the magma induces a change of viscosity as described quantitatively below. The pipe connects two magma chambers, the bottom one continuously fed from below and feeding the upper one through the vertical pipe. We build on the theory developed by Whitehead and Helfrich (1991) which is supported by experimental observations. These authors were interested in both the spatial and temporal behavior of such flow and developed their theory in Cartesian coordinates. Here, as we are interested mostly in the time dependent characteristics of the flow we use instead a cylindrical system of coordinates.

We assume that the flow is in a laminar regime and that the vertical velocity is the only non null component of the velocity field. We consider the horizontally averaged

4.5. THEORETICAL MODEL OF MAGMA RESERVOIRS INTERACTION

momentum equation in the vertical direction

$$\frac{dw}{dt} = -\frac{1}{\rho} \frac{dP}{dz} - \rho g - \frac{8\nu(T)w}{a^2} \quad (4.1)$$

where w is the horizontally averaged vertical velocity, P is the fluid pressure, ρ and g are the bulk density of the magma and the gravity acceleration, $\nu(T)$ is the temperature dependent kinematic viscosity and a is the radius of the pipe (e.g., Jaupart and Tait, 1990).

It may seem paradoxical to consider a laminar flow for which the Reynolds number is a priori small and at the same time add a time dependent inertial term $\rho dw/dt$ in the momentum equation. As we shall see, because the viscosity varies with temperature, we cannot neglect a priori dw/dt based on dimensional analysis. This is due to the fact that as Re tends toward 0, expression 4.1 does not necessarily tend toward a constant value (see Barenblatt (1996) p.10). Contrary to the case where the viscosity is kept constant and for which a priori neglecting dw/dt is valid, here the inertial term has to be present in the equation and, as we will see, plays an important role in the dynamics of the phenomenon we are studying.

The viscosity is assumed to depend linearly on the temperature as described by

$$\nu(T) = \nu_H + \alpha(T_H - T). \quad (4.2)$$

We assume a steady state regime for the temperature inside the cylindrical pipe, *i.e.*,

$$w \frac{\partial T}{\partial z} = \kappa \frac{1}{r} \frac{\partial}{\partial r} \left(r \frac{\partial T}{\partial r} \right). \quad (4.3)$$

The vertical temperature advection is equilibrated by the radial temperature diffusion.

The boundary condition on the wall, *i.e.*, at $r = a$ is linearly dependent of depth

$$T = T_H - \frac{\Delta T}{L} z. \quad (4.4)$$

This allows us to consider simply —together with the steady-state temperature equation— that a vertical temperature gradient develops in the pipe and its surrounding as the magma

**CHAPTER 4. A FLUID-DYNAMICS–BASED MODEL OF RESERVOIR
OVERPRESSURE OSCILLATIONS AS INFERRED FROM GEODETIC TIME SERIES**

is rising (see *e.g.*, Jaupart and Mareschal (2010) page 325, Delaney and Pollard (1982) and Bruce and Huppert (1989)).

One can verify that

$$T = T_H - \frac{\Delta T}{L}z + \frac{w\Delta T}{4\kappa La^2}(a^2 - r^2) \quad (4.5)$$

is a particular solution of equation 4.3. The homogeneous solution that have to be added to the particular one must have T equal to T_H when $z = 0$. But here —as done by Whitehead and Helfrich (1991)— for analytical convenience we approximate the temperature $r = 0$ and use the following approximate solution

$$\begin{aligned} T &= T_h \quad z < \frac{wa^2}{4\kappa} \\ T &= T_H - \frac{\Delta T}{L}z + \frac{w\Delta T}{4\kappa La^2} \quad \frac{wa^2}{4\kappa} < z < L \end{aligned} \quad (4.6)$$

which is consistent with the boundary conditions and in particular with $T = T_H$ at $z = 0$. The length defined by $L^* = wa^2/4\kappa$ is equivalent to the thermal entrance discussed in Delaney and Pollard (1982). It defines the depth below which most of the heat that entered the pipe still resides in the fluid.

Let's inject solution 4.6 into the momentum equation (4.1) and integrate it from the bottom to the top of the pipe. The integration gives

$$\frac{-1}{\rho}(\Delta P + \rho gL) = \begin{cases} \frac{8w}{a^2} [v_H L + \alpha \frac{\Delta T}{2L} (L - \frac{wa^2}{4\kappa})^2] + L \frac{dw}{dt} & w \leq \frac{4\kappa L}{a^2} \\ \frac{8v_H w L}{a^2} + L \frac{dw}{dt} & w > \frac{4\kappa L}{a^2} \end{cases} \quad (4.7)$$

Where ΔP is the difference of pressure between the bottom and the top of the pipe that drives the flow. Equation 4.7 couples the difference of pressure driving the flow with the vertical flow velocity and the rate of variation of the flow velocity.

Posing $L^* = L$ allows us to define a velocity scale $w^* = (4\kappa L)/a^2$, which in turn allows us to define a Reynold number

$$Re \equiv \frac{w^* \rho a}{\mu} = \frac{4\kappa L \rho}{a \mu} = \frac{1}{Pr} \times \frac{4L}{a} \quad (4.8)$$

4.5. THEORETICAL MODEL OF MAGMA RESERVOIRS INTERACTION

where $Pr \equiv \nu/\kappa$ is the Prandtl number (Delaney and Pollard, 1982). If we consider a basaltic magma with a viscosity $\mu \simeq 10^2 Pa.s$, a density $\rho \simeq 3.10^3 kg.m^{-3}$ and make the assumption that both the magma and the surrounding rock have the same thermal diffusivity $\kappa = 10^{-6} m^2.s^{-1}$ and $L \simeq 10^3 m$ and $a \simeq 1 m$, then the corresponding Reynold number is $\simeq 10^{-1}$ which is small compared to 1. Such a reasoning based on dimensional analysis is generally used to neglect the inertial term $\rho dw/dt$ in the momentum equation 4.1. But as already stressed out, because of the nonlinearity of the relationship relating the vertical velocity and the pressure driving the flow, equation 4.7 may not tend toward a fixed limit when Re tends toward 0 (Barenblatt (1996) p. 10). Whether or not equation 4.7 tends toward a fixed value as Re tends toward 0 depends on the parameter values.

4.5.2 Two shallow magma reservoirs fed by a deeper source

Geochemistry, petrology and geophysics provide evidences that both volcanoes, Okmok and Piton de la Fournaise, have plumbing systems composed of multiple storage zones fed by basaltic magmas coming from a deeper source region (see section 4.3). Relying on such information, let's consider that flow in the cylinder presented above connects two shallow magma chambers.

As the magma is either flowing in or out one of the chamber, its volume changes. The change of volume ΔV can easily be related to a change of pressure ΔP inside the chambers by assuming that they are embedded in an elastic medium. In this case, the change of pressure is given by:

$$\Delta P = E \frac{\Delta V}{V}. \quad (4.9)$$

For an incompressible magma, the coefficient E depends on both the intrinsic elastic properties of the surrounding rocks and the geometry of the chambers. For example $E = \frac{4}{3}G$ for a spherical magma chamber, where G is the shear modulus of the surrounding rocks (Tait et al., 1989; Delaney and McTigue, 1994). We may refer to E as the effective bulk modulus of the magma chambers (Huppert and Woods, 2002).

The volumetric flux associated with the pipe that has a radius a_r is simply $w\pi a_r^2$. The two shallow chambers have pressure P_B and P_T respectively (subscripts B and T refer to bot-

**CHAPTER 4. A FLUID-DYNAMICS-BASED MODEL OF RESERVOIR
OVERPRESSURE OSCILLATIONS AS INFERRED FROM GEODETIC TIME SERIES**

tom and top). The deepest chamber is connected to a source region inside which the pressure P_S is constant and supplies the shallow reservoirs with a magma that has a constant viscosity through a cylindrical pipe of radius a_S and length L_S . The associated volumetric flow is $Q_S = \frac{a_S^4 \pi}{8\mu L_S} [P_S - P_B - \rho g L_S]$ (e.g., Lenglin et al., 2008; Pinel et al., 2010). A schematic representation of the system is displayed in figure 4.5.

Such a system is governed by the following three coupled differential equations

$$\begin{aligned}\frac{dP_B}{dt} &= \frac{a_S^4 E \pi}{V_B 8\mu L_S} [P_S - P_B - \rho g L_S] - w \frac{E \pi a_R^2}{V_B}, \\ \frac{dP_T}{dt} &= w \frac{\pi a_R^2 E}{V_T}, \\ \frac{dw}{dt} &= -\frac{8w}{a_R^2 L_R} \left[v_H L_R + \frac{\alpha \Delta T}{2L_R} \left(L_R - \frac{w a_R^2}{4\kappa} \right)^2 \right] + \frac{1}{\rho L_R} [P_B - P_T - \rho g L_R].\end{aligned}\tag{4.10}$$

The first equation relates the change of pressure in the deepest shallow chamber with the influx coming from the underlying source region and the outflux leaving toward the shallower reservoir. The second equation relates the change of pressure in the shallower chamber with the flux of magma arising from the chamber below. The third equation couples the variations of the vertical velocity of the magma with the difference of pressure between the two shallow reservoirs. If we consider that the pressures that drive the flows are the sum of the lithostatic pressures at the outlets of the pipes and the overpressure of the magma reservoirs then the former equations become:

$$\begin{aligned}\frac{dP_B}{dt} &= \frac{a_S^4 E \pi}{V_B 8\mu L_S} [\Delta P_S - \Delta P_B + \Delta \rho g L_S] - w \frac{E \pi a_R^2}{V_B}, \\ \frac{dP_T}{dt} &= w \frac{\pi a_R^2 E}{V_T}, \\ \frac{dw}{dt} &= -\frac{8w}{a_R^2 L_R} \left[v_H L_R + \frac{\alpha \Delta T}{2L_R} \left(L_R - \frac{w a_R^2}{4\kappa} \right)^2 \right] + \frac{1}{\rho L_R} [\Delta P_B - \Delta P_T + \Delta \rho g L_R].\end{aligned}\tag{4.11}$$

where $\Delta \rho = \rho_r - \rho$ is the density contrast between the surrounding rocks and the magma, ΔP_S , ΔP_B and ΔP_T are the overpressure of the corresponding reservoirs. The system of equations 4.11 shows that the fluid flow is driven by both the chamber overpressure and the buoyancy of the magma (Jaupart and Tait, 1990). If $\Delta \rho$ is kept as a constant, the buoyancy term acts as a constant flux and constitutes a constant forcing term.

4.5. THEORETICAL MODEL OF MAGMA RESERVOIRS INTERACTION

4.5.3 Dimensions

The dimensionless variables —denoted with primes— are defined by

$$\begin{aligned} w &= w'w^*, & w_r &= \frac{4\kappa L_R}{a_R^2}, \\ t &= t' \frac{8\mu L_S V_B}{E\pi a_S^4}, \\ P &= P' \left[\frac{L_R \rho 8\nu_H w^*}{a_R^2} \right]. \end{aligned} \quad (4.12)$$

The velocity scale w^* is the one mentioned in the section 4.5.1 and corresponds to the velocity above which most of the heat still resides in the magma (Delaney and Pollard, 1982). The time scale is the characteristic time scale associated with the balance of pressure between one shallow reservoir of volume V_B and a deep source region (e.g. Pinel et al., 2010). Finally the pressure scale is a viscous pressure scale that can be extracted from the steady state version of the momentum equation (equation 4.1).

By injecting the above expressions of the variables in equations 4.11, dropping the primes, and considering that $\Delta\rho = 0$ we end up with the following dimensionless system of equations

$$\begin{aligned} \frac{d\Delta P_B}{dt} &= \Delta P_S - \Delta P_B - w \frac{L_S a_R^4}{L_R a_S^4}, \\ \frac{d\Delta P_T}{dt} &= w \frac{V_B a_R^4 L_S}{V_T a_S^4 L_R}, \\ \frac{dw}{dt} &= \gamma [f(w) + \Delta P_B - \Delta P_T]. \end{aligned} \quad (4.13)$$

where

$$f(w) = \begin{cases} -w(1 + \frac{A}{2}(1-w)^2) & w \leq 1 \\ -w & w > 1. \end{cases} \quad (4.14)$$

Four dimensionless parameters appear in equation 4.13:

$$\gamma = \left(\frac{8\nu_H^2}{a_S^2} \right) \frac{\rho L_S V_B}{E\pi a_R^2}, \quad A = \frac{\alpha \Delta T}{\nu_H}, \quad B = \frac{a_R^4 L_S}{a_S^4 L_R}, \quad C = \frac{V_B}{V_T}. \quad (4.15)$$

As detailed in the following section, the values of these four dimensionless parameters have a direct influence on the qualitative dynamics of the system.

4.5.4 Linear stability analysis and Hopf bifurcation

In order to understand the behavior of such a system and its relevance with respect to the geodetic observations presented in section 4.4, we consider first that the dimensionless flux entering the deepest reservoir is kept constant such that its value $Q \equiv [\Delta P_S - \Delta P_B] = cst$. The number of variables of the resulting system can be reduced by posing $X = \Delta P_T - \Delta P_B$, which leads to:

$$\frac{dX}{dt} = -Q + (1 + C)Bw, \quad (4.16a)$$

$$\frac{dw}{dt} = \gamma[f(w) - X]. \quad (4.16b)$$

Since B and C and γ are positive, it is clear from Eqs. 4.16a and 4.16b that this model contains the possibility of oscillatory solutions, as is the case for the linear system

$$\dot{x} = y, \quad \dot{y} = -x. \quad (4.17)$$

Whether this capacity to oscillate is realized for system 4.16 depends on parameter values, as we shall see below.

The system of differential equations 4.16 differs from the much simpler system 4.17 in two essential ways: (i) it is nonlinear, and (ii) it is not conservative. The nonlinearity appears in the damping, as in the classical Van der Pol oscillator, which is characterized by seesaw-shaped relaxation oscillations, as opposed to the sinusoidal oscillations of 4.17 (Guckenheimer and Holmes, 1983).

Like 4.17, 4.16 has a unique fixed point, *i.e.*, a single stationary solution that corresponds to $\frac{dX}{dt} = \frac{dw}{dt} = 0$, given by:

$$w_0 \left(\left(1 + \frac{V_B}{V_T}\right) \frac{L_S a_R^4}{L_R a_S^4} \right) = Q, \quad (4.18a)$$

$$X_0 = f(w_0). \quad (4.18b)$$

The first step to understand the dynamics governed by such a nonlinear system is to lin-

4.5. THEORETICAL MODEL OF MAGMA RESERVOIRS INTERACTION

linearize it around the fixed point 4.18. The linearization yields

$$\begin{aligned}\frac{dX}{dt} &= w\left(1 + \frac{V_B}{V_T}\right) \frac{L_S a_R^4}{L_R a_S^4} \\ \frac{dw}{dt} &= \gamma \left[\frac{df}{dw} \right]_{w_0} w - X.\end{aligned}\tag{4.19}$$

The eigenvalues of the linear system 4.19 are

$$\lambda_{\pm} = \frac{\gamma}{2} \left[\frac{df}{dw} \right]_{w_0} \pm \sqrt{\left[\frac{df}{dw} \right]_{w_0}^2 - \frac{4(C+1)B}{\gamma}}.\tag{4.20}$$

A nonlinear dynamical system is said to be linearly unstable when at least one of its eigenvalue have a positive real part. The fixed point loses its stability when $\left. \frac{df}{dw} \right|_{w_0}$ becomes positive — γ being always positive. In this case, any trajectory of the system starting near the fixed point will necessarily spiral away from it.

One can show that this transition is possible only for values of the fixed point defined by the inequality

$$\frac{2}{3} - \frac{1}{3} \sqrt{1 - \frac{6}{A}} < w_0 < \frac{2}{3} + \frac{1}{3} \sqrt{1 - \frac{6}{A}}\tag{4.21}$$

which enables us to extract two criteria for the fixed point to be unstable. First A needs to be larger than 6, otherwise $\left. \frac{df}{dw} \right|_{w_0}$ cannot be positive. Also from equation 4.18a and from the inequality 4.20 one can show that the flux Q of the magma feeding the shallow reservoirs needs to verify the following inequality

$$\left(\frac{2}{3} - \frac{1}{3} \sqrt{1 - \frac{6}{A}}\right)(C+1)B < Q < \left(\frac{2}{3} + \frac{1}{3} \sqrt{1 - \frac{6}{A}}\right)(C+1)B.\tag{4.22}$$

Far enough from the fixed point, $\left(\frac{df}{dw}\right)$ can change sign, thus giving rise to a limit cycle, *i.e.* a nonlinear oscillatory regime can take place when the fixed point becomes unstable (figure 4.16) (Grasman, 2011). Such oscillations have been coined "relaxation oscillations" and are characterized by the fact that their shapes are not necessarily sinusoidal as for the oscillations of the classical example of the Van der Pol oscillator (Van der Pol, 1926; Guckenheimer and Holmes, 1983). Their shapes vary from a system to another, here for example there is an asymmetry between the phase of increasing X and decreasing X which

leads to a sawtooth shaped oscillatory time series (figure 4.7b). Also their amplitudes do not depend on the initial conditions from which they arise but on the parameters of the system only contrary to classical harmonic oscillations of linear system (eq. 4.17).

Another way to understand the temporal behavior of the system 4.16 is to rewrite it as

$$\frac{dX}{dw}(f(w) - X) = \frac{1}{\gamma}(-Q + w(C + 1)B). \quad (4.23)$$

If we consider that $\frac{1}{\gamma}$ is a small parameter then

$$\frac{dX}{dw}(f(w) - X) \simeq 0 \quad (4.24)$$

which means that the trajectories of the system roughly follow the curves defined by $f(w) = X$ or $\frac{dX}{dw} = 0$, *i.e.*, vertical lines in the plane phase space w versus X . The composition of these two curves forms the so called limit cycle in the phase space X versus w shown in figure 4.7a.

The change in the dynamics of a nonlinear deterministic system from a unique stable fixed point to a stable closed orbit — like the one seen in Figure 4.7 — is called a Hopf bifurcation (Ghil and Childress, 1987; Guckenheimer and Holmes, 1983; Jordan and Smith, 2007).

4.6 Okmok: two successive exponential inflations followed by damped oscillations

4.6.1 Two successive exponential inflations

The first aspect of Okmok dynamics that needs to be understood is the occurrence of two consecutive episodes of exponential inflations that have different characteristic time scales called here τ_1 and τ_2 (see figure 4.3). A common way of explaining the presence of exponential inflations is to consider a shallow reservoir fed by a source region inside which the pressure is constant (e.g., Pinel et al., 2010). If we consider that the deepest shallow chamber is fed by a source and is not connected to any other reservoir then the evolution

4.6. OKMOK: TWO SUCCESSIVE EXPONENTIAL INFLATIONS FOLLOWED BY DAMPED OSCILLATIONS

of ΔP_B can be expressed analytically and

$$\Delta P_B = \Delta P_B(0) \exp\left(\frac{-t}{\tau_1}\right) + \Delta P_S(1 - \exp\left(\frac{-t}{\tau_1}\right)) \quad (4.25)$$

where $\tau_1 = \frac{V_B 8\mu L_S}{E\pi a_S^4}$. Here, the characteristic time scale τ_1 can be linked to the hydraulic connection between the source region and the shallow reservoir. This is also the time scale used to adimensionalized the system (eq. 4.11).

As shown in figure 4.3, the second exponential inflation phase occurred when the first started to become almost flat (figure 4.3a). This observation suggests that the second inflation phase is related to the transfer of magma from the shallow chamber considered above to another one because when the overpressure ΔP_B reaches a value large enough a new pathway —or already existing pathway— for magma may open —resp. re-open— allowing the transfer of magma to a shallower reservoir. If this scenario is correct, then the second exponential inflation phase can be related to the dynamics of pressure balance between two shallow chambers. If we neglect that the bottom shallow reservoir is connected to a source region then ΔP_B and ΔP_T evolve according to

$$\begin{aligned} \Delta P_B &= \frac{V_T}{V_B + V_T} (\Delta P_B(0) - \Delta P_T(0)) (1 - \exp\left(\frac{-t}{\tau_2}\right)) + \Delta P_B(0), \\ \Delta P_T &= \frac{V_B}{V_B + V_T} (\Delta P_T(0) - \Delta P_T(0)) (1 - \exp\left(\frac{-t}{\tau_2}\right)) + \Delta P_T(0) \end{aligned} \quad (4.26)$$

where in this case $\tau_2 = \frac{8\mu D_R}{E\pi a_R^4} \left(\frac{V_T V_B}{V_T + V_B}\right)$ (Reverso et al., 2014).

If we suppose that E and μ are the same for both pipes then

$$\frac{\tau_1}{\tau_2} = \frac{L_S a_R^4}{a_S^4 L_R} \left(\frac{V_T + V_B}{V_T}\right) \quad (4.27)$$

which means that τ_1 may be bigger than τ_2 —as it is the case for Okmok time series (figure 4.3)— if V_T is smaller than V_B .

Even though, at first order, the above reasoning may be acceptable, in all rigor the entire system —*i.e.*, the two reservoirs fed by the source region— should be treated as a whole because the transfer of magma between the two shallow reservoirs affects the pressure of

the bottom shallow reservoir that in turn affects the flux of magma from the source region. The dynamics of this system is governed by equation 4.13 with $A = 0$. Its resolution shows that in fact it possesses two characteristic time scales. One of them is larger than τ_1 and the other one larger than τ_2 but smaller than τ_1 (see appendix A).

4.6.2 The transition between the exponential inflations and the oscillations

The last phase of Okmok deformation before the 2008 eruption starts in 2004 when a damped oscillatory signal emerged from the second inflation phase (figure 4.3). This signal and the transition from the exponential trend can be explained using the system of differential equations 4.13.

As we saw above, the reduced system governed by equations 4.16a and 4.16b evolves in an nonlinear oscillatory regime only if the flux entering the system is bounded by values that depend on the dimensionless parameters A , B and C (inequality 4.22).

This is also valid for the system 4.13 even though in that case the flux is not a constant and depends on the value of the overpressure ΔP_B . From the inequality 4.22 we can derived thresholds for ΔP_B required for the emergence of an oscillatory regime. Such inequality is given by

$$\Delta P_S - \left(\frac{2}{3} + \frac{1}{3}\sqrt{1 - \frac{6}{A}}\right)(C + 1)B < \Delta P_B < \Delta P_S - \left(\frac{2}{3} - \frac{1}{3}\sqrt{1 - \frac{6}{A}}\right)(C + 1)B. \quad (4.28)$$

The figure 4.8 shows time series of evolving overpressure governed by equations 4.8. As the pressure equilibrates between the shallow reservoirs and the source region, ΔP_B and ΔP_T increase. When P_B reaches the lower threshold defined in inequality 4.28, the overpressure starts to oscillate in a sawtooth manner like in figure 4.7b. These oscillations are superimposed onto the overall trend of exponential pressure increase and are slightly damped as the flux entering the shallow system decreases. When the pressure ΔP_B reaches the upper threshold of inequality 4.28 the oscillations cannot be sustained anymore.

This qualitative dynamics can be directly compared to observations at Okmok. The fact that at Okmok the oscillations start when the rate of inflation decrease and is damped suggests that the transition from the exponential inflation regime to the oscillatory one is

4.7. PITON DE LA FOURNAISE: AN IRREGULAR BEHAVIOR

controlled by the evolution of the flux entering the shallow system. Note also that, because the time in figure 4.8 is scaled by the characteristic time scale τ_1 associated to the pressure balance between a source region and a shallow reservoir, the period of the oscillations are also quantitatively consistent with observations at Okmok.

4.7 Piton de la Fournaise: an irregular behavior

4.7.1 On irregular temporal patterns

Although geodetic time series at Piton de la Fournaise show much more irregularity than Okmok, one can also observed a succession of fast inflation followed by intervals of rest or small subsidence superimposed onto a longer period inflation that, in this case, is roughly linear. Such observation suggests that the relaxation oscillations presented above may also play a role in the Piton de la Fournaise dynamics.

The irregularity is characterized by variations of the amplitudes and periods of the successive fast inflations and relatively quiet periods. Unlike Okmok volcano, the presence of an overall linear trend suggests that the variations of the amplitude and period of the events are not mainly controlled by the flux supplying the shallow system. The linear trend suggests a constant flux from the source region meaning that the reduced system 4.16 may be more adapted to Piton de la Fournaise time series than system 4.13.

An irregular temporal behavior may be understood by adding only one degree of freedom to the nonlinear system 4.16. In this case the irregularity is called "deterministic chaos" (see the seminal work of Lorenz (1963b) and *e.g.*, Ghil and Childress (1987) for examples in geophysics). Van der Pol (1940) gave a beautiful explanation — with no equations whatsoever — of how a relaxation oscillator can, in the presence of periodic forcing, lead to what is called nowadays "sensitive dependence on initial states", and hence irregular, chaotic behavior. Relying on this guideline, we can explore the processes that may induce changes in the parameter values that control both the period and amplitude of the relaxation oscillations.

The estimated difference of overpressure in the shallow reservoir necessary to explain

the differences of amplitude of the inflations events observed lie around $\simeq 1\text{MPa}$ (Peltier et al., 2008). The information exposed in section 4.3 allows us to consider that the length of the pipe connecting the two shallow reservoirs at Piton de la Fournaise is $L_R \simeq 5\text{km}$. If we consider that $a_R \simeq 1\text{m}$, $\mu \simeq 100\text{Pa}\cdot\text{s}$ and $\kappa \simeq 10^{-6}\text{m}^2\cdot\text{s}^{-1}$ then the pressure scale defined above takes the value $[P] \simeq 10^{-1}\text{MPa}$.

4.7.2 Effect of volatiles on the oscillations

If volatiles are present in the magma and are exsolved, the effective bulk modulus of the magma chamber — E — can change significantly. The work of Famin et al. (2009) based on lavas coming from the February and December 2005 eruptions shows that H_2O and CO_2 are present in melt inclusions that have been entrapped from $\simeq 2\text{km}$ depth and above. The concentration of H_2O present in the melt inclusions of the studied samples ranges from $\simeq 0.1\text{wt.}\%$ to $\simeq 0.6\text{wt.}\%$ (Famin et al., 2009). The concentration of CO_2 is much more smaller because its solubility is much lower. A significant fraction of CO_2 probably exsolved in the deepest part of the plumbing system and left it before the magma reaches the 2km depth storage zone (Boudoire et al., 2017).

The melt inclusions are thought to represent the parental magma that is then differentiated through crystallization processes in the chamber. Because the parental magma contains a significant amount of water, the differentiated melt that results from it can reach saturation and water can then exsolve. Although the estimation of the entrapment depth of the melt inclusions shows that H_2O exsolves probably mainly during the decompression associated to the ascension of the magma toward the surface, some may also exsolve in the chamber while crystallization occurs (see Tait et al. (1989) and the references therein).

Let's therefore make the assumption that only one volatile species (H_2O) is present when the melt arrives in the 2km depth shallow reservoir. We follow the formalism of Huppert and Woods (2002) to study how the presence of the volatile affect the bulk modulus of the magma chamber (see the appendix B for further details on the model). The computation of the variations of the effective bulk modulus as a function of the weight fraction of crystals are shown in figure 4.9. We choose two values for total H_2O content

4.8. CONCLUDING REMARKS

of the melt, $N = 2.5wt.%$ and $N = 3wt.%$, that are within the range measured in the melt inclusions. In both cases, as the crystal content increases, the resulting melt can reach H_2O saturation. At this point a huge drop of almost 2 orders of magnitude of the value of the effective bulk modulus occurs.

A drop of E of two orders of magnitude leads to an increase of γ of two order of magnitude. The pressure evolution of P_T in the case of a constant flux coming from the source region to the shallow system for $\gamma = 0.1$ and $\gamma = 10$ are shown in figure 4.10. As shown, such change of amplitude in γ leads to both amplitude and period variations of the oscillations of pressure inside the reservoir. The order of magnitude of the difference of pressure associated with the amplitude of the oscillations is $\simeq 10 \times [P]$. Because as estimated $[P] \simeq 10^{-1}MPa$, the amplitude difference is $\simeq 1MPa$ which is consistent with the amplitude variation of overpressure from one event to the other (Peltier et al., 2009).

4.8 Concluding remarks

4.8.1 Summary

Okmok and Piton de la Fournaise have similar plumbing systems composed of several storage zones. The dynamics of both systems reflected the GPS derived deformation time series can be understood by the study of the interaction of two reservoirs connected by a pipe in which the magma has a viscosity that depends on temperature. For a certain range of parameter values, the pressure inside the shallow reservoirs can oscillates between phases of fast variations of pressure and opposite phases of slow variations of pressure.

At Okmok the oscillations are damped and superimposed onto an exponential inflation. Because the oscillations can only be sustained when the flux of magma feeding the magma chambers is bounded by specific values, the onset of the oscillations appears to be controlled only by the evolution of the flux of magma coming from the source region.

GPS time series at Piton de la Fournaise show much more irregularity. The successive fast inflations and quiet periods are superimposed onto a quasi linear trend. The period and amplitude of the cycles of inflation can be the result of the variations of several param-

eters of the model presented above. In particular, because the melt entering the shallowest reservoir contains a significant portion of water, the exsolution of volatile species can lead to a significant change of the effective bulk modulus of the magma chambers that leads, in turn, to the modification of the amplitude and period of the successive fast inflations observed.

4.8.2 Relaxation oscillations as a mechanism for triggering eruptions?

At Piton de la Fournaise, within the studied period (2003-2007), almost all fast inflations are followed either by eruptions or intrusive events. In particular the largest eruption of April 2007 is also preceded by such "pulses" (figure 4.4 a and b). At Okmok the two damped oscillations presented above are followed by a fast inflation that is itself followed by the 2008 eruption. These observations prompt the question of a link between the phase of fast inflations associated with the oscillations and the triggering of eruptions.

From a purely mechanical standpoint, a classical way to see how eruptions are triggered is to consider that the overpressure can be large enough for the wall tensile stress of the magma chamber to reach the tensile strength. In this case the induced tensile fracture can eventually reach the surface and generate an eruption (Blake, 1981). At Okmok this mechanism may explain the onset of the eruption; the last fast inflation allowing the overpressure to reach the critical value faster than it would without the oscillations.

But GPS time series at Piton de la Fournaise shows that eruptions —although often small— can occur at different level of overpressure inside the chamber because they occur at different moment along the linear trend reflecting the pressurization of the shallow magma chambers. In this case both the value of the overpressure and the rate of variation of the overpressure seem to play a role in the mechanism of eruption triggering. The purely mechanical standpoint exposed above that depends only on the value of the overpressure may not be appropriate.

A way to understand the effect that could have the rate of variation of overpressure is to consider for example the solidification of magma during dyke propagation (Taisne and Tait, 2011). Higher rate of overpressure would allow higher flux of magma inside an

4.9. APPENDIX A: LINEAR HYDRAULIC INTERACTION OF TWO SHALLOW RESERVOIRS FED BY A SOURCE REGION

opening dyke and therefore a larger amount of advected heat inside the dyke. This would prevent the magma to solidify, allowing for the intrusion to reach the surface and give rise to an eruption.

4.8.3 Conclusion

We conclude that episodes of fast inflations followed by more longer quiet periods can be explained for by a model of hydraulic reservoir interaction that takes into account viscosity variations of the magma. This behavior indicates the presence of a nonlinear oscillatory regime that arise when : (i) the flux supplying the shallow system is bounded between specific values and (ii) the viscosity variations are sufficiently high. Such a regime explains the "pulses" as a manifestation of the internal variability of the magmatic system instead of the result of time "ad hoc" dependent external forcing.

4.9 Appendix A: Linear hydraulic interaction of two shallow reservoirs fed by a source region

Let's consider system 4.13 without any viscosity variations —*i.e.*, $A = 0$. In this case the system 4.13 reduces to

$$\begin{cases} \frac{d\Delta P_B}{dt} = \Delta P_S - \Delta P_B - B(\Delta P_B - \Delta P_T) \\ \frac{d\Delta P_T}{dt} = BC(\Delta P_B - \Delta P_T) \end{cases} \quad (4.29)$$

where B and C are two dimensionless parameters introduced in the main text (see table 4.11).

The solutions of the corresponding homogeneous system have necessarily the form

$$\begin{pmatrix} \Delta P_B \\ \Delta P_T \end{pmatrix} = \alpha \begin{pmatrix} e^{\lambda_1 t} \\ e^{\lambda_2 t} \end{pmatrix} \quad (4.30)$$

where α is a matrix containing coefficients that depend on the initial conditions. The

coefficients λ_1 and λ_2 are the eigenvalues of the matrix

$$\begin{pmatrix} -(B+1) & B \\ BC & -BC \end{pmatrix} \quad (4.31)$$

and are defined by:

$$\begin{cases} \lambda_1 = \frac{-(B(C+1)+1) + \sqrt{(B(C-1)-1)^2 + 4CB^2}}{2} \\ \lambda_2 = \frac{-(B(C+1)+1) - \sqrt{(B(C-1)-1)^2 + 4CB^2}}{2} \end{cases} \quad (4.32)$$

Because λ_1 and λ_2 are real values, system 4.29 cannot oscillate. It shows that the dynamics of the system 4.29 is associated with two time scales $\lambda_1 \times \frac{8\mu L_S V_B}{E\pi a_3^4}$ and $\lambda_2 \times \frac{8\mu L_S V_B}{E\pi a_3^4}$.

4.10 Appendix B: The link between the effective bulk modulus of a magma chamber and the volatile content of magmas

We follow Huppert and Woods (2002) to show how the presence of volatile can affect the effective bulk modulus of the magma chambers E . In the case where the bulk density of the magma varies the conservation of mass indicates that

$$\frac{d}{dt}(\rho V) = \rho \frac{dV}{dt} + V \frac{d\rho}{dt} = Q. \quad (4.33)$$

where Q is the total mass flux of magma either leaving or entering a chamber. The density ρ is a function of temperature, pressure, mass fraction of crystals and total mass fraction of volatile (dissolved plus exsolved). Differentiating expression 4.33 with respect to the density gives the following relationship

$$\frac{dV}{dt} + \frac{V}{\rho} \frac{\partial \rho}{\partial p} \frac{dp}{dt} = \frac{Q}{\rho} - \frac{V}{\rho} \frac{\partial \rho}{\partial T} \frac{dT}{dt}. \quad (4.34)$$

4.10. APPENDIX B: THE LINK BETWEEN THE EFFECTIVE BULK MODULUS OF A MAGMA CHAMBER AND THE VOLATILE CONTENT OF MAGMAS

As we already saw the change of volume inside a chamber can be related to the change of pressure by

$$\frac{dV}{dt} = \frac{V}{E} \frac{dP}{dt} \quad (4.35)$$

Injection 4.35 into equation 4.34 gives

$$V \left[\frac{1}{E} + \frac{1}{\rho} \frac{\partial \rho}{\partial P} \right] \frac{dP}{dt} = \frac{Q}{\rho} - \frac{V}{\rho} \frac{\partial \rho}{\partial T} \frac{dT}{dt} \quad (4.36)$$

We can identify the left hand side of equation 4.36 with the right hand side of equation 4.35 to define an effective bulk modulus for magma chamber with compressible magma which is defined according to

$$\frac{1}{\bar{E}} = \frac{1}{E} + \frac{1}{\rho} \frac{\partial \rho}{\partial P}. \quad (4.37)$$

The effective modulus for magma chamber that contains volatile \bar{E} can be calculated with an expression of the bulk density as a function of the pressure P . We use the following expression for the bulk density:

$$\rho = \left[\frac{n}{\rho_g} + (1-n) \left(\frac{x}{\rho_c} + \frac{1-x}{\rho_m} \right) \right]^{-1}, \quad (4.38)$$

where ρ_g and ρ_c are respectively the gas density and the crystals density, x is the weight fraction of crystals and n is the weight fraction of exsolved volatile.

The gas density follows an ideal gas law

$$\rho_g = \frac{P}{RT} \quad (4.39)$$

where R is the universal gas constant. The exsolved volatile content n is assumed to follow the Henry's law. For water the law expresses $n = N - sP^{1/2}(1-x)$ when the magma reaches saturation, *i.e.*, $n \geq 0$, otherwise $n = 0$. N is the total volatile content and $s = 4 \times 10^{-6} Pa^{-1/2}$.

4.11 Table

| Description | Symbols |
|---|--|
| <i>Variables</i> | |
| Pressure in the top magma chamber | P_T |
| Pressure in the bottom magma chamber | P_B |
| Overpressure in the top magma chamber | ΔP_T |
| Overpressure in the bottom magma chamber | ΔP_B |
| Horizontally average vertical velocity | w |
| Difference of overpressures | $X = \Delta P_T - \Delta P_B$ |
| <i>Geometrical parameters</i> | |
| Feeding pipe length | L_S |
| Shallow pipe length | L_R |
| Feeding pipe radius | a_S |
| Shallow pipe radius | a_R |
| <i>Magma properties</i> | |
| Dynamic viscosity | μ |
| Kinematic viscosity | ν |
| Density | ρ |
| Thermal diffusivity | κ |
| Density contrast | $\Delta\rho$ |
| <i>Country rock properties</i> | |
| Density | ρ_r |
| Shear modulus | G |
| <i>Magma chambers properties</i> | |
| Volume of the top magma chamber | V_T |
| Volume of the bottom magma chamber | V_B |
| Effective bulk modulus | E |
| Effective bulk modulus for compressible magma | \bar{E} |
| <i>Important dimensionless parameters</i> | |
| | $\gamma = \left(\frac{8\nu_H}{a_R^2}\right)^2 \frac{\rho D_R V_T}{E\pi a_R^2}$ |
| | $A = \frac{a\Delta T}{\nu_H}$ |
| | $B = \frac{a_R^4 L_S}{a_S^4 L_R}$ |
| | $C = \frac{V_B}{V_T}$ |

Table 4.1: List of main variables and parameters described in the main text.

4.12 Figures

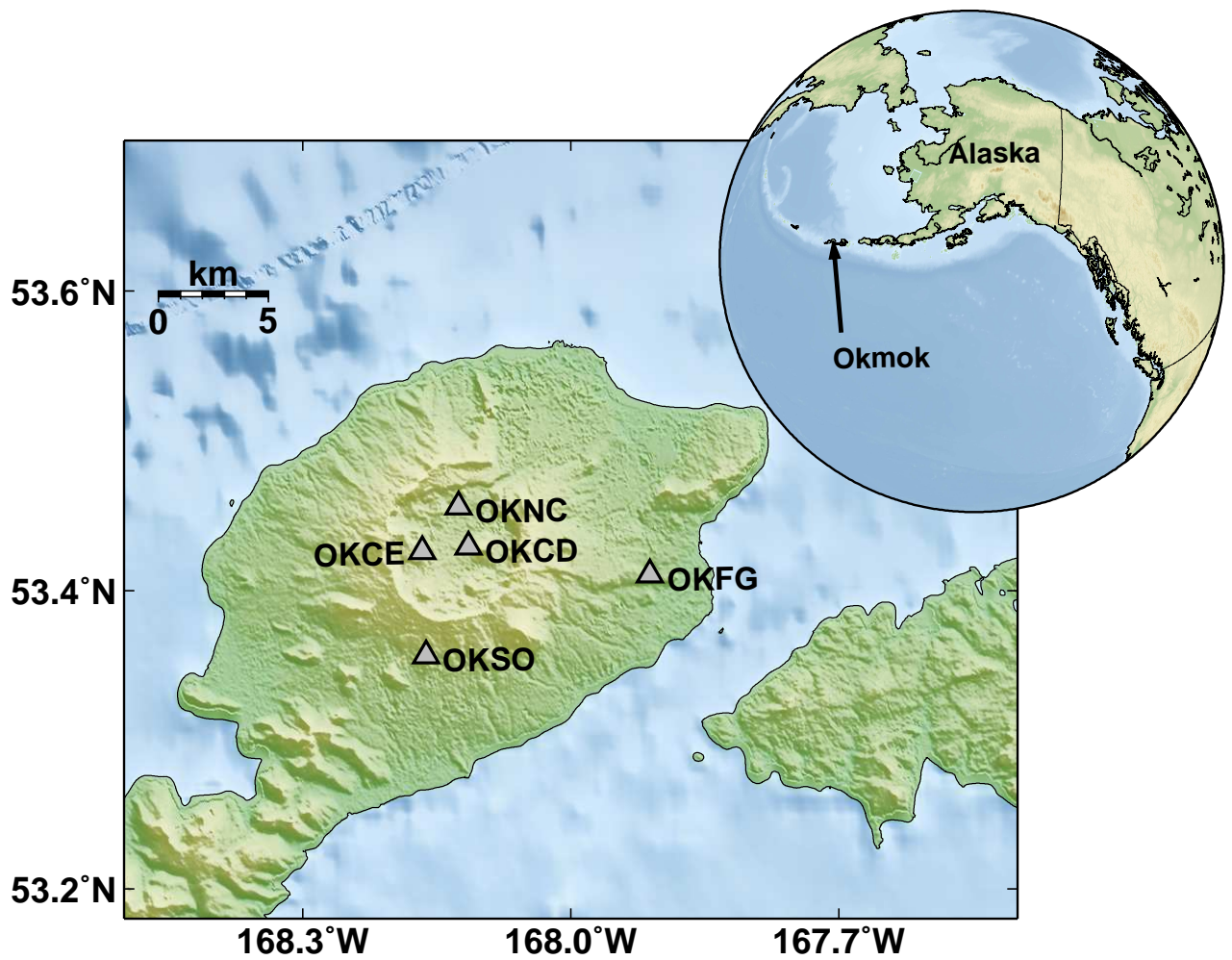


Figure 4.1: Location map of Okmok showing the GPS sites (grey triangles) from which the displacement time series used here have been extracted

CHAPTER 4. A FLUID-DYNAMICS-BASED MODEL OF RESERVOIR OVERPRESSURE OSCILLATIONS AS INFERRED FROM GEODETIC TIME SERIES

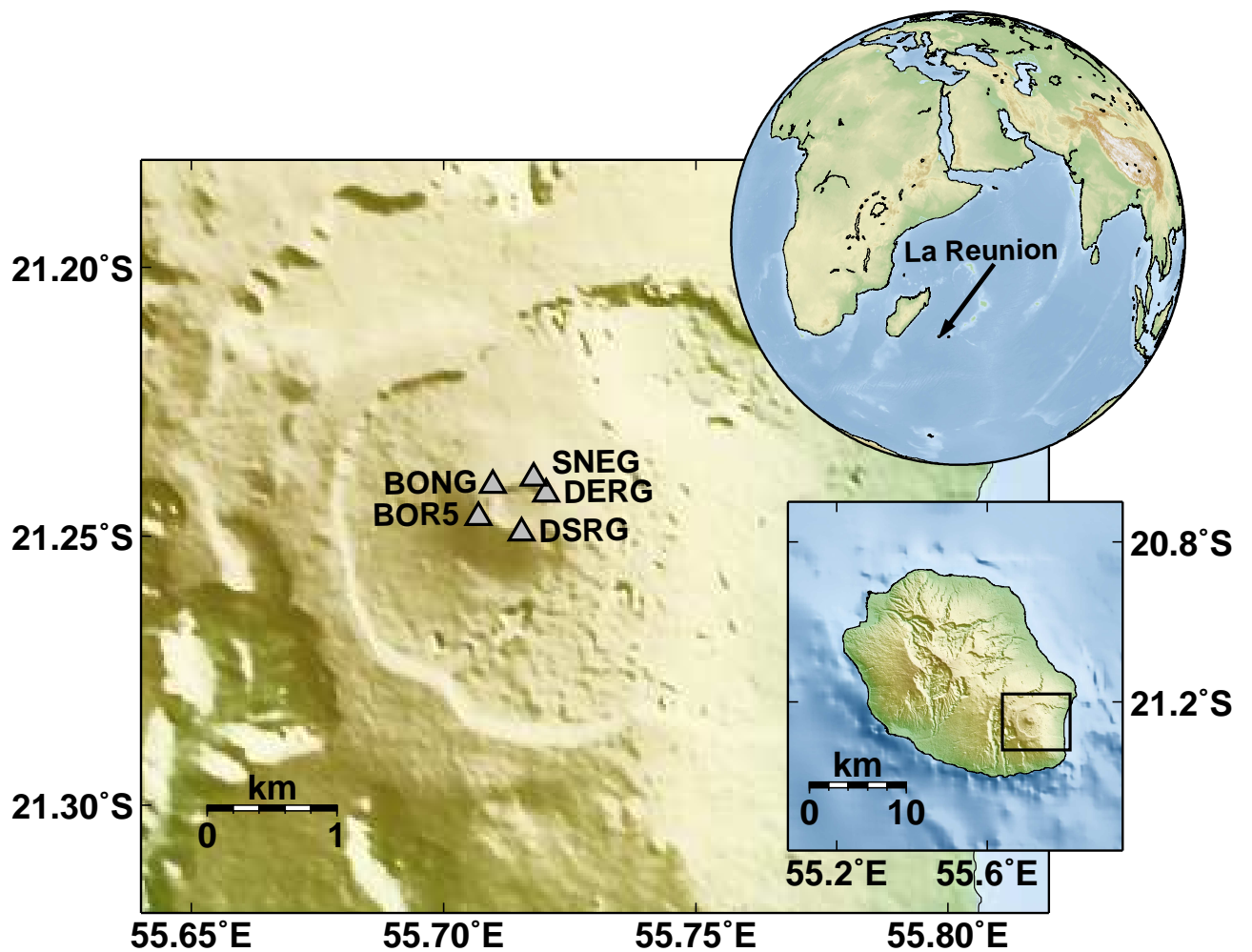


Figure 4.2: Location map of Piton de la Fournaise showing the GPS sites (grey triangles) from which the displacement time series used here have been extracted.

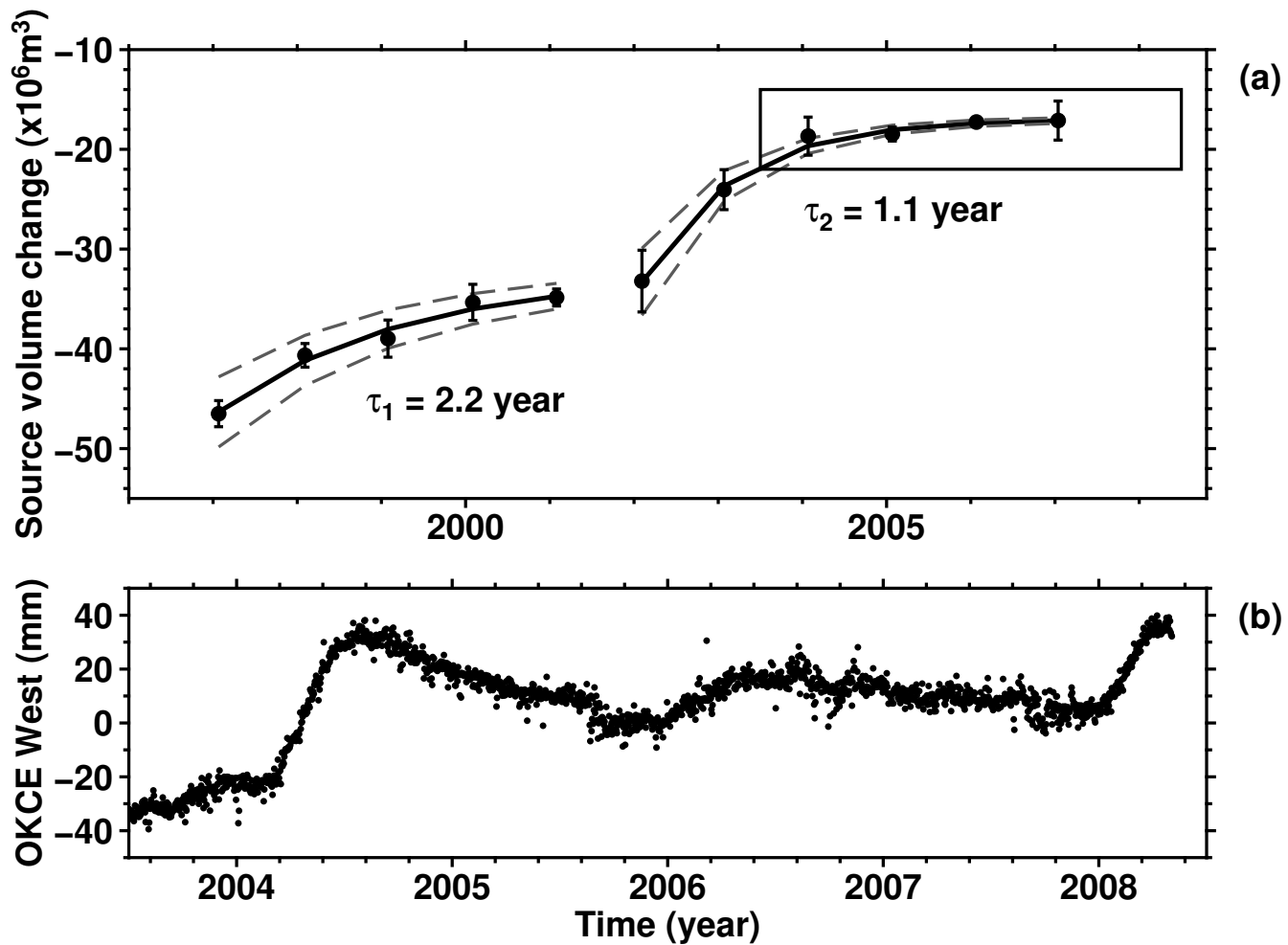


Figure 4.3: Geodetic time series products from Okmok volcano. The top sub-panel shows the cumulative volume change estimated from InSAR time series (Biggs et al., 2010). The bottom sub-panels shows a selected GPS time series reflecting the deformation regime before the 2008 eruption.

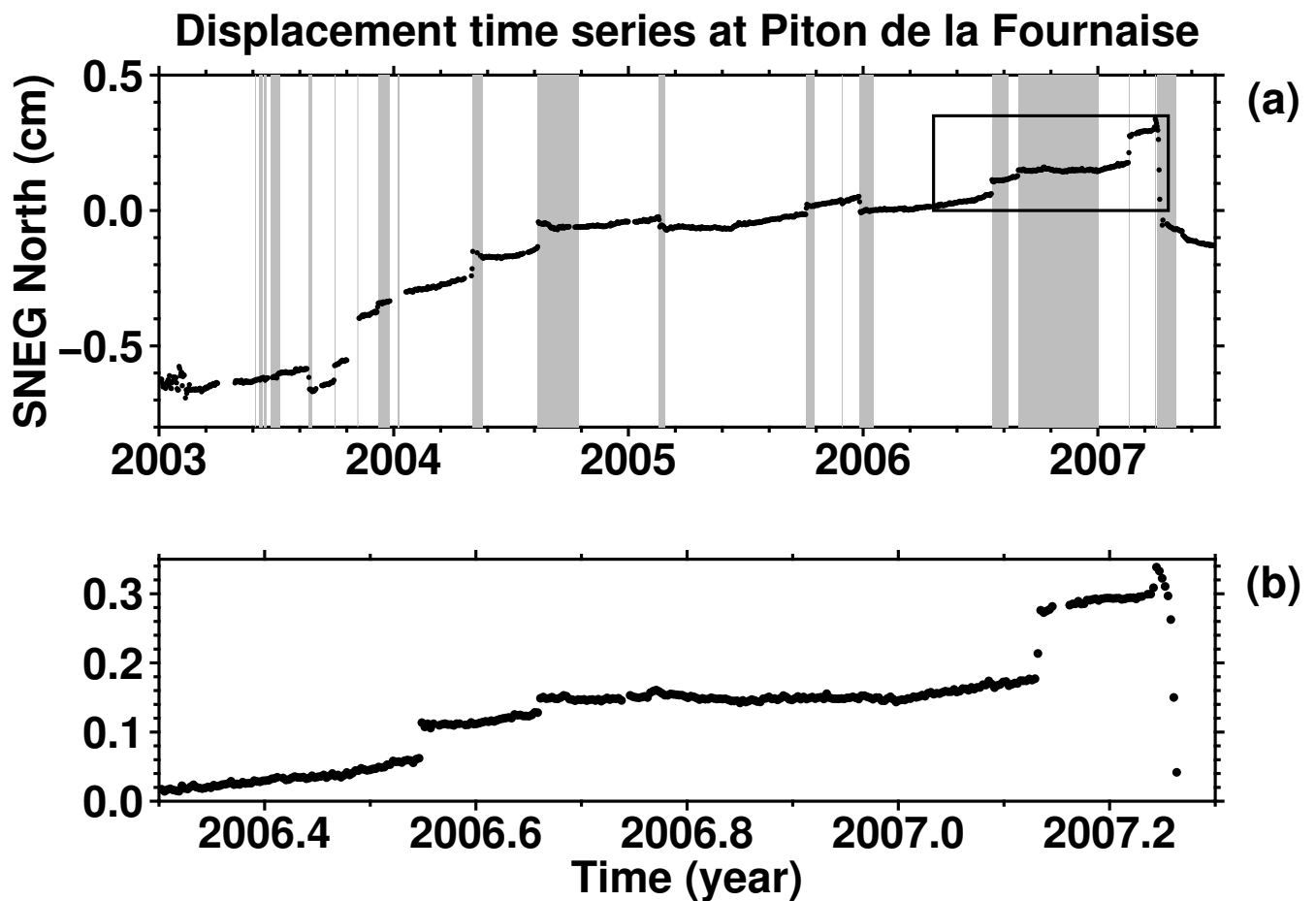


Figure 4.4: A selected GPS time series recorded at the summit of Piton de la Fournaise. The top sub-panel shows the time series between 2003 and 2007.5 (black dot) as well as the different intrusive and eruptive events (grey areas). The bottom sub-panel zooms in the pre-eruptive period of the large 2007 eruption.

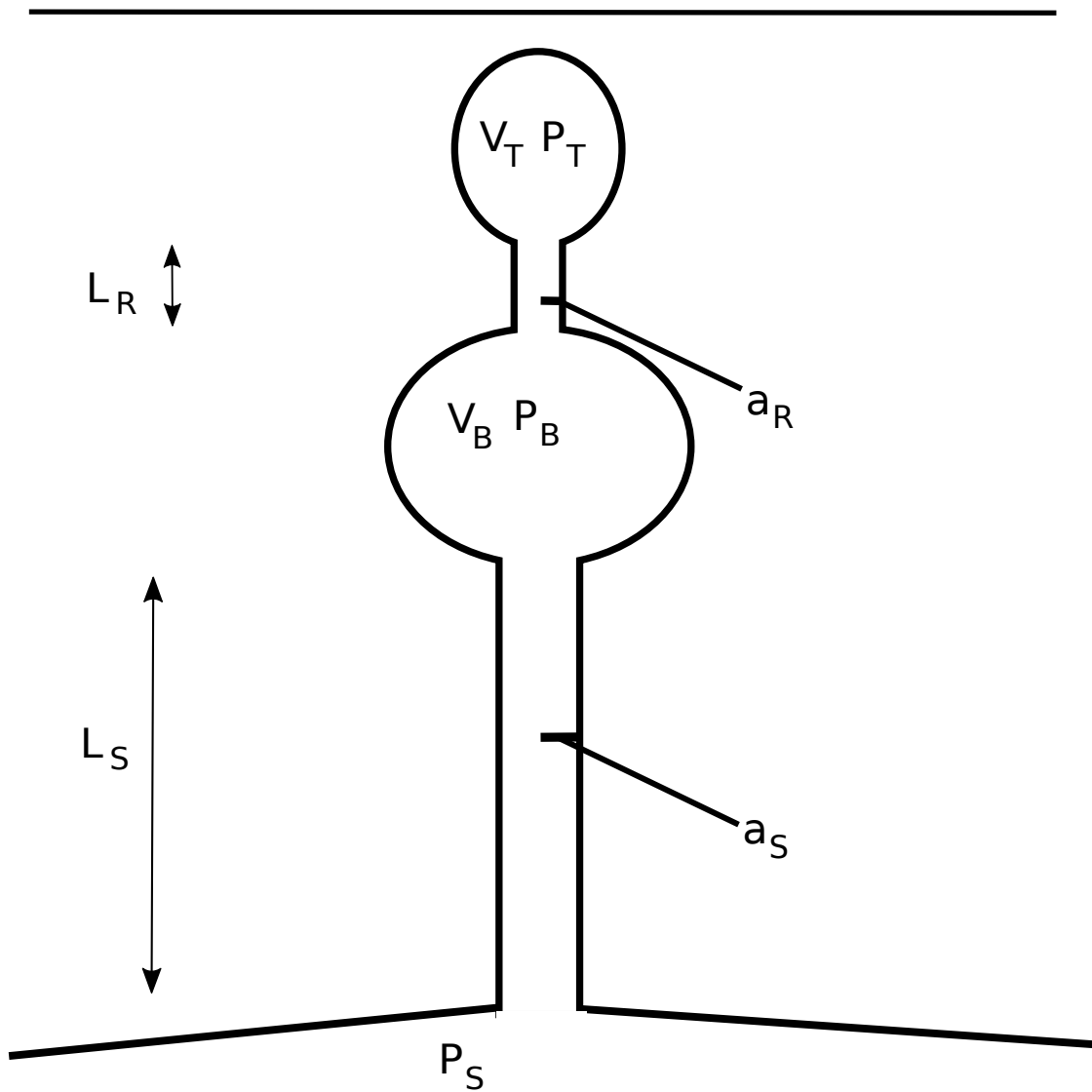


Figure 4.5: Schematic representation of the various elements composing the model described in the main text. Two shallow reservoirs, that have volume V_B and V_T and inside which the pressure are denoted P_B and P_T , are supplied by a deeper source region of constant pressure P_S .

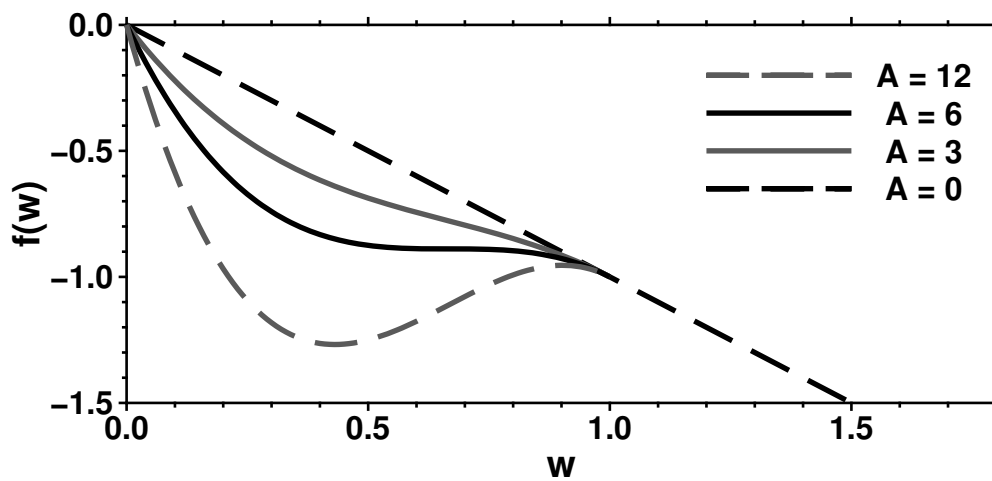


Figure 4.6: Changes in the shape of $f(w)$ as the dimensionless parameter A varies. When A is above 6 there is a range of w for which $f(w)$ increases. This is the critical characteristic of f that allows for the emergence of the relaxation oscillations.

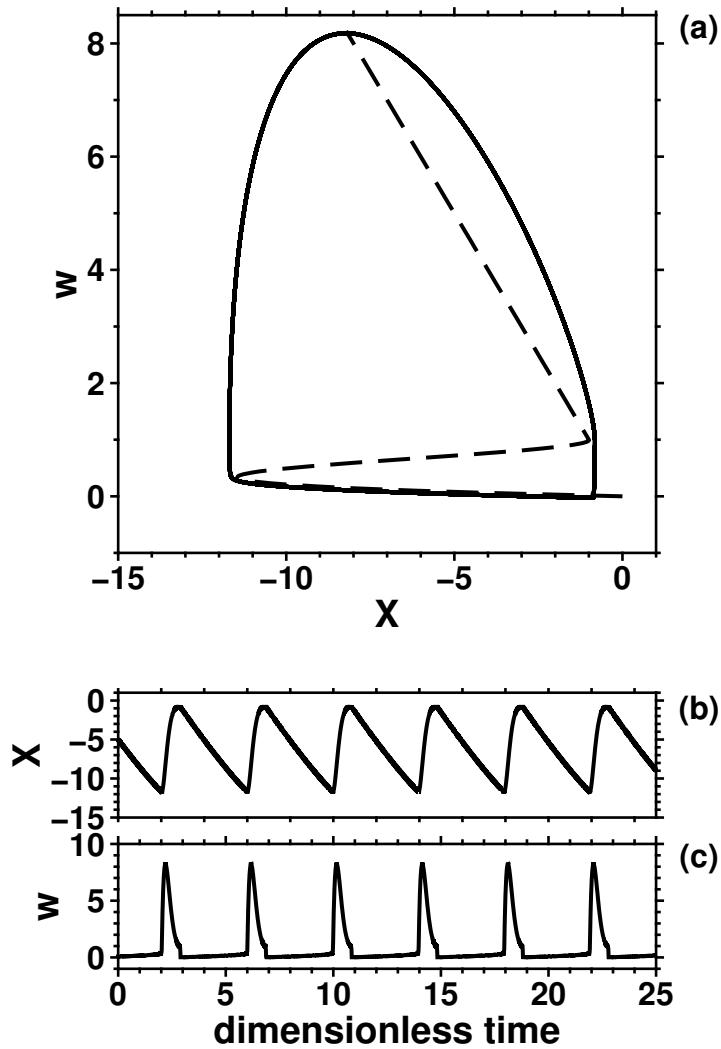


Figure 4.7: Nonlinear oscillations of the reduced model governed by Eq. (4.16): (a) phase portrait in the $(\Delta X, w)$ -plane ; (b) and (c) the associated time series representing, respectively, X and w . All plots are computed using $[\gamma, A, B, C, Q] = [10, 150, 1, 3, 4]$ in the equations. In panel (a), the closed trajectory (heavy solid line) is the limit cycle. The dashed curve represents the function $f(w)$ that is responsible for the shape of the limit cycle. As it can be understood from equation 4.24, the trajectory of the limit cycle either follows $f(w)$ or vertical lines.

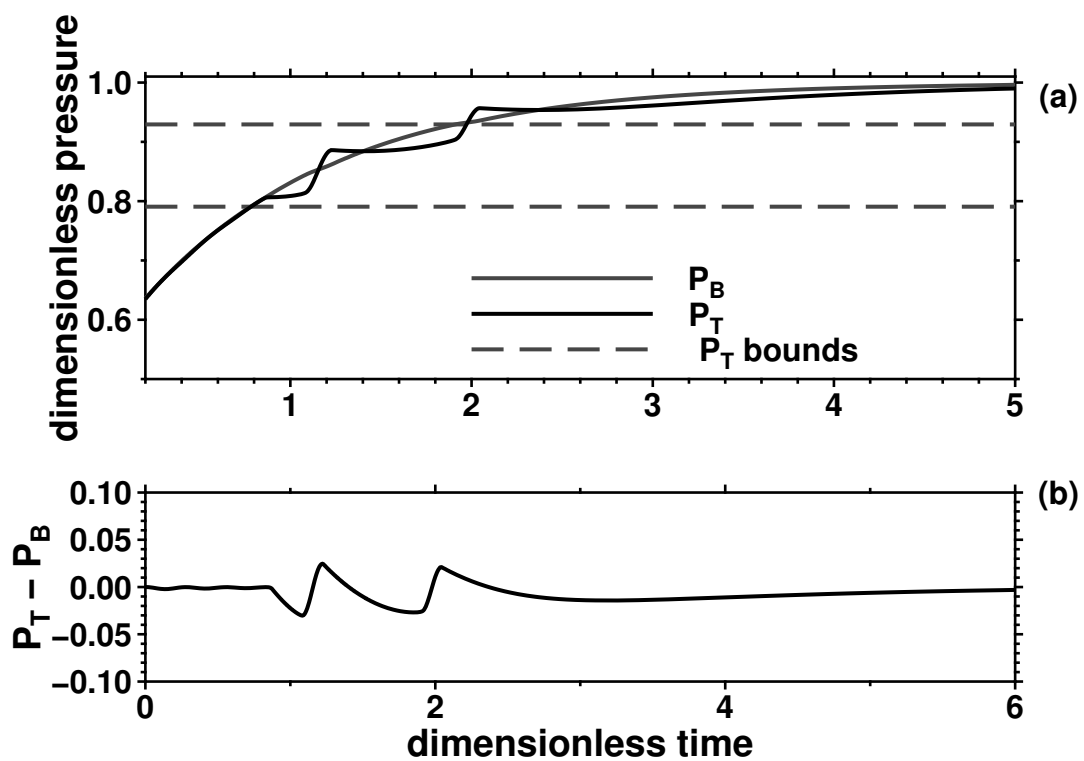


Figure 4.8: Time series reflecting the dynamics of the reservoir overpressure that is governed by equations 4.8 : (a) time series of both P_B and P_T ; (b) time series of $P_T - P_B$. Plots are computed using $[\gamma, A, B, C] = [2.5, 350, 10, 20]$.

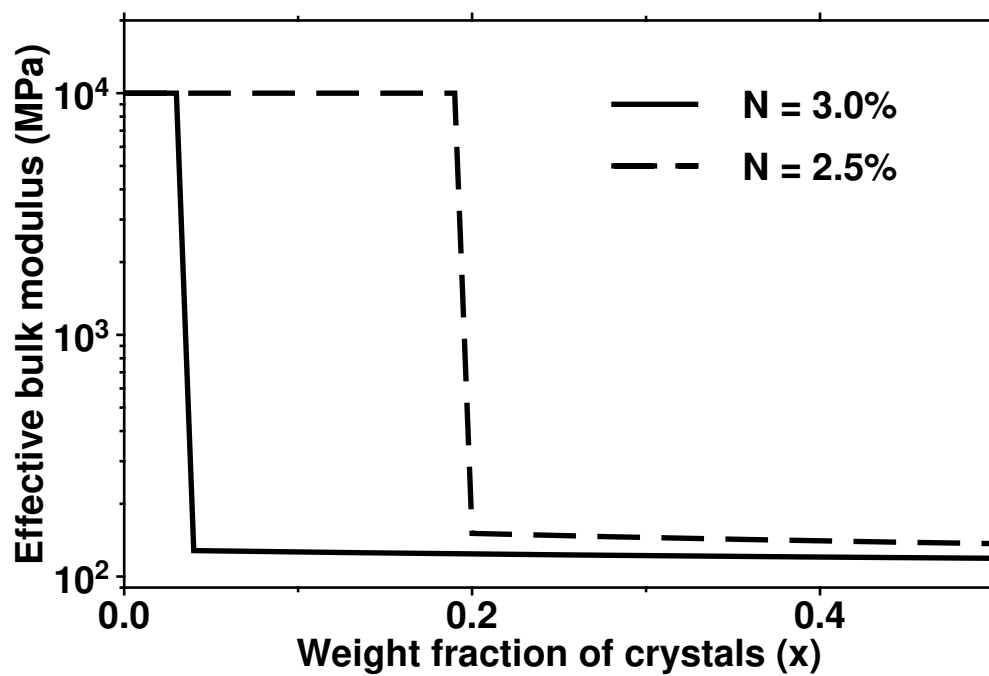


Figure 4.9: The effective modulus of the magmatic chambers as a function of both the weight fraction of crystals x and the total weight fraction of volatile. The computation is explained in section 4.10. The curves are computed using $\rho_m = 3000\text{kg}\cdot\text{m}^{-3}$, $\rho_c = 3200\text{kg}\cdot\text{m}^{-3}$, $T = 1100\text{C}$, $P = 60\text{MPa}$ and $E = 10^{10}\text{Pa}$.

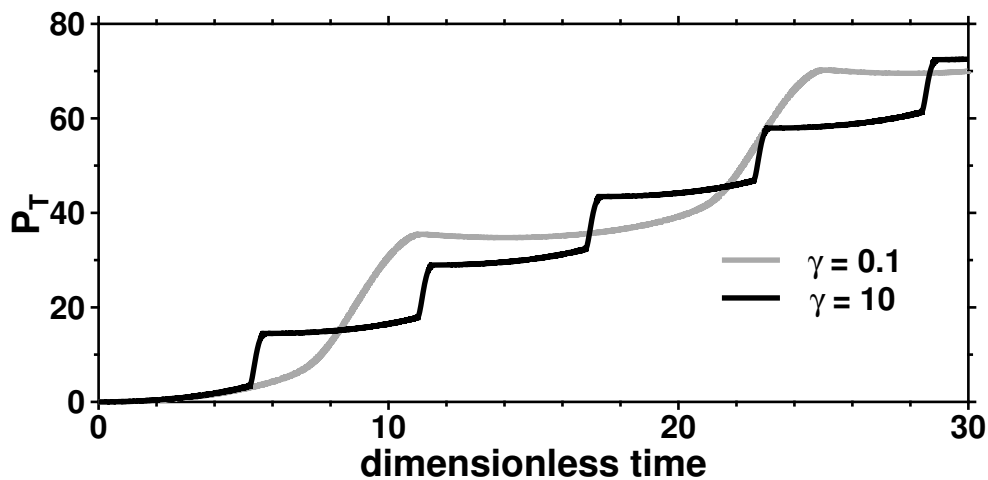


Figure 4.10: Effect of volatile exsolution on the overpressure oscillations in the top shallow reservoir. Two time series have been computed using two values of γ separated by two orders of magnitude which is approximately the effect that would have volatile exsolution on γ . Exsolution of volatile causes an increase of the value of γ that in turn causes a decrease of the amplitude and period of the oscillations. Both time series have been computed using $A = 150$, $Q = 4$, $B = 1$, $C = 3$.

CHAPTER 5

CONCLUSIONS AND PERSPECTIVES

Les séries temporelles géodésiques fournissent des informations sur la dynamique qualitative des systèmes géologiques. Cela signifie que si l'on souhaite modéliser la dynamique d'un système naturel par une équation du type

$$\frac{d\mathbf{y}}{dt} = \mathbf{F}(\mathbf{y}) \quad (5.1)$$

les séries temporelles peuvent permettre de contraindre l'opérateur \mathbf{F} .

Avec cette perspective comme ligne directrice nous avons analysé des séries temporelles GPS acquises sur quatre volcans actifs: Akutan, Okmok, Shishaldin de l'arc des Aléoutiennes et le Piton de la Fournaise à la Réunion. La M-SSA, une méthode d'analyse non paramétrique, permet de décomposer ces séries temporelles en modes de variabilité correspondant soit à des tendances non linéaires, à des modes oscillants ou à du bruit (Ghil et al., 2002). Ces quatre volcans possèdent une dynamique cyclique similaire représentée par seulement quelques uns des modes extraits par la M-SSA. Cette dynamique est en partie expliquée par un simple oscillateur non linéaire.

La relative simplicité de cet oscillateur —qui possède seulement deux variables— est cohérente avec la quantité d'information contenue dans les séries temporelles (Discussion du chapitre 3). Dans l'idée de concevoir un modèle physique pour comprendre l'émergence de

ce type de signature dans les séries temporelles de déformation volcanique, cette analogie permet de formuler des contraintes sur la dynamique qualitative de ces quatre volcans: par exemple un tel modèle physique doit posséder une dynamique oscillatoire non linéaire.

Le chapitre 4 montre qu'un modèle avec deux réservoirs connectés par un conduit dans lequel la viscosité du magma varie avec la température possède un tel régime oscillatoire non linéaire (Whitehead and Helfrich, 1991). Lorsque le magma ne subit aucune variation de viscosité à l'intérieur du conduit le modèle proposé est équivalent à ceux de connections hydrauliques couramment utilisés pour expliquer les séries temporelles géodésiques (e.g. Reverso et al., 2014). Il est donc facilement intégrable au cadre théorique déjà existant pour exploiter les séries temporelles géodésiques en vue de comprendre la dynamique volcanique.

Le régime oscillatoire peut se mettre en place uniquement lorsque (1) les variations de température du magma à l'intérieur du conduit sont suffisamment importantes et (2) lorsque le flux de magma qui entre dans le système est compris entre deux valeurs qui sont déterminées analytiquement à partir de l'analyse de stabilité linéaire du système. A Okmok on peut justement observer une transition vers ce régime oscillatoire lorsque le flux de magma entrant dans le système diminue et atteint une valeur seuil.

Les séries temporelles du Piton de la Fournaise présentent certaines irrégularités. Un tel comportement peut éventuellement être modélisé en ajoutant une variable au modèle réduit du chapitre 4. C'est le principe du chaos déterministe (e.g., Lorenz, 1963a; Guckenheimer and Holmes, 1983). Cette approche peut s'appuyer sur la littérature de la dynamique des fluides appliquée aux systèmes volcaniques afin d'identifier les processus physiques et/ou chimiques qui peuvent être couplés aux interactions hydrauliques et rendre la dynamique du système plus compliqué. Les études pétrologiques et géochimiques sur les laves des éruptions du Piton de la Fournaise qui ont eu lieu pendant la période étudiée permettent également d'identifier ces processus.

Nous avons brièvement étudié l'effet des volatiles sur l'amplitude et la période des oscillations de surpressions dans les chambres magmatiques. Un modèle prenant en compte les variations de la fraction de magma cristallisé et de volatiles dissous dans le magma mon-

tre qu'une exsolution des volatiles entraîne une baisse d'environ deux ordres de grandeur du module d'incompressibilité des chambres magmatiques. Ceci modifie la capacité de la chambre magmatique à se déformer élastiquement et provoque à la fois une augmentation de la période des oscillations et une augmentation de leurs amplitudes.

D'autres effets qu'il serait intéressant de considérer sont ceux liés à l'impact du régime thermique qui se met en place à l'intérieur du conduit qui sépare les deux zones de stockages du magma. Par exemple, le gradient de température à l'intérieur du conduit peut varier dans le temps ce qui aura également pour effet de modifier les amplitudes et périodes des oscillations de surpression. Le magma pourrait également cristalliser dans le conduit ce qui ferait varier à la fois la viscosité du magma et le rayon du conduit (e.g. Taylor, 1932; Bruce and Huppert, 1990). Les variations de ces deux paramètres ont des effets significatifs puisqu'ils sont respectivement élevés aux puissances 2 et -2 dans le paramètre sans dimension γ qui contrôle la manière dont les chambres magmatiques se déforment en réponse aux oscillations de surpressions (chapitre 4, equation 4.15).

Une suite naturelle à cette étude serait de coupler au modèle proposé des équations gouvernant l'évolution des paramètres mentionnés ci-dessus. Comme la dynamique résultante peut être compliquée une telle approche nécessiterait de définir des observables calculables à la fois à partir des séries temporelles géodésiques et des résultats d'un tel modèle. Ces observables permettraient de caractériser davantage la dynamique des systèmes volcaniques telle que vu par les séries temporelles géodésiques et de la comparer au modèle.

Le contenu fréquentiel pourrait constituer une telle observable puisque certaines solutions —même chaotiques— des systèmes d'équations différentielles présentent des fréquences dominantes (e.g. Ghil and Childress, 1987; Jordan and Smith, 2007). Cependant l'application brute de la transformée de Fourier sur les séries temporelles du Piton de la Fournaise ne révèlent aucune fréquence dominante.

Dans la littérature de la théorie des systèmes dynamiques certaines observables calculables directement à partir des séries temporelles sont régulièrement utilisés pour caractériser la dynamique sous-jacente (e.g., Bennetin et al., 1980; Abarbanel et al., 1992). Cependant,

les séries temporelles du Piton de la Fournaise présentent les épisodes d'inflations rapides comme des processus quasi-discrets du fait probablement du manque de résolution temporelle. Des outils statistiques adaptés devront sûrement être mis en œuvre pour définir de telles observables (Cowperrait, 2006).

Des portraits de phases construits directement à partir des séries temporelles de déformations, dont des exemples simples sont présentés dans le chapitre 3, peuvent également fournir des informations intéressantes. Les portraits de phases du chapitre 3 sont contenus dans les plans déplacements en fonction du taux de déplacement et ont été utilisés pour mettre en évidence le caractère oscillatoire de la dynamique reflétée par les séries temporelles de déformation. Cependant on peut également exploiter les différents modes extraits par la M-SSA pour reconstruire des portraits de phase à 3 dimensions qui permettraient de contraindre des modèles dynamiques possédant davantage de degrés de liberté (e.g. Broomhead and King, 1986a).

A Okmok nous pouvons exploiter le fait qu'en plus des modes associés aux oscillations du volcan et discutés au chapitre 3, un mode associé à l'éruption de 2008 est extrait par la M-SSA. A partir de ces modes un portrait de phase a été construit et est représenté en figure 5.1. Ce portrait de phase est une représentation géométrique de la dynamique associée à la transition des oscillations vers l'éruption de 2008. La trajectoire suit une spirale dans le plan horizontal puis est expulsée dans une direction perpendiculaire. Ce type de géométrie est comparable à une transition dynamique appelée bifurcation de Shilnikov et qui apparaît par exemple dans la dynamique des courants océaniques forcés par le vent (e.g. Ghil and Childress, 1987; Nadiga and Luce, 2001).

Enfin, l'idée qui consiste à exploiter les séries temporelles géodésiques pour obtenir des informations sur la dynamique qualitative des systèmes géologiques ne s'applique pas seulement aux volcans. Par exemple, les glissements lents des zones de subductions des Cascades et de Mexico forment également un régime oscillatoire non linéaire (Radiguet et al., 2012; Rogers and Dragert, 2003). Bien que ces phénomènes peuvent être expliqués, par exemple, par des interactions entre failles (Romanet et al., 2017), il pourrait être utile de formuler un modèle réduit —avec deux degrés de liberté— reposant à un niveau hié-

chique inférieur mais qui pourrait permettre d'identifier au premier ordre les conditions d'occurrences de tels comportements oscillatoires non linéaires.

An Okmok volcano phase portrait

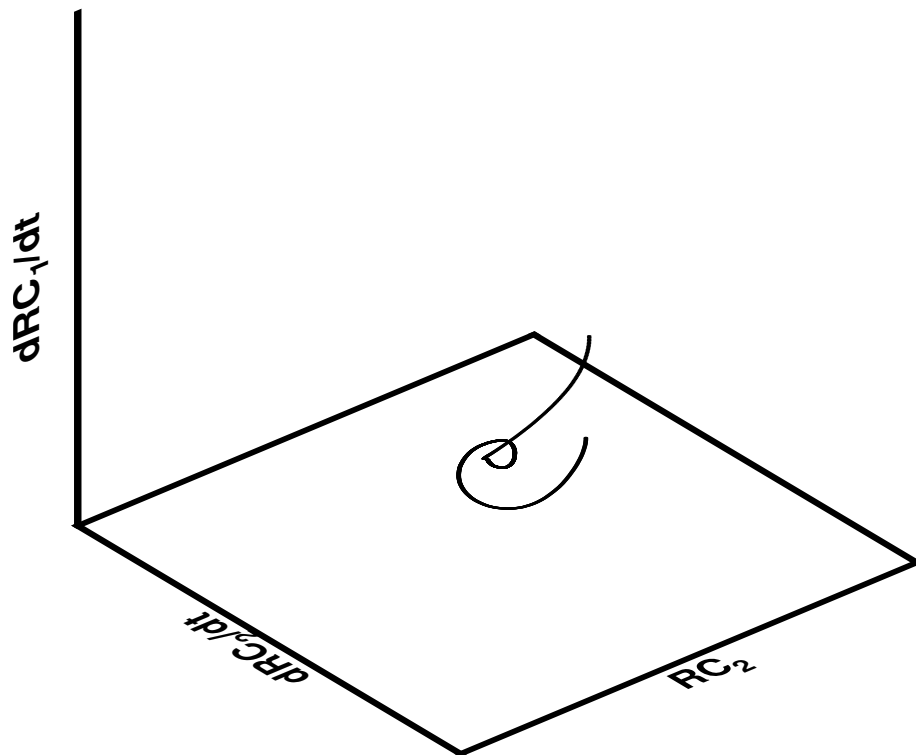


Figure 5.1: Phase portrait reconstructions in the displacement vs. rate-of-displacement vs. rate-of-displacement of the co-eruptive subsidence space. The geometric shape drawn by the trajectory is reminiscent of a Shilnikov bifurcation (To be compared with figure 6.12 in (e.g. Ghil and Childress, 1987)).

BIBLIOGRAPHY

- Abarbanel, H. D., Brown, R., and Kennel, M. B. (1992). Local lyapunov exponents computed from observed data. *Journal of Nonlinear Science*, 2(3):343–365.
- Abarbanel, H. D., Brown, R., Sidorowich, J. J., and Tsimring, L. S. (1993). The analysis of observed chaotic data in physical systems. *Reviews of Modern Physics*, 65(4):1331.
- Agnew, D. C. (1992). The time-domain behavior of power-law noises. *Geophysical Research Letters*, 19(4):333–336.
- Agnew, D. C. (2013). Realistic simulations of geodetic network data: The fakenet package. *Seismological Research Letters*, 84(3):426–432.
- Alessio, S. M. (2016). *Digital Signal Processing and Spectral Analysis for Scientists: Concepts and Applications*. Springer. Ch. 12. Singular Spectrum Analysis (SSA), pp. 537–571.
- Allen, M. R. and Robertson, A. W. (1996). Distinguishing modulated oscillations from coloured noise in multivariate datasets. *Climate Dynamics*, 12(11):775–784.
- Allen, M. R. and Smith, L. A. (1994). Investigating the origins and significance of low-frequency modes of climate variability. *Geophysical Research Letters*, 21(10):883–886.
- Barenblatt, G. I. (1996). *Scaling, self-similarity, and intermediate asymptotics: dimensional analysis and intermediate asymptotics*, volume 14. Cambridge University Press.

- Battaglia, J., Ferrazzini, V., Staudacher, T., Aki, K., and Cheminée, J.-L. (2005). Pre-eruptive migration of earthquakes at the piton de la fournaise volcano (réunion island). *Geophysical Journal International*, 161(2):549–558.
- Bennetin, G., Galgani, L., Giorgilli, A., and Strelcyn, J. (1980). Lyapunov characteristic exponents for smooth dynamical systems and for hamiltonian systems: A method for computing all of them. *Meccanica*, 15(9):27.
- Bevis, M., Alsdorf, D., Kendrick, E., Fortes, L. P., Forsberg, B., Smalley, R., and Becker, J. (2005). Seasonal fluctuations in the mass of the Amazon River system and Earth's elastic response. *Geophysical Research Letters*, 32(16):L16308.
- Biggs, J., Anthony, E. Y., and Ebinger, C. J. (2009). Multiple inflation and deflation events at Kenyan volcanoes, East African Rift. *Geology*, 37(11):979–982.
- Biggs, J., Lu, Z., Fournier, T., and Freymueller, J. T. (2010). Magma flux at Okmok Volcano, Alaska, from a joint inversion of continuous GPS, campaign GPS, and interferometric synthetic aperture radar. *Journal of Geophysical Research*, 115(B12).
- Blake, S. (1981). Volcanism and the dynamics of open magma chambers. *Nature*, 289(5800):783–785.
- Bletery, Q., Sladen, A., Delouis, B., Vallée, M., Nocquet, J.-M., Rolland, L., and Jiang, J. (2014). A detailed source model for the mw9.0 tohoku-oki earthquake reconciling geodesy, seismology, and tsunami records. *Journal of Geophysical Research: Solid Earth*, 119(10):7636–7653.
- Blewitt, G. (2001). A New Global Mode of Earth Deformation: Seasonal Cycle Detected. *Science*, 294(5550):2342–2345.
- Blewitt, G., Argus, D., Bennett, R., Bock, Y., Calais, E., Craymer, M., Davis, J., Dixon, T., Freymueller, J., Herring, T., et al. (2005). A stable north america reference frame (snarf): First release. In *Proceedings of the Joint UNAVCO/IRIS Workshop, Stevenson, WA, USA, June*, pages 9–11.

BIBLIOGRAPHY

- Boivin, P. and Bachèlery, P. (2009). Petrology of 1977 to 1998 eruptions of piton de la fournaise, la réunion island. *Journal of Volcanology and Geothermal Research*, 184(1):109–125.
- Boudoire, G., Liuzzo, M., Di Muro, A., Ferrazzini, V., Michon, L., Grassa, F., Derrien, A., Villeneuve, N., Bourdeu, A., Brunet, C., et al. (2017). Investigating the deepest part of a volcano plumbing system: Evidence for an active magma path below the western flank of piton de la fournaise (la réunion island). *Journal of Volcanology and Geothermal Research*, 341:193–207.
- Broomhead, D. S. and King, G. P. (1986a). Extracting qualitative dynamics from experimental data. *Physica D*, 20(23):217–236.
- Broomhead, D. S. and King, G. P. (1986b). On the qualitative analysis of experimental dynamical systems. In Sarkar, S., editor, *Nonlinear Phenomena and Chaos*, pages 113–144. Adam Hilger, Bristol.
- Bruce, P. M. and Huppert, H. E. (1989). Thermal control of basaltic fissure eruptions. *Nature*, 342(6250):665–667.
- Bruce, P. M. and Huppert, H. E. (1990). Solidification and melting along dykes by the laminar flow of basaltic magma. *Magma transport and storage*, pages 87–101.
- Caricchi, L., Biggs, J., Annen, C., and Ebmeier, S. (2014). The influence of cooling, crystallisation and re-melting on the interpretation of geodetic signals in volcanic systems. *Earth and Planetary Science Letters*, 388:166–174.
- Carr, J. (2012). *Applications of centre manifold theory*, volume 35. Springer Science & Business Media.
- Chanard, K., Avouac, J. P., Ramillien, G., and Genrich, J. (2014). Modeling deformation induced by seasonal variations of continental water in the Himalaya region: Sensitivity to Earth elastic structure. *Journal of Geophysical Research: Solid Earth*, 119(6):5097–5113.

- Chen, Q., van Dam, T., Sneeuw, N., X. Collilieux, X., M. Weigelt, M., and Reischung, P. (2013). Singular spectrum analysis for modeling seasonal signals from GPS time series. *Journal of Geodynamics*, 72:25–35.
- Comeau, M. J., Unsworth, M. J., Ticona, F., and Sunagua, M. (2015). Magnetotelluric images of magma distribution beneath Volcan Uturuncu, Bolivia: Implications for magma dynamics. *Geology*, 43(3):243–246.
- Cowperrwait, P. S. (2006). A spatial–temporal point process model of rainfall for the thames catchment, uk. *Journal of Hydrology*, 330(3):586–595.
- Delaney, P. and McTigue, D. (1994). Volume of magma accumulation or withdrawal estimated from surface uplift or subsidence, with application to the 1960 collapse of kilauea volcano. *Bulletin of Volcanology*, 56(6-7):417–424.
- Delaney, P. T. and Pollard, D. D. (1982). Solidification of basaltic magma during flow in a dike. *American Journal of Science*, 282(6):856–885.
- Deremble, B., d’Andrea, F., and Ghil, M. (2009). Fixed points, stable manifolds, weather regimes, and their predictability. *Chaos: An Interdisciplinary Journal of Nonlinear Science*, 19(4):043109.
- Dickey, J. O. (2002). Interdisciplinary space geodesy: Challenges in the new millennium. In Adam, J. and Schwarz, K. P., editors, *Vistas for Geodesy in the New Millennium*, pages 590–594. International Association of Geodesy.
- Dvorak, J. J. and Okamura, A. T. (1987). A hydraulic model to explain variations in summit tilt rate at kilauea and mauna loa volcanoes. *US Geol. Surv. Prof. Pap*, 1350(2):1281–1296.
- Famin, V., Welsch, B., Okumura, S., Bachelery, P., and Nakashima, S. (2009). Three differentiation stages of a single magma at piton de la fournaise volcano (reunion hot spot). *Geochemistry, Geophysics, Geosystems*, 10(1).
- Farmer, J. D., Ott, E., and Yorke, J. A. (1983). The dimension of chaotic attractors. *Physica D: Nonlinear Phenomena*, 7(1-3):153–180.

BIBLIOGRAPHY

- Feng, L. and Newman, A. V. (2009). Constraints on continued episodic inflation at Long Valley Caldera, based on seismic and geodetic observations. *Journal of Geophysical Research*, 114(B6).
- Fu, Y., Freymueller, J. T., and Jensen, T. (2012). Seasonal hydrological loading in southern Alaska observed by GPS and GRACE: Seasonal loading in Southern Alaska. *Geophysical Research Letters*, 39(15).
- Ghil, M., Allen, M. R., Dettinger, M. D., Ide, K., Kondrashov, D., Mann, M. E., Robertson, A. W., Saunders, A., Tian, Y., Varadi, F., and Yiou, P. (2002). Advanced spectral methods for climatic time series. *Reviews of Geophysics*, 40(1):3–1.
- Ghil, M. and Childress, S. (1987). *Topics in Geophysical Fluid Dynamics: Atmospheric Dynamics, Dynamo Theory, and Climate Dynamics*, volume 60 of *Applied Mathematical Sciences*. Springer Science & Business Media.
- Ghil, M. and Malanotte-Rizzoli, P. (1991). Data assimilation in meteorology and oceanography. *Advances in geophysics*, 33:141–266.
- Ghil, M. and Robertson, A. W. (2002). “waves” vs “particles” in the atmosphere’s phase space: A pathway to long-range forecasting? *Proc. Natl. Acad. Sci. USA*, 99, Suppl.:2493–2500.
- Ghil, M. and Vautard, R. (1991). Interdecadal oscillations and the warming trend in global temperature time series. *Nature*, 350:324–327.
- Grasman, J. (2011). Relaxation oscillations. In Meyers, R. A., editor, *Mathematics of Complexity and Dynamical Systems*, pages 1475–1488. Springer Science & Business Media.
- Groth, A. and Ghil, M. (2015a). Monte carlo singular spectrum analysis (ssa) revisited: Detecting oscillator clusters in multivariate datasets. *Journal of Climate*, 28(19):7873–7893.
- Groth, A. and Ghil, M. (2015b). Monte Carlo SSA revisited: Detecting oscillator clusters in multivariate data sets. *Journal of Climate*, in press.

- Guckenheimer, J. and Holmes, P. J. (1983). *Nonlinear Oscillations, Dynamical Systems, and Bifurcations of Vector Fields*, volume 42 of *Applied Mathematical Sciences*. Springer Science & Business Media.
- Heki, K. (2004). Dense GPS array as a new sensor of seasonal changes of surface loads. *The State of the Planet: Frontiers and Challenges in Geophysics*, pages 177–196.
- Huppert, H. E. and Woods, A. W. (2002). The role of volatiles in magma chamber dynamics. *Nature*, 420(6915):493.
- Hutchison, W., Biggs, J., Mather, T. A., Pyle, D. M., Lewi, E., Yirgu, G., Caliro, S., Chiodini, G., Clor, L. E., and Fischer, T. P. (2016). Causes of unrest at silicic calderas in the East African Rift: New constraints from InSAR and soil-gas chemistry at Aluto volcano, Ethiopia. *Geochemistry, Geophysics, Geosystems*, 17(8):3008–3030.
- Hutchison, W., Mather, T. A., Pyle, D. M., Biggs, J., and Yirgu, G. (2015). Structural controls on fluid pathways in an active rift system: A case study of the aluto volcanic complex. *Geosphere*, 11(3):542–562.
- Jaupart, C. and Mareschal, J.-C. (2010). *Heat generation and transport in the Earth*. Cambridge university press.
- Jaupart, C. and Tait, S. (1990). Dynamics of eruptive phenomena. *Reviews in Mineralogy and Geochemistry*, 24(1):213–238.
- Ji, K. H. and Herring, T. A. (2011). Transient signal detection using GPS measurements: Transient inflation at Akutan volcano, Alaska, during early 2008. *Geophysical Research Letters*, 38(6).
- Ji, K. H. and Herring, T. A. (2013). A method for detecting transient signals in GPS position time-series: smoothing and principal component analysis. *Geophysical Journal International*, 193(1):171–186.
- Jiang, N., Neelin, J. D., and Ghil, M. (1995). Quasi-quadrennial and quasi-biennial variability in the equatorial Pacific. *Climate Dynamics*, 12(2):101–112.

BIBLIOGRAPHY

- Jordan, D. W. and Smith, P. (2007). *Nonlinear Ordinary Differential Equations – An Introduction for Scientists and Engineers*. Oxford University Press, Oxford; New York.
- Keppenne, C. L. and Ghil, M. (1993). Adaptive filtering and prediction of noisy multivariate signals: An application to subannual variability in atmospheric angular momentum. *Intl. J. Bifurcation & Chaos*, 3:625–634.
- King, N. E., Argus, D., Langbein, J., Agnew, D. C., Bawden, G., Dollar, R. S., Liu, Z., Galloway, D., Reichard, E., Yong, A., Webb, F. H., Bock, Y., Stark, K., and Barseghian, D. (2007). Space geodetic observation of expansion of the San Gabriel Valley, California, aquifer system, during heavy rainfall in winter 2004/2005. *Journal of Geophysical Research: Solid Earth*, 112(B3):B03409.
- Klein, E., Fleitout, L., Vigny, C., and Garaud, J. (2016). Afterslip and viscoelastic relaxation model inferred from the large-scale post-seismic deformation following the 2010 Mw 8.8 Maule earthquake (Chile). *Geophysical Journal International*, 205(3):1455–1472.
- Larsen, J. F., Liwiski, M. G., Nye, C., Cameron, C., and Schaefer, J. R. (2013). The 2008 eruption of Okmok Volcano, Alaska: Petrological and geochemical constraints on the subsurface magma plumbing system. *Journal of Volcanology and Geothermal Research*, 264:85–106.
- Lenglin, O., Marsan, D., Got, J.-L., Pinel, V., Ferrazzini, V., and Okubo, P. G. (2008). Seismicity and deformation induced by magma accumulation at three basaltic volcanoes. *Journal of Geophysical Research*, 113(B12).
- Lorenz, E. N. (1963a). Deterministic Nonperiodic Flow. *Journal of the Atmospheric Sciences*, 20(2):130–141.
- Lorenz, E. N. (1963b). Deterministic nonperiodic flow. *Journal of the atmospheric sciences*, 20(2):130–141.
- Lu, Z., Dzurisin, D., Biggs, J., Wicks, C., and McNutt, S. (2010). Ground surface deformation patterns, magma supply, and magma storage at Okmok volcano, Alaska, from InSAR analysis: 1. Inter-eruption deformation, 1997–2008. *Journal of Geophysical Research: Solid Earth*, 115(B5).

- Lu, Z., Masterlark, T., and Dzurisin, D. (2005). Interferometric synthetic aperture radar study of Okmok volcano, Alaska, 1992–2003: Magma supply dynamics and postemplacement lava flow deformation. *Journal of Geophysical Research: Solid Earth*, 110(B2).
- Mañé, R. (1981). On the dimension of the compact invariant sets of certain non-linear maps. In *Dynamical Systems and Turbulence*, volume 898 of *Lecture Notes in Mathematics*, pages 230–242. Springer, Berlin.
- Mao, A., Harrison, C. G. A., and Dixon, T. H. (1999). Noise in GPS coordinate time series. *Journal of Geophysical Research: Solid Earth*, 104(B2):2797–2816.
- Massonnet, D., Rossi, M., Carmona, C., Adragna, F., Peltzer, G., Feigl, K., and Rabaute, T. (1993). The displacement field of the Landers earthquake mapped by radar interferometry. *Nature*, 364(6433):138–142.
- Masterlark, T., Haney, M., Dickinson, H., Fournier, T., and Searcy, C. (2010). Rheologic and structural controls on the deformation of Okmok volcano, Alaska: FEMs, InSAR, and ambient noise tomography. *Journal of Geophysical Research: Solid Earth*, 115(B2).
- McLeod, P. and Tait, S. (1999). The growth of dykes from magma chambers. *Journal of Volcanology and Geothermal Research*, 92(3):231–245.
- Mériaux, C. and Jaupart, C. (1995). Simple fluid dynamic models of volcanic rift zones. *Earth and Planetary Science Letters*, 136(3):223–240.
- Miller, M. M., Melbourne, T., Johnson, D. J., and Sumner, W. Q. (2002). Periodic slow earthquakes from the Cascadia subduction zone. *Science*, 295(5564):2423–2423.
- Mogi, K. (1958). Relations between the eruptions of various volcanoes and the deformations of the ground surfaces around them. *Bull. Earthquake Res. Inst.*, 36:99–134.
- Montillet, J.-P., Williams, S. D. P., Koulali, A., and McClusky, S. C. (2015). Estimation of offsets in GPS time-series and application to the detection of earthquake deformation in the far-field. *Geophysical Journal International*, 200(2):1205–1219.

BIBLIOGRAPHY

- Munekane, H. and Matsuzaba, S. (2004). Nontidal ocean mass loading detected by gps observations in the tropical pacific region. *Geophysical Research Letters*, 31(8):L08602–4.
- Nadiga, B. T. and Luce, B. P. (2001). Global bifurcation of shilnikov type in a double-gyre ocean model. *Journal of physical oceanography*, 31(9):2669–2690.
- Newman, A. V., Dixon, T. H., and Gourmelen, N. (2006). A four-dimensional viscoelastic deformation model for Long Valley Caldera, California, between 1995 and 2000. *Journal of Volcanology and Geothermal Research*, 150(1-3):244–269.
- Ohtani, R., McGuire, J. J., and Segall, P. (2010). Network strain filter: A new tool for monitoring and detecting transient deformation signals in GPS arrays. *Journal of Geophysical Research*, 115(B12).
- Packard, N. H., Crutchfield, J. P., Farmer, J. D., and Shaw, R. S. (1980). Geometry from a Time Series. *Physical Review Letters*, 45(9):712–716.
- Parks, M. M., Biggs, J., England, P., Mather, T. A., Nomikou, P., Palamartchouk, K., Papanikolaou, X., Paradissis, D., Parsons, B., Pyle, D. M., Raptakis, C., and Zacharis, V. (2012). Evolution of Santorini Volcano dominated by episodic and rapid fluxes of melt from depth. *Nature Geoscience*, 5(10):749–754.
- Peltier, A., Bachèlery, P., and Staudacher, T. (2009). Magma transport and storage at piton de la fournaise (la réunion) between 1972 and 2007: A review of geophysical and geochemical data. *Journal of Volcanology and Geothermal Research*, 184(1):93–108.
- Peltier, A., Famin, V., Bachèlery, P., Cayol, V., Fukushima, Y., and Staudacher, T. (2008). Cyclic magma storages and transfers at piton de la fournaise volcano (la réunion hotspot) inferred from deformation and geochemical data. *Earth and Planetary Science Letters*, 270(3):180–188.
- Pinel, V., Jaupart, C., and Albino, F. (2010). On the relationship between cycles of eruptive activity and growth of a volcanic edifice. *Journal of Volcanology and Geothermal Research*, 194(4):150–164.

- Plaut, G. and Vautard, R. (1994). Spells of Low-Frequency Oscillations and Weather Regimes in the Northern Hemisphere. *Journal of the Atmospheric Sciences*, 51(2):210–236.
- Preisendorfer, R. W., Zwiers, F., and Barnett, T. (1981). Foundations of principal component selection rules. *SIO Reference Series 81-4 May 1981*. 192 p, 37 Fig, 33 Tab, 75 Ref.
- Radiguet, M., Cotton, F., Vergnolle, M., Campillo, M., Walpersdorf, A., Cotte, N., and Kostoglodov, V. (2012). Slow slip events and strain accumulation in the guerrero gap, mexico. *Journal of Geophysical Research: Solid Earth*, 117(B4).
- Reverso, T., Vandemeulebrouck, J., Jouanne, F., Pinel, V., Villemin, T., Sturkell, E., and Bascou, P. (2014). A two-magma chamber model as a source of deformation at grímsvötn volcano, iceland. *Journal of Geophysical Research: Solid Earth*, 119(6):4666–4683.
- Riel, B., Simons, M., Agram, P., and Zhan, Z. (2014a). Detecting transient signals in geodetic time series using sparse estimation techniques. *Journal of Geophysical Research: Solid Earth*, 119(6):5140–5160.
- Riel, B., Simons, M., Agram, P., and Zhan, Z. (2014b). Detecting transient signals in geodetic time series using sparse estimation techniques. *Journal of Geophysical Research: Solid Earth*, 119(6):5140–5160.
- Rivet, D., Brenguier, F., Clarke, D., Shapiro, N. M., and Peltier, A. (2014). Long-term dynamics of Piton de la Fournaise volcano from 13 years of seismic velocity change measurements and GPS observations. *Journal of Geophysical Research: Solid Earth*, 119(10):7654–7666.
- Rogers, G. and Dragert, H. (2003). Episodic tremor and slip on the cascadia subduction zone: The chatter of silent slip. *Science*, 300(5627):1942–1943.
- Romanet, P., Bhat, H. S., Jolivet, R., and Madariaga, R. (2017). Fast and slow earthquakes emerge due to fault geometrical complexity. *arXiv preprint arXiv:1709.10336*.
- Roux, J., Rossi, A., Bachelart, S., and Vidal, C. (1980). Representation of a strange attractor from an experimental study of chemical turbulence. *Physics Letters A*, 77(6):391–393.

BIBLIOGRAPHY

- Segall, P. (2010). *Earthquake and volcano deformation*. Princeton University Press.
- Sparks, R. (2003). Forecasting volcanic eruptions. *Earth and Planetary Science Letters*, 210(1):1–15.
- Szeliga, W., Melbourne, T., Santillan, M., and Miller, M. (2008). Gps constraints on 34 slow slip events within the cascadia subduction zone, 1997–2005. *Journal of Geophysical Research: Solid Earth*, 113(B4).
- Taisne, B. and Tait, S. (2011). Effect of solidification on a propagating dike. *Journal of Geophysical Research: Solid Earth*, 116(B1).
- Tait, S., Jaupart, C., and Vergnolle, S. (1989). Pressure, gas content and eruption periodicity of a shallow, crystallising magma chamber. *Earth and Planetary Science Letters*, 92(1):107–123.
- Takens, F. (1981a). Detecting strange attractors in turbulence. In *Dynamical Systems and Turbulence*, volume 898 of *Lecture Notes in Mathematics*, pages 366–381. Springer, Berlin.
- Takens, F. (1981b). Detecting strange attractors in turbulence. In *Dynamical Systems and Turbulence, Warwick 1980*, pages 366–381. Springer.
- Tarantola, A. (2005). *Inverse problem theory and methods for model parameter estimation*. SIAM.
- Taylor, G. I. (1932). The viscosity of a fluid containing small drops of another fluid. *Proceedings of the Royal Society of London. Series A, Containing Papers of a Mathematical and Physical Character*, 138(834):41–48.
- Theiler, J., Galdrikian, B., Longtin, A., Eubank, S., and Farmer, J. D. (1991). Testing for nonlinearity in time series: The method of surrogate data. Technical report, Los Alamos National Laboratory, Los Alamos, NM (United States).
- Tran, D. T. (2013). *Analyse rapide et robuste des solutions GPS pour la tectonique*. PhD thesis, University of Nice Sophia Antipolis.
- Unal, Y. S. and Ghil, M. (1995). Interannual and interdecadal oscillation patterns in sea level. *Climate Dynamics*, 11(5):255–278.

- van Dam, T. M. and Herring, T. A. (1994). Detection of atmospheric pressure loading using very long baseline interferometry measurements. *Journal of Geophysical Research: Solid Earth*, 99(B3):4505–4517.
- van Dam, T. M. and Wahr, J. (1998). Modeling environment loading effects: a review. *Physics and Chemistry of the Earth*, 23(910):1077–1087.
- Van der Pol, B. (1926). On relaxation-oscillations. *The London, Edinburgh, and Dublin Philosophical Magazine and Journal of Science*, 2(11):978–992.
- Van der Pol, B. (1940). Biological rhythms considered as relaxation oscillations. *Acta Med. Scand. Suppl.*, 108:76–87.
- Vautard, R. and Ghil, M. (1989). Singular spectrum analysis in nonlinear dynamics, with applications to paleoclimatic time series. *Physica D: Nonlinear Phenomena*, 35(3):395–424.
- Vautard, R., Yiou, P., and Ghil, M. (1992). Singular-spectrum analysis: A toolkit for short, noisy chaotic signals. *Physica D*, 58:95–126.
- Wallace, J. M. and Gutzler, D. S. (1981). Teleconnections in the Geopotential Height Field during the Northern Hemisphere Winter. *Monthly Weather Review*, 109(4):784–812.
- Walwer, D., Calais, E., and Ghil, M. (2016). Data-adaptive detection of transient deformation in geodetic networks. *Journal of Geophysical Research: Solid Earth*, 121(3):2129–2152.
- Whitehead, J. and Helfrich, K. R. (1991). Instability of flow with temperature-dependent viscosity: a model of magma dynamics. *Journal of Geophysical Research: Solid Earth*, 96(B3):4145–4155.
- Williams, S. D. P. (2003). The effect of coloured noise on the uncertainties of rates estimated from geodetic time series. *Journal of Geodesy*, 76(9-10):483–494.
- Williams, S. D. P. (2004). Error analysis of continuous GPS position time series. *Journal of Geophysical Research*, 109(B3).
- Zhang, J., Bock, Y., Johnson, H., Fang, P., Williams, S., Genrich, J., Wdowinski, S., and Behr, J. (1997). Southern California permanent GPS geodetic array: Error analysis of

BIBLIOGRAPHY

daily position estimates and site velocities. *Journal of Geophysical Research: Solid Earth*, 102(B8):18035–18055.

Résumé

Nous étudions dans un premier temps l'intérêt de l'utilisation de la "multichannel singular spectrum analysis" (M-SSA) sur des séries temporelles de positionnements GPS. Cette méthode permet de simultanément analyser un ensemble de séries temporelles et d'en extraire des modes de variabilités communs sans utiliser d'information a priori sur les structures spatiales et temporelles des champs géophysiques. Ces modes correspondent à des tendances non linéaires, des oscillations ou du bruit. Nous l'appliquons à des données enregistrées sur le volcan Akutan en Alaska. Nous y extrayons deux types de signaux. L'un correspondant à des déformations dites saisonnières, l'autre représentant deux cycles d'inflations et de déflations successifs du volcan Akutan. Les inflations sont rapides et courtes et suivies de déflations plus lentes et plus longues.

Dans une seconde partie nous tirons parti de la M-SSA pour analyser des séries temporelles enregistrées sur plusieurs volcans. Les volcans Okmok et Shishaldin en Alaska et le Piton de la Fournaise à la Réunion possèdent une partie de leurs histoires de déformations qui est similaire à celle d'Akutan. Le caractère oscillatoire de ces cycles de déformations est comparé au régime oscillatoire d'un simple oscillateur non linéaire. Les données pétrologiques, géochimiques et géophysiques disponibles pour Okmok et le Piton de la Fournaise combinées aux contraintes sur la dynamique apportées par l'oscillateur non linéaire permet de proposer un modèle physique. Deux réservoirs superficiels sont connectés par un conduit cylindrique dans lequel le magma possède une viscosité qui dépend de la température. Un tel système se comporte de manière similaire à l'oscillateur non linéaire étudié précédemment. Lorsque que le gradient de température vertical présent dans le fluide est suffisamment important et que le flux de magma entrant dans le système de réservoirs est compris entre deux valeurs déterminées analytiquement un régime oscillatoire se met en place.

Mots Clés

Séries temporelles, géodésie, volcans, Dynamiques non linéaire

Abstract

We study the use of the "multichannel singular spectrum analysis" on GPS time series. This method allows to simultaneously analyze a set of time series in order to extract from it common modes of variability without using any a priori on the temporal or the spatial structure of geophysical fields. The extracted modes correspond either to nonlinear trends, oscillations or noise. The method is applied on a set of GPS time series recorded at Akutan, a volcano located in Aleutian arc in Alaska. Two types of signals are extracted from it. The first one corresponds to seasonal deformations and the other represents two successive cycles of inflation and subsidence of Akutan volcano. The inflations are fast and short and are followed by deflations that are slower and longer.

In the second part we take benefit of the M-SSA to analyze GPS time series recorded at several volcanoes. Okmok and Shishaldin in Alaska and Piton de la Fournaise in La Réunion possess a part of their deformation history that is similar to Akutan volcano. The cyclic nature of the observed deformations leads us to make an analogy between the oscillatory regime of a simple nonlinear oscillator and the deformation cycles of these volcanoes.

Geochemical, petrological and geophysical data available for Okmok and Piton de la Fournaise combined with the constraint on the qualitative dynamics bring by the nonlinear oscillator allow to propose a physical model. Two shallow reservoirs are connected by a cylindrical conduit in which the magma have a viscosity that depends on the temperature. Such system behaves like the nonlinear oscillator mentioned above. When the temperature gradient inside the conduit is large enough and the flux of magma entering the shallow system is bounded by values that are determined analytically a nonlinear oscillatory regime arises.

Keywords

Time series, geodesy, volcanoes, Nonlinear dynamics